THE USES OF DISTRIBUTED TEMPERATURE SURVEY (DTS) DATA

A DISSERTATION
SUBMITTED TO THE DEPARTMENT OF
ENERGY RESOURCES ENGINEERING
AND THE COMMITTEE ON GRADUATE STUDIES
OF STANFORD UNIVERSITY
IN PARTIAL FULFILLMENT OF THE REQUIREMENTS
FOR THE DEGREE OF
DOCTOR OF PHILOSOPHY

Zhe Wang

August 2012

This dissertation is online at: http://purl.stanford.edu/ds180yx9388

I certify that I have read this dissertation and that, in my opinion, it is fully adequate in scope and quality as a dissertation for the degree of Doctor of Philosophy.

Roland Horne, Primary Adviser

I certify that I have read this dissertation and that, in my opinion, it is fully adequate in scope and quality as a dissertation for the degree of Doctor of Philosophy.

Peter Kitanidis

I certify that I have read this dissertation and that, in my opinion, it is fully adequate in scope and quality as a dissertation for the degree of Doctor of Philosophy.

Tapan Mukerji

Approved for the Stanford University Committee on Graduate Studies.

Patricia J. Gumport, Vice Provost Graduate Education

This signature page was generated electronically upon submission of this dissertation in electronic format. An original signed hard copy of the signature page is on file in University Archives.

I certify that I have read this dissertation and that, in my opinion, it is fully adequate in scope and quality as a dissertation for the degree of Doctor of Philosophy.

(Roland N. Horne) Principal Adviser

I certify that I have read this dissertation and that, in my opinion, it is fully adequate in scope and quality as a dissertation for the degree of Doctor of Philosophy.

(Tapan Mukerji)

I certify that I have read this dissertation and that, in my opinion, it is fully adequate in scope and quality as a dissertation for the degree of Doctor of Philosophy.

(Peter Kitanidis - Civil Engineering Department)

Approved for the University Committee on Graduate Studies

Acknowledgements

"Life is like riding a bicycle. To keep your balance, you must keep moving."

-Albert Einstein

At the moment approaching the last step of my PhD, I am more and more grateful to the helpers along my way. I appreciate their kindly help and warm encouragement, respect their immense creativity, and admire their humbleness.

Among them, the first person I want to thank is my advisor, Professor Roland Horne. He deserves the respect for a successful professor. One of the most important things I learned from him is the merit of research: combining rigid scientific knowledge with enormously comprehensive industrial background, while keeping maximum freedom of the exploration for unknown areas. Undoubtedly, Roland inspires me by his successful career. In addition, we established a very close personal relationship. The annual Thanksgiving dinner and summer BBQ, held by his wife Yoko Kawashima and him, are magical venues for me to feel at home. This feeling is especially valuable for a foreign student like me. Many thanks to Roland, I am very fortunate and honored to be his graduate student.

I also would like to express my gratitude to another mentor of mine, Professor Shiyi Zheng from Heriot-Watt University. I appreciate his recommendation when I was applying for Stanford, and thank him for his caring and attention to me all the way along. He was always enlightening when road was misty for me, and inspiring when frustration hit me. His success of career encourages me to aim higher, and work

harder.

Stanford University provides a systematic, diversified and creative academic environment for its students. All the faculty members of Energy Resources Engineering Department and all the lecturers of the course I have taken at Stanford strengthen my academic ability, helping me feel confident about the credentials of a Stanford PhD degree. Meanwhile, I would like to thank all the engineers I have worked with. Their field knowledge influenced me deeply, bringing more sense to shape my research.

An indispensable part of a happy college life is to have wonderful colleagues. The weekly Supri-D meeting is really a enjoyable time, when every member is sharing their ideas, discussing courses and casting light to other's research. Furthermore, I am really in luck to be a part of the ERE student community, where everybody is immersed in joyful air for communicating and sharing.

Last but not least, my thanks is sent to my family members. My parents, Yubao Wang and Yumei He, are never reserved when offering me support. Their lofty personalities and life experience show me the way that leads a boy to a man, a man with responsibility, kindness and humbleness. Also, I am sincerely grateful to my wife Hansong, who is committed herself to biomedical research. I respect her diligence and hunger for scientific research. Meanwhile, she is indeed a very good life partner, who is willing to share me happiness and joy, always be together with me no matter life is filled with ups or downs. It is hard to imagine how miserable my life would be without the colors she puts in.

"Life is like riding a bicycle. To keep your balance, you must keep moving." The five years at Stanford have been educational and memorable, but life should be moving to next stage. I believe this experience helps me be prepared for future challenges in my life. I thank all the persons who have helped me, taught me, argued with me and guided me.

Abstract

Temperature change plays an important role in many downhole processes, and temperature measurements have long been used to monitor the performance of producing wells, evaluate water-injection profiles and diagnose the effectiveness of fracture jobs, etc. However, for many years, the utilization of downhole temperature measurement was largely over-shadowed by other measurements obtained through sophisticated suites of logging tools. However, the development of fiber-optic technology has helped a resurgence of interest in temperature measurement. One characteristic of fiber-optic temperature measurement is that it is capable of measuring multiple points simultaneously. The fiber-optic tool used to measure temperature is called a Distributed Temperate Survey (DTS), which measures temperature along the whole interval covered by the fiber.

In our study, we explored approaches of how to interpret DTS data. The significant contributions of this work include:

1. Building a wellbore/reservoir coupled thermal model

   The need to interpret wellbore temperature profiles measured by Distributed Temperature Sensors (DTS) requires a correspondingly sophisticated type of well model. To be specific, this model should be capable of predicting pressure and temperature distributions under a nonisothermal, multicomponent and multiphase production scenario. In our model, wellbore pressure and temperature

were solved separately and then coupled by iteration. Accuracy was assured by the following three ways:

(a) Using the drift flux model to predict multiphase flow pressure;

(b) Fluid PVT properties were obtained by solving Equations of State, which is more accurate than the values obtained by averaging or mixing rules;

(c) Using numerical methods to solve the heat transfer between wellbore and formation, avoiding the assumption of an invariant relaxation length.

This model was verified by comparing with several previously published models.

2. Estimating flowrate profile from temperature profile measurement

Measuring flowrate profile can be a challenging job for traditional single-point flowrate measurement tools, and it becomes very unreliable especially for multiphase flow and complex well geometries. However, temperature profile provides an alternative approach for measuring flowrate profiles. As the temperature in the wellbore is influenced by the properties and flowrate of the inflows from different entry points, measured temperature can be used to estimate flowrate. Therefore, the DTS data are very valuable for estimating flowrate profiles. In our study, we used two different inverse methods separately. Although the philosophy and performance of these two methods are different, both succeed in estimating flowrate profile from the temperature profile. The multiphase case was also considered, in which we found that it requires more input information than just temperature data to achieve a good estimate of flowrate profile.

3. Evaluating formation properties

Temperature is also a function of formation properties, and thus it can be used to evaluate the formation. We found that temperature data are more sensitive

to the properties in the near-well formation than pressure data. This finding is confirmed by our study on several different cases of single-layer reservoirs. Furthermore, multilayer and horizontal wells, both of which have multiple entry points in the well, were also studied. Finally, a successful analysis of a real case was helpful to verify our findings.

Contents

List of Tables

List of Figures

Chapter 1

Introduction

Temperature change plays an important role in many downhole processes, and temperature measurements have long been used to monitor the performance of producing wells, evaluate water-injection profiles and diagnose the effectiveness of fracture jobs, etc. However, for many years, the utilization of downhole temperature measurement was largely over-shadowed by other measurements obtained through sophisticated suites of logging tools. However, the development of fiber-optic technology has helped a resurgence of interest in temperature measurement.

One characteristic of fiber-optic temperature measurement is that it is capable of measuring multiple points simultaneously. The fiber-optic tool used to measure temperature is called a Distributed Temperate Survey (DTS), which measures temperature along the whole interval covered by the fiber. Because temperature in the wellbore is related closely to flow conditions, the distributed temperature data obtained from DTS are very valuable for downhole production surveillance.

As DTS is a newly-emerged technology, with significant potential applications in oil/gas wells, the objective of this research was to study the interpretation of DTS data and explore what reservoir and well information the temperature data indicate directly or indirectly. In this chapter, the DTS system is introduced, followed by the

outline of this dissertation.

1.1 Distributed Temperature Survey System

1.1.1 Basics about DTS

DTS monitoring was the first commercially successful optical monitoring service offered in the oil/gas market (Drakeley et al. 2006). According to Brown (2008), in the most basic form, a DTS system comprises a strand of optical fiber, a laser light source, an optical splitter, an optoelectronic signal-processing unit and a display unit (Figure 1.1). The core of fiber is very thin, 5-50 microns in diameter, and the core is surrounded by an protective layer of silica known as cladding, which has a different reflective index from the core.

The fiber is interrogated by a 10-ns lasers pulse (its equivalent interval length is 1 m). Because of the reflective index contrast between the core and cladding of the fiber, each laser pulse is reflected back along the boundary between the core and cladding. The backscattered light wavelength will be shifted through a phenomenon known as Raman backscattering. According to the Raman theory, the negative part of the backscattering shift, namely the anti-Stokes Raman backscattering, is temperature-dependent. The in-situ temperature can then be calculated by the intensity ratio between Stokes and anti-Stokes backscattered light. This process is illustrated in Figure 1.1.

The backscattered light is also analyzed to determine how far down the fiber it originated. Because each input pulse is 10-ns long, the interval from which the backscattered light originated will correspond directly to a specific meter-long segment of the fiber. Consequently, a log of temperature can be calculated at one meter intervals along the length of the fiber by using only the laser source, the analyzer and

a reference temperature with the surface system. In other words, a DTS system can obtain temperature profiles along the interval of the well that is covered by the fiber.

Comparing to traditional temperature logging methods, which are point-by-point measurements, DTS measures multiple points simultaneously. The unique advantages of DTS summarized by Pinzon et al. (2007) are as follows:

1. Minimize well intervention;

2. Sustain flow in high-production-rate wells;

3. Save cost;

4. Improve safety.

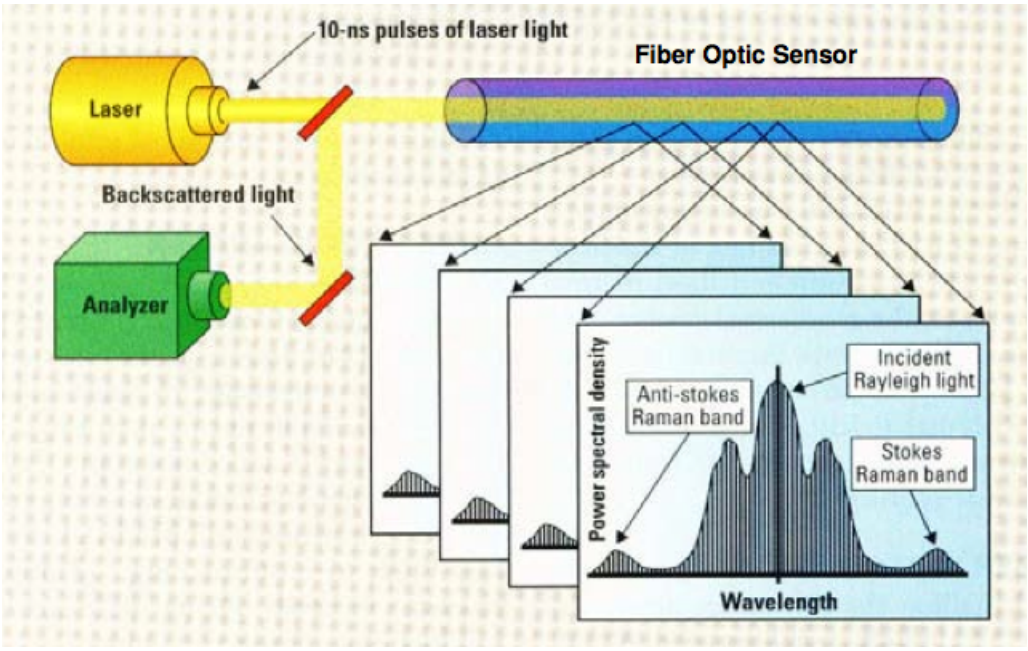

Figure 1.1: Sketch of a DTS system. (Al-Asimi et al., 2003)

1.1.2 Placement of Fibers

Due to the small size of optical fibers, various downhole installation methods of DTS can be applied. For our research, the installation method matters, because it determines what temperature profiles the fiber actually measures. Referring to Figure 1.2, there are three different temperature profiles to be considered:

1. Geothermal temperature: the original temperature profile of the formation, which depends on the thermal conductivity of the rock;

2. Entry temperature: the temperature of the fluid at the sandface (and thus referred as sand face temperature in some literature), before it enters the well and mixes with the fluid in the well. At the location where fluid flows into wells, the entry temperature is different from the geothermal temperature as a result of several thermal phenomena such as viscous dissipation and adiabatic expansion. In contrast, at the locations of no fluid flow, the entry temperature measured by DTS is the same as the geothermal temperature;

3. Mixing temperature: the temperature of the fluid in the wellbore, after mixing with the fluid coming from other entry points in the wellbore.

Several common installation methods relevant to our study are illustrated in Figure 1.3, 1.4 and 1.5.

The fiber can be attached to sand screens, as shown in Figure 1.3. The temperature measured by DTS is the mixing temperature. Similarly, in a vertical well installed with several inflow-control-valves (ICV) (Figure 1.4), the fiber is attached to tubing, and DTS also measures the mixing temperature. Alternatively, the fiber-optic can be installed permanently: being cemented, as shown in Figure 1.5. The temperature data obtained from this installation method are the entry temperatures.

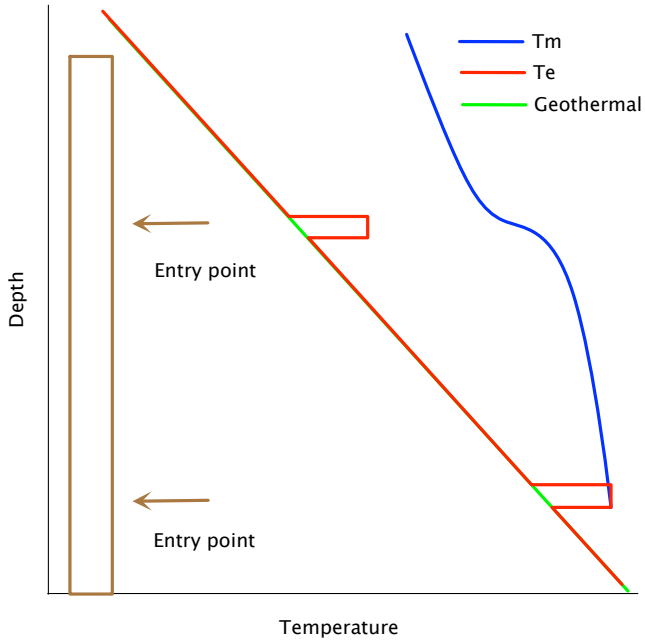

Figure 1.2: Three different temperature profiles, T_m = mixing temperature, T_e = entry temperature.

However, there is a potential risk associating with this installation method: the fiber-optic cable can be damaged during perforation. Therefore, in practice, to prevent the damage by perforation guns, several fiber optic strands are cemented at different locations around the wellbore.

1.2 Statement of Purpose

DTS technology has already been applied to operating fields. For example, James (2000) used DTS data to identify formation damage in a production field. Nath et al. (2005) present a case of a field using DTS data to monitor steam breakthrough in a steam-flooding project. As summarized by Drakeley et al. (2006), several potential uses of DTS are:

- Thermal profiling of well

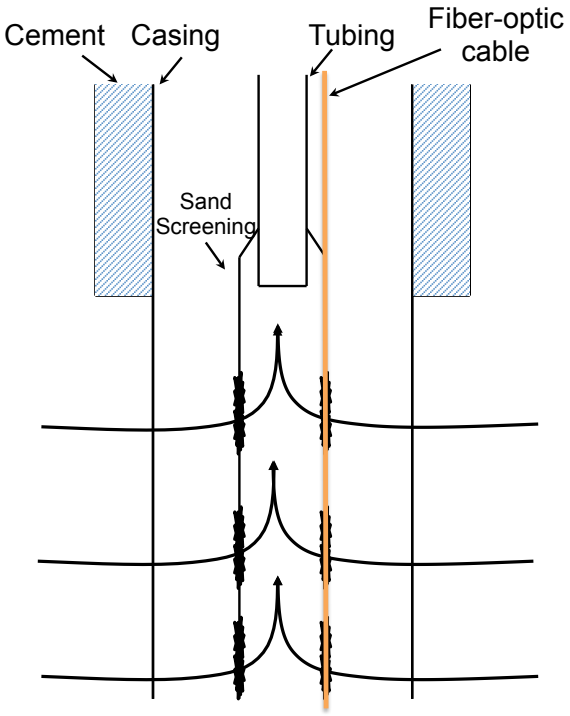

Figure 1.3: DTS installed in a sand screen completion.

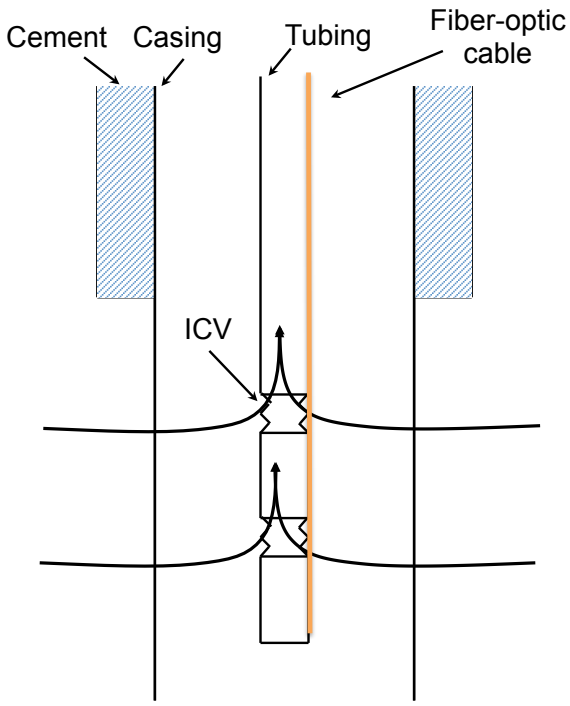

Figure 1.4: DTS installed in wells with inflow-control-valves.

- Production and injection profiling
- Identification of well problems
- Monitoring of water, gas, steam breakthrough
- Optimization of gas lift

In our study, we explored approaches of how to interpret DTS data. Our study did not cover all the applications listed above, but was focused in the following three directions:

1. Building a wellbore/reservoir coupled thermal model

   The model is capable of calculating pressure and temperature distribution both in the reservoir and the wellbore. This model can also handle multiphase flow,

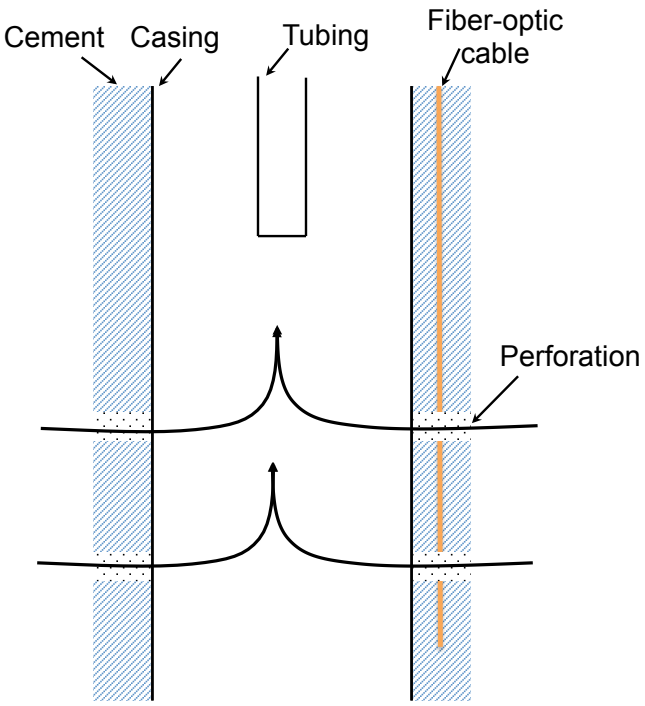

Figure 1.5: DTS is cemented.

in which thermodynamic properties of fluid are calculated by solving a compositional simulation problem. Flash calculation is performed and equations of state are solved to obtain the composition of the fluid at certain temperature and pressure. Moreover, a comprehensive list of underground thermal phenomena is modeled to ensure the accuracy of this model.

The details of building this mode, such as control equations and solution algorithms, etc. are explained in Chapter 4.

2. Estimating flowrate profile from temperature profile measurement

   Measuring flowrate profile can be a challenging job for traditional single-point flowrate measurement tools, and it becomes very unreliable especially for multiphase flow and complex well geometries. However, temperature profile provides an alternative approach for measuring flowrate profiles. As the temperature in

the wellbore is influenced by the properties and flowrate of the inflows from different entry points, measured temperature can be used to estimate flowrate. Therefore, the DTS data are very valuable for estimating flowrate profiles. In our study, we used two different inverse methods separately. Although the philosophy and performance of these two methods are different, both succeed in estimating flowrate profile from the temperature profile. The multiphase case was also considered, in which we found that it requires more input information than just temperature data to achieve a good estimate of flowrate profile. The inverse modeling results are shown in Chapter 5.

3. Evaluating formation properties

   Temperature is also a function of formation properties, and thus it can be used to evaluate the formation. We found that temperature data are more sensitive to the properties in the near-well formation than pressure data. This finding is confirmed by our study on several different cases of single-layer reservoirs. Furthermore, multilayer and horizontal wells, both of which have multiple entry points in the well, were also studied. Finally, a successful analysis of a real case was helpful to verify our findings. The details are elaborated in Chapters 6 and 7.

Chapter 2

Literature Review

2.1 DTS Application

The DTS system has become a compelling piece of permanent downhole monitoring equipment. Data acquired from DTS are interpreted qualitatively in some projects, e.g. Nath et al. (2005) used the DTS in a steam injection project to locate steam breakthrough zones and identify steam zone development, which provide valuable information for steam breakthrough management. Meanwhile, others tried quantitative interpretation of DTS data, e.g. Ouyang and Belanger (2006) provide a numerical approach to estimate flowrate profile from the temperature profile. They concluded that DTS data can be used to determine the production profile under certain circumstances like single-phase flow. However, under other more complicated circumstances, like multiphase flow or horizontal well, additional data may be required to perform flow profiling by DTS data. Brown et al. (2007) monitored production flowrate and change over time by DTS data in a real developing field. In their project, optic fiber was installed on the periphery of the sand-screening shroud, from which the fiber can measure the sand face temperature before it enters the well. Their novel manner of installation of DTS fiber makes them very useful when doing the flowrate profiling.

Brown et al. (2007) succeeded in estimating flowrate even after gas breakthrough which involves multiphase flow and changing gas/oil ratio.

2.2 Flow Modeling

Many papers have been published on the topic of the heat transfer between wellbore and formation. Ramey (1962) provided an analytical model to predict the temperature profile in an injection well. In that paper, Ramey presented a simple analytical equation for wellbore temperature based on a simplified heat balance. Apart from this analytical temperature equation, Ramey also proposed a simple procedure to estimate an overall heat-transfer coefficient for wellbore heat losses comprising both transient heat resistance in the formation and near-wellbore heat resistance. Despite its simplification, in practice Ramey's approach seems to work remarkably well (Jacques, 2004). Horne and Shinohara (1979) extended Ramey's model to production wells. These models succeed in predicting the temperature profile, given the entering temperature and flowrate. However, these analytical models are constrained to simple scenarios, like single phase and constant fluid-properties. Livescu et al. (2008) implemented a numerical multiphase thermal wellbore model, and it is fully coupled with a general purpose reservoir simulator. Ouyang and Belanger (2006) also built a numerical wellbore model, specially for DTS data interpretation. Using their wellbore model, Ouyang and Belanger (2006) succeeded in estimating flowrate profile by solving an inverse problem.

Reservoir dynamic thermal modeling is a relevant topic for DTS application. The research of heat transfer in porous media can also be traced back to Ramey. Atkinson and Ramey (1977) studied three mechanisms governing the energy transport of porous media flow: convection, conduction and storage of energy in the solid and fluid. Their study was based on the assumption of uniform and constant fluid flow

field, and thus the energy balance was uncoupled from mass balance equations. The governing equation, which is a diffusion-convection type Partial Differential Equation (PDE), is difficult to solve mathematically. By making assumptions to simplify fluid and formation interaction, Atkinson and Ramey derived an analytical solution. There has been much research effort spent in deriving analytical solutions to the diffusion-convection PDE. Neuringer (1968) used Greens functions to solve an instantaneous line source diffusing in a gravity field problem, and Yee (1990) gave an approximate analytical solution to the same problem. Ramaznov and Nagimov (2007) presented an analytical expression for the calculation of temperature distribution. In their work, they coupled the energy equation with flow equation, so temperature distribution can be calculated with variable pressures. However, they neglected the heat conduction term for mathematic convenience, and did not justify the consquence. Recently, Duru and Horne (2008) gave an analytical solution to a comprehensive reservoir thermal model. They considered heat conductive, convective mechanism and also other thermal phenomena, like viscous dissipation and adiabatic expansion heating/cooling effect. Their thermal model was coupled with the pressure equation, and solved by Operator Splitting and Time Stepping technique, which separately solved parabolic diffusion equation and hyperbolic convective equation at each time step and moved forward in time space.

Although the analytical approach has advantages of explicit expression, fast computation and high accuracy, it usually requires neglecting terms to simplify the problem, and it is not applicable to complicated scenarios. Under certain circumstances, a numerical method is preferred. Dawkragai (2006) derived a numerical multiphase model to predict temperature in a horizontal well. In his model, all the relevant mechanisms were considered, including multiphase flow. Based on the primary work of Dawkragai, Yoshioka (2007) analyzed entering fluid temperature in a horizontal well. Sui (2008) presented a method to determine multilayer formation properties

from DTS data, and concluded that layer permeability, damage permeability and damaged radius can be determined uniquely using single-point transient pressure data and transient distributed temperature data.

Based on the treatment of fluid PVT properties, numerical models can be categorized as black-oil models or compositional models. More specifically, in a black-oil model, the fluid PVT properties are treated as a single function of pressure and temperature, which means the PVT properties are interpolated from empirical relationships. While a compositional model is more general, it computes PVT properties from a function of in-situ composition, which is dependent on pressure and temperature. Stone et al. (1989), and Livescu et al. (2008) built black-oil models and Stone et al. (2002), Pourafshary et al. (2008) and Livescu et al. (2009) developed compositional models. However, our model differs from these compositional models. Stone et al. (2002) did not include slip between phases, which is an important phenomenon in multiphase flow. Pourafshary et al. (2008) did not consider transient effects in either the mass or energy conservation equations. Livescu et al. (2009) used the drift-flux model to capture the slip between phases. As stated in their paper, the drift-flux model is relatively simple, continuous and differentiable. Also in their model, the accumulation term was included to model the transient effects.

2.3 Inverse Modeling

To estimate flowrate or formation properties from DTS data is to solve an inverse problem. Different solution methods to interpret DTS data have been published. Sui et al. (2008) succeeded in using the least-square method to estimate formation properties from DTS data, while their discussion is constrained to commingled reservoir and single-phase flow. Zhuoyi et al. (2010) built a model to calculate pressure and temperature distribution in horizontal wells, and use traditional Markov Chain

Monte Carlo (MCMC) method to interpret the pressure and temperature data to obtain a flow-rate profile along horizontal wells. Their method was applied successfully to a real data set, and generated satisfactory results. Brown (2005) also succeeded in inverting flowrate profile from a real DTS data set, by using a neural-network optimization algorithm.

In a different approach, Kitanidis (1995) noted the suitability of using a stochastic model in solving the inverse problem. In contrast to deterministic methods, which yield a single answer based on the assumption that the data are perfect without errors, the stochastic method takes into consideration the imperfection both in data and forward model, and generates a series of solutions that are equally plausible candidates to be the actual values. In his paper, Kitanidis reviewed key concepts and equations related to the stochastic approach to inverse modeling, and discussed the challenge of striking a proper balance between resolution and noise suppression.

Chapter 3

Theory

In a flowing fluid, there are several heat transfer mechanisms controlling the temperature of the fluid. One mechanism that plays an important role is the Joule-Thomson effect. This mechanism relates the temperature change with the pressure change, and it is important for the inversion of formation properties using temperature data. In this chapter, we explain the Joule-Thomson effect and introduce the coefficient of this effect.

As stated in Chapter 1, one objective of this research was to estimate the flowrate and formation properties by temperature data, which requires solving inverse problems. One solution method we used is the quasilinear inverse model based on Bayes theory. The characteristic of this inverse model is that its estimate results strike a balance between data reproduction and noise suppression. The theory and formulation of this inverse model are explained in this chapter.

As noise is prevalent in data, denoising is a prerequisite step for most data analysis work. Temperature variations in the original data contain useful information as well as noise. The denoising method should be able to smooth out the variations at high frequency (noise), while keep the variations at low frequency (useful information). The wavelet method is able to examine the data sets at multiple resolutions, and a

desired level might be achieved. In this level, useful information is kept, on the other hand, noise is removed. The theory of wavelet analysis is explained in this chapter.

3.1 Joule-Thomson Effect

In thermodynamics, the Joule-Thomson effect describes the temperature change of a gas or liquid when it is forced through a valve or porous plug while kept insulated so that no heat is exchanged with the environment (Roy, 2002). The effect is named for James Prescott Joule and William Thomson, who discovered it in 1852.

1. Joule-Thomson Process

   The study of the dependence of the energy and enthalpy of real gases on pressure was conducted by Joule and Thomson. In their experiment, a sample of a gas, initially at P_1, V_1, and T_1 was forced through a porous plug at constant pressure, P_1. The gas came out of the other side of the plug at P_2, V_2, and T_2. The apparatus was insulated so that heat transferred with surrounding equals zero. The work has two terms: the work done on the system to force the gas through the plug and the work done by the system on the surroundings as it came out the other side of the plug.

   The total work is:

$$w = -p_1(0 - V_1) - p_2(V_2 - 0) = p_1V_1 - p_2V_2 \tag{3.1}$$

   As $q = 0$, the change in internal energy of the gas is:

$$\Delta U = q + w = 0 + p_1V_1 - p_2V_2 \neq 0 \tag{3.2}$$

   This process is not at constant internal energy. The enthalpy, however, is given

by:

$$\Delta H = \Delta U + \Delta(pV) = p_1V_1 - p_2V_2 + p_2V_2 - p_1V_1 = 0 \tag{3.3}$$

So the Joule-Thompson experiment is a process at constant enthalpy.

Consider a process that proceeds along a constant-enthalpy line in the direction of decreasing pressure. On the pressure-temperature diagram for a typical real gas shown in Figure 3.1, the process proceeds along a constant-enthalpy line from high pressures where the temperature increases, until the inversion temperature, after which, as the fluid continues its expansion, the temperature drops. If we do this for several constant enthalpies and join the inversion points, a line called the inversion line is obtained. This line intersects the T-axis at a certain temperature, named the maximum inversion temperature.

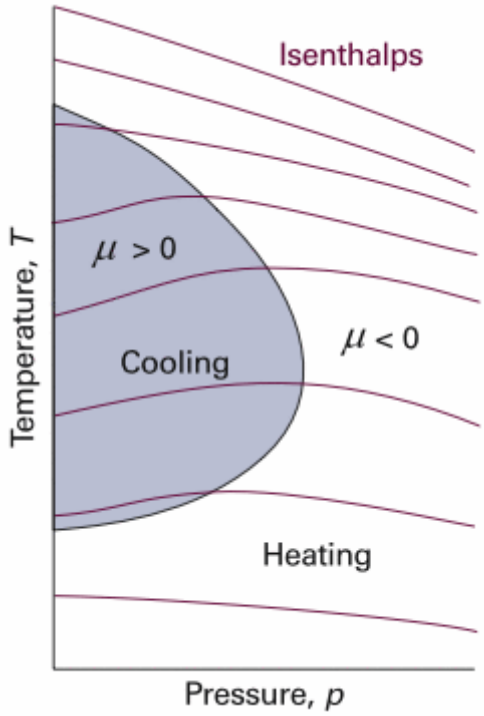

Figure 3.1: Pressure-Temperature diagram for a typical real gas. (Zemansky, 1968)

2. Joule-Thomson Coefficient

In the Joule-Thomson experiment, we could select a value for Δp, and then measure ΔT. The ratio of these two quantities is an approximation to a derivative.

$$\frac{\Delta p}{\Delta T} = \frac{\partial p}{\partial T} = \mu_{JT} \tag{3.4}$$

where μ_{JT} is defined as the coefficient of the Joule-Thompson effect.

$$\mu_{JT} = (\frac{\partial p}{\partial T})_{JT} = \frac{(\frac{\partial H}{\partial p})_T}{(\frac{\partial H}{\partial T})_p} = \frac{(\frac{\partial H}{\partial p})_T}{C_p} \tag{3.5}$$

where C_p is the heat capacity at constant pressure.

As:

$$dH = TdS + Vdp \tag{3.6}$$

$$(\frac{\partial H}{\partial p})_T = T(\frac{\partial S}{\partial p})_p + V \tag{3.7}$$

and we know that:

$$dG = VdpSdT \tag{3.8}$$

$$(\frac{\partial S}{\partial p})_T = (\frac{\partial V}{\partial T})_p \tag{3.9}$$

so Eq. 4.46 can be written as:

$$(\frac{\partial H}{\partial p})_T = V - T(\frac{\partial V}{\partial T})_p \tag{3.10}$$

Finally, we reach an expression to calculate Joule-Thomson coefficient:

$$\mu_{JT} = \frac{T(\frac{\partial V}{\partial T})_p - V}{C_p} \tag{3.11}$$

For a real gas, $(\frac{\partial V}{\partial T})_p$ can be obtained from any equation of state. If we use the van der Waals equation of state, as shown in Eq. 3.12:

$$pV = RT - \frac{a}{V} + bp + \frac{ab}{V^2} \tag{3.12}$$

the Joule-Thomson coefficient can be written as:

$$\mu_{JT} = \frac{(\frac{2a}{RT}) - b}{C_p} \tag{3.13}$$

Whether temperature increases or decreases during an adiabatic expansion depends on the sign of the Joule-Thomson coefficient μ_{JT} of the fluid. Because pressure always drops in an adiabatic expansion process, temperature increases if the sign of μ_{JT} is negative, while temperature decreases if the sign of μ_{JT} is positive. As shown in Eq 3.11, the Joule-Thomson coefficient depends on the temperature and pressure before expansion. As we mentioned earlier, at a certain point, μ_{JT} changes its sign. An example of the μ_{JT} values for nitrogen and helium at atmosphere pressure and at different temperature is shown in Figure 3.2. From the plot, we can see that helium's inversion temperature is 51K, while nitrogen's inversion temperature is 621K. At room temperature, helium has a negative Joule-Thomson coefficient while nitrogen has a positive one, which means that helium can be warmed from Joule-Thomson expansion and nitrogen can be cooled.

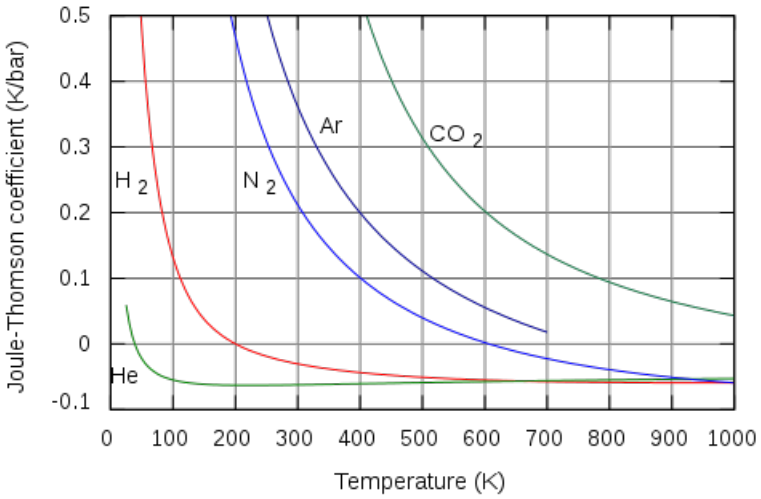

Figure 3.2: Joule-Thomson coefficient at various temperatures. (Zemansky, 1968)

3.2 Stochastic Inversion Based on Bayes Theorem

Physical theories allow us to make predictions: given a complete description of a physical system, we can predict the outcome of measurements. This problem of predicting the result of measurements is called the forward problem. The inverse problem consists of using the actual result of measurements to infer the values of the parameters that characterize the system. Unlike the forward problem which can give a unique solution in most cases, the inverse problem may not bear a unique solution, because often it is an ill-posed problem in the mathematical sense. To consider the inverse problems in a probability sense can help to solve the nonuniqueness. Rather than being considered as the chances of an event in repeated experiments in the classic statistics sense, probability can be regarded as a state of information in Bayesian statistics sense, which interprets probability in terms of a 'subjective' degree of knowledge of the 'true' value of a given physical parameter. By subjective we mean that it represents the knowledge of a given individual, obtained using rigorous reasoning, but that this knowledge may vary from individual to individual because each may possess different information (Tarantola, 2004). The subjectivity comes from the different opinions about the balance between how closely the data should be reproduced and how smooth the curve should be. There is no doubt that it is preferable that the forward model can generate results close to the data. However, as data are seldom perfect, and we believe that our model should bear a certain degree of smoothness, we can not achieve a satisfactory estimation by simply reproducing the data. In this section, we show a method to strike for a reasonable balance between 'data reproduction' and 'smoothness'.

The most general theory is obtained when using a probabilistic point of view, where the prior information on the model parameters is represented by a probability distribution over the 'model space'. The method shown here explains how this *priori*

probability distribution is transformed into the *posteriori* probability distribution, by incorporating a physical theory (relating the model parameters to some observable parameters) and the actual result of the observations (with their uncertainties). As summarized by Kitanidis (2007), this method can:

1. provide a representative solution that contains features common to all possible solutions;

2. provide a range of possible solutions and present a confidence interval;

3. provide many equally plausible solutions that are consistent with the data, yet different sufficiently to differ from each other.

In this section, the derivation of a linear inverse model is presented, and key concepts as well as the method to choose reasonable prior covariance are explained. Then, we will explain a linearization process which can extend the linear inversion applicable to quasilinear problems.

3.2.1 Linear Inversion

For illustrative purpose, we start our discussion of inverse modeling from the linear inversion.

Consider $s(x)$ is an unknown function that we want to estimate, e.g. flowrate in our case. $s(x)$ is modeled as:

$$s(x) = \sum_{k=1}^{p} f_k(x)\beta_k + \epsilon(x) \tag{3.14}$$

The first term is the prior mean, where $f_k(x)$ are known functions and β_k are unknown coefficients; the second term is a random function with zero mean and covariance function defined by our input. This linear model is versatile in the sense

that it includes the deterministic (the first term) and stochastic (the second term) terms. After discretization (like implementing a finite-difference model), $s(x)$ is an m by 1 vector, m is the grid number of unknowns. The mean of s is:

$$E[s] = X\beta \tag{3.15}$$

where X is a known $m \times p$ matrix, and β are unknown drift coefficients with the size of p. The covariance of s is:

$$E[(s-\mu)(s-\mu)^T] = Q \tag{3.16}$$

Q is usually parametrized through a variogram or generalized covariance function (GCF). Thus, Eq 3.14 can be written as:

$$s = X\beta + \epsilon \tag{3.17}$$

where ϵ has zero mean and covariance matrix Q.

The observation vector y (DTS data in our case) is related to the unknown vector s by the linear relation:

$$y = Hs + v \tag{3.18}$$

where H is an n by m given matrix (n is the number of data points, m is the number of grid cells); v is an error term, which is the deviations between observations and modeling results, with mean zero and covariance matrix R. Without the term v, the modeling results should match the observations exactly. However, because errors exist both in the measurement and our forward model, we need v to take this flaw into consideration.

3.2.2 Bayesian Analysis

We assume we already have a prior probability density function $p'(s)$, according to Bayes theorem, the posterior probability density function $p''(s)$ can be computed from the prior by weighting the likelihood, which is the probability density function of y given s, $p(y|s)$:

$$p''(s) = Cp(y|s)p'(s) \tag{3.19}$$

The C is a normalization factor to guarantee the probability density function integral has a value of 1.

As we assumed, the prior probability density function is Gaussian, and β is modeled as uniform over all space:

$$p'(s,\beta) \propto exp(-\frac{1}{2}(s - X\beta)^T Q^{-1}(s - X\beta)) \tag{3.20}$$

The likelihood function is:

$$p(y|s) \propto exp(-\frac{1}{2}(y - Hs)^T R^{-1}(y - Hs)) \tag{3.21}$$

Thus, the posterior probability density function is:

$$p''(s,\beta) \propto exp(-\frac{1}{2}(s - X\beta)^T Q^{-1}(s - X\beta) - \frac{1}{2}(y - Hs)^T R^{-1}(y - Hs)) \tag{3.22}$$

The negative logarithm of posterior probability density function is:

$$\frac{1}{2}(s - X\beta)^T Q^{-1}(s - X\beta) + \frac{1}{2}(y - Hs)^T R^{-1}(y - Hs) \tag{3.23}$$

Minimizing Eq 3.23 with respect to s and β is the same as achieving maximized posterior probability density function. Note that the first term in Eq. 3.23 represents a penalty for not reproducing data, and the second term represents a penalty for

deviating from the mean.

After algebraic derivation (the derivation process can be referred to Kitanidis, 2007), the posterior mean can be solved as:

$$\hat{s} = \Lambda y \tag{3.24}$$

where Λ functions, as a pseudoinverse of H, can be found by solving the following system:

$$\begin{bmatrix} \Psi & \Phi \\ \Phi^T & 0 \end{bmatrix} \begin{bmatrix} \Lambda^T \\ M \end{bmatrix} = \begin{bmatrix} HQ \\ X^T \end{bmatrix} \tag{3.25}$$

where the coefficient:

$$\Psi = HQH^T + R, \Phi = HX \tag{3.26}$$

$\hat{s}$ is the best estimate, and we can generate conditional realization by perturbation. The procedure to generate a conditional realization is as follows:

1. Generate an unconditional realization s_{ui} with zero mean and covariance matrix Q, a realization of the measurement error v_i with zero mean and covariance matrix R;

2. Then the conditional realization can be calculated by:

$$s_{ci} = s_{ui} + X\beta + QH^T\xi \tag{3.27}$$

ξ and β can be found by the solution of a system:

$$\begin{bmatrix} \Psi & HX \\ (HX)^T & 0 \end{bmatrix} \begin{bmatrix} \xi \\ \beta \end{bmatrix} = \begin{bmatrix} y + v - Hs_u \\ 0 \end{bmatrix} \tag{3.28}$$

3.2.3 Quasilinear Inversion

Linearization

Most practical applications are not linear, but most of these nonlinear problems can be reformulated in a way that allows us to use the linear equations described in Section 3.2.1. According to Kitanidis (2007), the model starts from a nonlinear relationship between y and s:

$$y = h(s) + v \tag{3.29}$$

We still assume a Gaussian distribution of error terms, with covariance matrix given by Q and R. The posterior probability density function can be written as:

$$p''(s, \beta|y) \propto exp\left[-\frac{1}{2}(y - h(s))^T R^{-1}(y - h(s)) - \frac{1}{2}(s - X\beta)^T Q^{-1}(s - X\beta)\right] \tag{3.30}$$

To achive the maximum-a-posteriori or MAP value, we must minimize the following negative log likelihood function:

$$L = \frac{1}{2}(y - h(s))^T R^{-1}(y - h(s)) + \frac{1}{2}(s^T G s) \tag{3.31}$$

in which,

$$G = Q^{-1} - Q^{-1}X(X^T Q^{-1} X)^{-1} X^T Q^{-1} \tag{3.32}$$

Then use successive linearization to minimize Eq. 3.31. We start from an estimation of $\tilde{s}$, and then use first derivative to approximate $h(\hat{s})$:

$$\tilde{H} = \frac{\partial h}{\partial s}|_{s=\tilde{s}} \tag{3.33}$$

$$h(\hat{s}) = h(\tilde{s}) + \tilde{H}(s - \tilde{s}) \tag{3.34}$$

The measurement equation may be written in the linear form:

$$y - h(\tilde{s}) + \tilde{H}\tilde{s} = \tilde{H}(s - \tilde{s}) \tag{3.35}$$

Then, we can use the linear inverse equations:

$$\tilde{\Psi} = HQH^T + R, \tilde{\Phi} = HX \tag{3.36}$$

$$\begin{bmatrix} \tilde{\Psi} & \tilde{\Phi} \\ \tilde{\Phi}^T & 0 \end{bmatrix} \begin{bmatrix} \tilde{\Lambda}^T \\ M \end{bmatrix} = \begin{bmatrix} \tilde{H}Q \\ X^T \end{bmatrix} \tag{3.37}$$

Then the estimate is:

$$\hat{s} = \lambda(y - h(\tilde{s}) + \tilde{H}\tilde{s}) \tag{3.38}$$

If $\hat{s}$ does not converge to $\tilde{s}$, we use $\hat{s}$ to update $\tilde{s}$ in Eq. 3.33 and repeat the process until convergence. The estimation obtained leads to the $maximum - a - posteriori$ value.

The covariance matrix of the posterior is hard to compute. However, there is a famous relation known as the Cramer-Rao lower bound stated as below:

$$V \geq -XM + Q - Q\tilde{H}^T\Lambda^T \tag{3.39}$$

We can use this lower bound as an approximation to the covariance matrix. Thus, the confidence interval can be calculated by:

$$s_i = \pm 1.96\sqrt{V_{ii}} \tag{3.40}$$

where s_i is the best estimate and V_{ii} is the diagonal elements of covariance matrix V.

Derivative Computation

Computation of the derivative $\tilde{H}$ (named sensitivity matrix or Jacobian matrix) is expensive, because usually the matrix itself has a large dimension ($n \times m$), and it involves forward simulation while building it. The computation effort can be reduced by choosing intelligently how to build the derivative matrix. As observation point number n is much smaller than grid number m, it is preferable to run the forward simulation n times rather than m times. The method is known as **adjoint-state** method, and is explained by the following example.

We assume our forward model is a partial differential equation solved by finite-difference method, and we have the following linear system:

$$A(s)\phi = b(s) \tag{3.41}$$

where s is the model parameter, i.e. flowrate in our problem, ϕ is data, i.e. temperature. Reformulate the equations to obtain:

$$\phi = A^{-1}b, \phi_i = e_i^T A^{-1} b \tag{3.42}$$

where e_i is a column vector with zeros everywhere except at row i where it is 1. The index of this nonzero term is determined by mapping the observation to the grid data. For example, in a one-dimensional problem, our observation locations are [3, 5], while our gridding locations are [1,2,3,4,5], so e_1 is an m-element column vector with 1 on the third element, 0 elsewhere; e_2 is an m-element column vector with 1 on the fifth element, 0 elsewhere.

Then,

$$\frac{\phi_i}{s_j} = e_i^T A^{-1} (\frac{\partial b}{\partial s_j} - \frac{\partial A}{\partial s_j}\phi) \tag{3.43}$$

Because the $\partial A/\partial s_j$ and $\partial b/\partial s_j$ are very sparse matrices, the term $(\partial b/\partial s_j - \partial A\phi/\partial s_j)$

can be calculated efficiently and stored into a matrix S in advance. We note that the $e_i^T A^{-1}$ is the most expensive part, as it requires inverting the big matrix A in forward modeling, and as in this adjoint-state method, we calculate n rows instead of m columns, so the computation is reduced a lot. We build the derivative matrix row by row, which involve n times inverting matrix A, and n times multiplication between $e_i^T A$ and jth column in matrix S.

3.2.4 Structure Parameters Selection

As discussed in Section 3.2.1, the prior covariance matrix is Q, while the error in measurement is also a Gaussian distribution, the covariance of which is R. The expressions for Q and R may involve parameters. For example, if the covariances are chosen as Eqs. 3.2.4 and 3.2.4.

$$Q_{ij} = -\theta_1 \left| x_i - x_j \right|, \theta_1 > 1 \tag{3.44}$$

$$R_{ij} = \theta_2, \theta_2 > 0 \tag{3.45}$$

There are two parameters known as θ_1 and θ_2 determining the behavior of the model, and these two parameters are *structural parameter*. In his paper, Kitanidis (2007) stated that θ_1 is to control the degree of smoothing in the obtained best estimate; the smaller the value of θ_1, the smoother the best estimate. Meanwhile, a larger θ_2 smooths the estimates and yields an estimate that reproduces the data less faithfully. Therefore, as discussed in Kitanidis (2007), by adjusting these parameters, one can produce different solutions. Most importantly,

- $\frac{\theta_1}{\theta_2}$ controls how closely measurements are reproduced and how finely $\tilde{s}$ is resolved. The higher the ratio, the more faithful the reproduction of the data and the more details appear in the estimate. However, choosing too high a value of this ratio will produce estimates that are excessively affected by noise and thus contain spurious features in the estimates.

- Multiplying both θ_1 and θ_2 but the same factor M^2 has no effect on the posterior mean $\tilde{s}$. However, it changes the posterior standard deviation and the spread of the conditional realization by factor M. Thus, the error estimates or range of possible solution depends on the choice of the structure parameters.

Kitanidis (2007) provides an objective approach to select the parameters. The idea is to find the parameters that maximize the probability of the data. Using the same probabilistic mode that we used to find the posterior of s, we can derive the probability density function of y given the vector of structural parameters θ. Then, using a well-established approach, known as restricted maximum a poserieri probability, we can find the parameters that maximize this expression for the actual data. The method of finding the structural parameter used by Kitanidis is cross validation. Consider an $(n - K)$ by n matrix P so that $P\Phi = 0$ and $P\Psi P^T$ is a diagonal matrix. Then, the transformed data $\sigma = Py$ have zero mean and covariance matrix $P\Psi P$ which is diagonal with entries σ_i^2 equal to the variances of δ.Then ϵ can be found through normalization, $\epsilon_i = \frac{\delta_i}{\sigma_i}$.

Note that P should be $(n - K)$ by n and verify that the imposed conditions are met. The significance of the generated transformed data is that they allow us to test the model and fit its parameters. The ϵ values are supposed to have zero mean and variance 1. The restricted maximum likelihood approach can be seen as a method to select parameters so that the variance is indeed near 1.

$$Q_2 = \frac{1}{n-K}\sum_{k=1}^{n-k} ln\epsilon_i^2 \tag{3.46}$$

By doing so, we select the right scaling for the parameters and thus find proper confidence intervals. Also the method of rest rived maximum likelihood finds the ratio of the parameters that optimizes the predictive ability of the model. Such a measurement is cR.

$$cR = Q_2 exp(\frac{1}{n-K}\sum_{k=1}^{n-k} ln\delta_i^2) \tag{3.47}$$

This is the geometric mean of the normalized variances of the delta residuals. The idea is that a good set of θ parameters should give small delta residual, which can be measured by the value of cR.

3.3 Wavelet Analysis for Data Denoising and Edge Identification

Noise is prevalent in data. Unlike 'perfect' synthetic data generated from forward models, data measured from the fields usually bear certain degrees of noise. Certainly, the noise in the data affect interpretation results. Noise disguises true phenomena, and sometimes, it leads to misunderstanding of the data. As we will show in Chapter 5, although some inverse models used in interpretation work are capable of handling certain degrees of noise in the data, denoising is still recommended as a prerequisite step for data interpretation.

In the DTS data we studied, we noticed that wellbore temperature will change abruptly at the fluid entry points. If we can identify these points, the number of unknowns in the inverse problem will be reduced by an order of magnitude, from the total

number of simulation grids (hundreds to thousands) to the number of entry points (often less than ten). Although most fluid enters the well through perforation points, the locations of which are documented by drilling engineers, there are always exceptions: the fluid might enter the well from unexpected entry points, the perforation-depth logging is not available and fluid enters the well through sand screens but not perforations, etc. Therefore, it is important to take the step of locating entry points on the DTS data, or 'edge identification'.

The desired result of denoising is that the data should be neither too noisy as the noise will ruin the interpretation, nor too smoothed as they will lose the abrupt changes at entry points. Wavelet analysis, which is a multiresolution signal processing method, was used in our study. Wavelet analysis decomposes the original signals into different resolutions until a desired level is achieved: at this level, the noise in the signal has been sufficiently suppressed while the information of entry points are preserved. The theory of wavelet analysis is introduced in this chapter, while the result of its application is discussed in Chapter 5.

3.3.1 Wavelet Theory

Wavelets are functions that satisfy certain mathematical requirements and are used in representing data or other functions. This idea originated from the Fourier transform which approximate a function by superposing sines and cosines. However, in wavelet analysis, the scale that we use to look at the data plays a special role. Wavelet algorithms process data at different resolutions. At each resolution, the signal is projected onto a continuous family of frequency bands. The frequency bands or subspaces (subbands) are scaled versions of a subspace. This subspace in turn in most situations is generated by the shifts of one generating function $\psi \in L^2(\mathbf{R})$, the **mother wavelet**.

The subspace of resolution a or frequency band $[1/a, 2/a]$ is generated by the

functions (sometimes called **child wavelet**):

$$\psi_{a,b}(t) = \frac{1}{\sqrt{a}}\psi(\frac{t-b}{a}) \tag{3.48}$$

where a is positive and defines the scale and b is any real number and defines the shift.

The projection of a function x onto the subspace of scale a then has the form:

$$x_a(t) = \int_{\mathbf{R}} WT_{\psi\{x\}}(a,b) \cdot \psi_{a,b}(t)db \tag{3.49}$$

with wavelet coefficients

$$WT_{\psi\{x\}}(a,b) = \int_{\mathbf{R}} x(t)\psi_{a,b}(t)dt. \tag{3.50}$$

It is helpful to think of the coefficients as a filter. The filter or coefficients are placed in a transformation matrix, which is applied to a raw data vector. The coefficients are ordered using two dominant patterns: one works as a smoothing filter (like a moving average), and the other works to bring out the detail information of the data.

Figure 3.3 and 3.4 show an example of the wavelet analysis by Mallat and Hwang (1992). The original data signal was passed through the low-pass and high-pass filters. As shown in the figure, at each level of decomposition, the approximated signal provides information on the overall features in the original data, while the detail signal describes changes in the signal on local scales. As the level of decomposition increases, the approximated signal gives coarser scale. This decomposition process can be continued until the desired level of coarseness is reached.

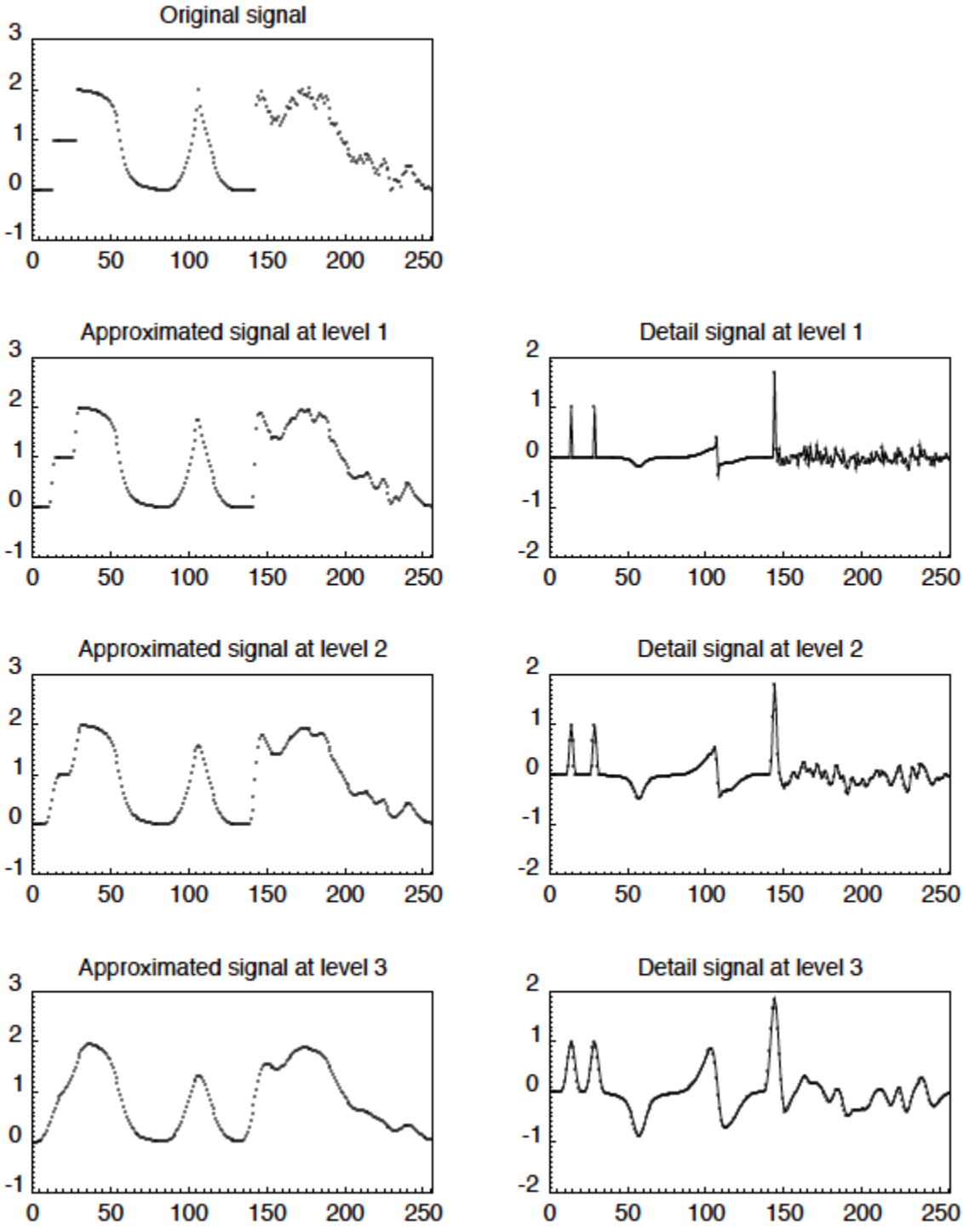

Figure 3.3: Wavelet decomposition. (Mallat and Hwang, 1992)

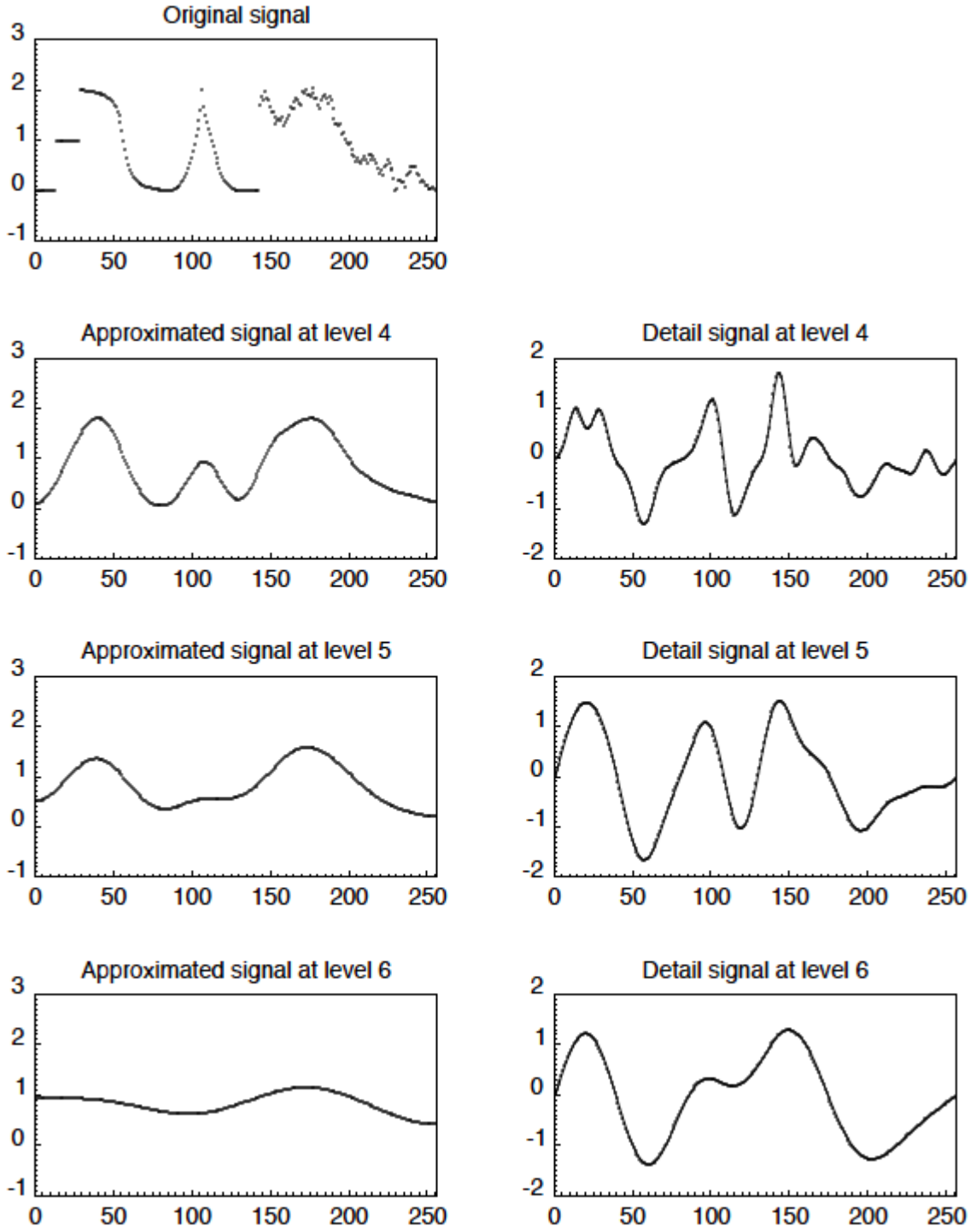

Figure 3.4: Wavelet decomposition (continued). (Mallat and Hwang, 1992)

3.3.2 Wavelet Transform Algorithm

It is possible to compute the wavelet transform in the time domain using Eq. 3.50. However, it is much simpler to use the fact that the wavelet transform is the convolution between the two functions x and Ψ, and to carry out the wavelet transform in Fourier space using the Fast Fourier Transform (FFT). In the Fourier domain, the wavelet transform is simply:

$$W_n(s) = \sum_{k=0}^{N-1} \hat{x_k} \hat{\psi}^*(s\omega_k) e^{i\omega_k n \delta t} \tag{3.51}$$

where the $\hat{}$ indicates the Fourier transform, and the Fourier transform of the time series is given by:

$$\hat{x_k} = \frac{1}{N} \sum_{n=0}^{N-1} x_n e^{-2\pi i k n/N} \tag{3.52}$$

To use this formula, the Fourier transform of the wavelet function should be known analytically. In addition, the wavelets must be normalized as:

$$\hat{\psi(s\omega_k)} = (\frac{2\pi s}{\delta t})^{1/2} \hat{\psi}_0(s\omega_k) \tag{3.53}$$

The steps to compute the wavelet transform for a time series are thus:

1. Choose a mother wavelet,
2. Find the Fourier transform of the mother wavelet,
3. Find the Fourier transform of the time series,
4. Choose a minimum scale s_0, and all other scales,
5. Perform the following for each scale:
   (a) Use Eq. 3.53 to compute the child wavelet at that scale;

(b) Normalize the child wavelet by dividing by the square-root of the total wavelet variance (the total of ψ^2 should then be one, thus preserving the variance of the time series)

(c) Multiply by the Fourier transform of your time series;

(d) Use Eq. 3.51 to transform back to real space.

3.4 Summary

In this chapter, we explained three preliminary theories to our research.

Firstly, the Joule-Thomson theory which relates the temperature change to the pressure change during a adiabatic process was explained. The direction and magnitude of the temperature change due to a pressure change of a certain type of fluid is determined by Joule-Thomson coefficient. The Joule-Thomson coefficient (μ_{JT}) of any fluid can be calculated through equation of state. Generally speaking, most gases have a positive μ_{JT}, and thus the temperature of the gas decreases when the pressure drops during a Joule-Thomson process; while most liquids have negative μ_{JT}, and have a temperature increase when the pressure drops. Therefore, the Joule-Thomson effect helps to identify the type of the fluid flowing into the well by monitoring temperature variations. Also, this effect is important for inverting formation permeability from temperature changes.

Secondly, the stochastic inverse model based on Bayes' theory was introduced. This inverse model is advantageous by having regulation parameters. The regulation helps the estimation result be at a reasonable balance between data reproduction and noise suppression. Also, this inverse model is a stochastic approach, which generates many equally plausible solutions that are consistent with the data. The theory of this model was introduced in this chapter, and the result is presented in Chapter 5.

Thirdly, wavelet theory was explained. This technique was used in our research

because its level-by-level ability of processing data. Wavelet can decompose data by several different levels, each of which has different a resolution. The desired level should smooth out the temperature variations at high frequency (regarded as noise), while the low-frequency variations are kept. These low-frequency variations on a DTS data set is important because they are corresponding to the entry points along the wells. This is elaborated later in Chapter 5.

Chapter 4

Wellbore/Reservoir Coupled Thermal Model

Wellbore temperature distributions are the results of nonisothermal transport of thermal energy and mass through both hydrocarbon-saturated reservoir (porous-medium flow) and wellbore (tube flow). There are several heat transfer mechanisms controlling this underground thermal phenomenon. For flow in a porous medium, heat is transported through conduction in the solid phase, conduction and convection in the fluid and conduction between solid phase and liquid phase. For flow in a wellbore, heat is transported through convection and conduction in the liquid phase, meanwhile is lost into the surrounding environment through conduction and radiation.

In order to understand the thermal phenomena of the underground flow, a wellbore/reservoir coupled thermal model is required. This model should be capable of computing temperature both in the wellbore and reservoir by considering comprehensive heat transfer mechanisms. The governing equations and solution methods of the model are explained in this chapter.

After our model was verified by comparing to published results, this model was used to conduct a series of sensitivity tests on different fluid and formation properties.

This process helped us find out the parameters to which the temperature signal is sensitive, which is a critical step for analyzing temperature data from distributed temperature measurement.

4.1 Modeling Procedure

The temperature distribution in the wellbore is a result of flow in the reservoir and in the wellbore. The reservoir model was built first, followed by the wellbore model. In both models, the governing equations are mass balance, momentum balance and energy balance equations. The formulation of each of these equations is explained, and then a numerical solution scheme and coupling method are presented.

4.1.1 Reservoir Pressure Model

Fluid flow in porous media can be modeled through three fundamental equations: Darcy's law, equations of state and mass balance. Darcy's law is expressed in Eq. 4.1:

$$u = \frac{\alpha}{\mu} k \nabla p \tag{4.1}$$

where $\alpha = 0.001127$, if all other quantities are in field units; e.g., pressure in psi, flowrate in bbl/day, velocity in ft/s, length in ft, permeability in md and viscosity in cp.

The fluid and rock are considered to be slightly compressible, which means rock porosity is a function of pressure. Isothermal rock compressibility is defined as:

$$c_R = -\frac{1}{V_p}(\frac{\partial V_p}{\partial p})_T = \frac{1}{\phi}(\frac{\partial \phi}{\partial p})_T \tag{4.2}$$

where V_p is the pore volume of the rock, and p is the pore pressure. Integrating

this expression subject to the condition $\phi_{(p^0)} = \phi^0$, where the superscript 0 denotes the reference condition, we obtain:

$$\phi_{(p)} = \phi^0 exp[c_R(p - p^0)] \tag{4.3}$$

The exponential can be expanded to give:

$$\frac{\phi}{\phi^0} = 1 + c_R(\Delta p + \frac{c_R(\Delta p)^2}{2} + \ldots) \tag{4.4}$$

Using a first-order approximation of this expansion, we obtain the porosity expressed as a function of pressure:

$$\phi = \phi^0(1 + c_R \Delta p) \tag{4.5}$$

If the reservoir is discretized by gridding into cells, as shown in Figure 4.1, in which x, y, z directions are denoted as cell i, j, k, the mass balance can be described as the mass flow rate $m_{i,j,k}$ across each interface between discretized cells plus the source term balance the mass accumulation $M_{i,j,k}$:

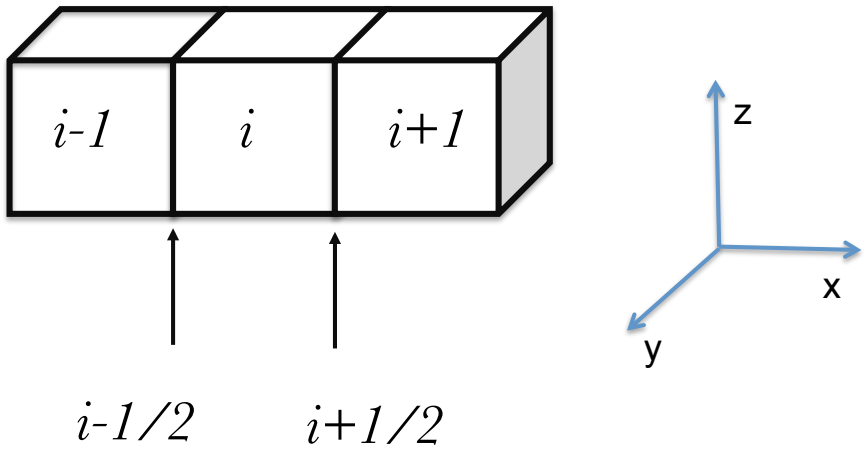

Figure 4.1: Gridding cells in x direction.

$$m_{i-1/2,j,k} - m_{i+1/2,j,k} + m_{i,j-1/2,k} - m_{i,j+1/2,k} + m_{i,j,k-1/2} - m_{i,j,k+1/2} - m^w_{i,j,k} = \frac{\partial M_{i,j,k}}{\partial t} \tag{4.6}$$

Each term in Eq. 4.6 is explained in the following.

1. Inflow and outflow term:

   Introducing Darcy's law gives:

   $$m_{i-1/2,j,k} = \rho^0 (\Upsilon_x)_{i-1/2,j,k} (p_{i-1,j,k} - p_{i,j,k}) \tag{4.7}$$

   where the x-direction transmissibility Υ_x is defined as:

   $$(\Upsilon_x)_{i-1/2,j,k} = \alpha(\frac{\Delta y \Delta z k_x}{B\mu \Delta x}) \tag{4.8}$$

   A similar expression can be formed for $m_{i+1/2,j,k}$.

2. Source and sink term:

   $$m_{i,j,k} = \rho^0 q^w_{i,j,k} \tag{4.9}$$

   where q^w is the wellbore volumetric flowrate.

3. Accumulation term:

   $$\frac{\partial M_{i,j,k}}{\partial t} = \frac{M_{i,j,k^{n+1}} - M^n_{i,j,k}}{\Delta t} = \frac{1}{\Delta} \Delta_t M_{i,j,k} \tag{4.10}$$

   where $M^n_{i,j,k}$ is

   $$M_{i,j,k} = \rho^0 \frac{V_{i,j,k} \phi^n}{5.615 B^n} \tag{4.11}$$

in which 5.615 is a unit conversion factor when the field unit system is used.

Hence the time difference can be written as:

$$\frac{\partial M_{i,j,k}}{\partial t} = \frac{1}{\Delta t}\rho^0 \frac{V_{i,j,k}}{5.615}(\phi^{n+1}c_f + b^n\phi^0 c_R)(p^{n+1} - p^n) \tag{4.12}$$

where p^n and p^{n+1} are the pressures at time steps n and $n+1$.

For multiphase flow, we used the Corey (1954) expression to describe relative permeability in oil/gas flow. The expression for oil relative permeability is:

$$k_{ro} = (\frac{S_o - S_{or}}{1 - S_{or}})^4 \tag{4.13}$$

and for gas relative permeability is:

$$k_{rg} = [1 - \frac{S_o - S_{or}}{S_m - S_{or}}]^2[1 - (\frac{S_o - S_{or}}{1 - S_{or}})^2] \tag{4.14}$$

where S_{or} is the residual oil saturation, S_m is the lowest oil saturation at which the gas tortuosity is infinite.

As an example, such a relative permeability curve is shown in Figure 4.2.

4.1.2 Reservoir Temperature Model

The solution of the reservoir energy balance equation gives temperature distribution in the reservoir. To derive the energy balance equation for a homogenous porous medium, the energy balance equations for the solid and fluid parts were derived separately from the first law of thermodynamics, and averaged over a control volume to obtain the general form of the model. If we assume that heat transfer between formation fluid and rock grains is instantaneous, which is an assumption verified by

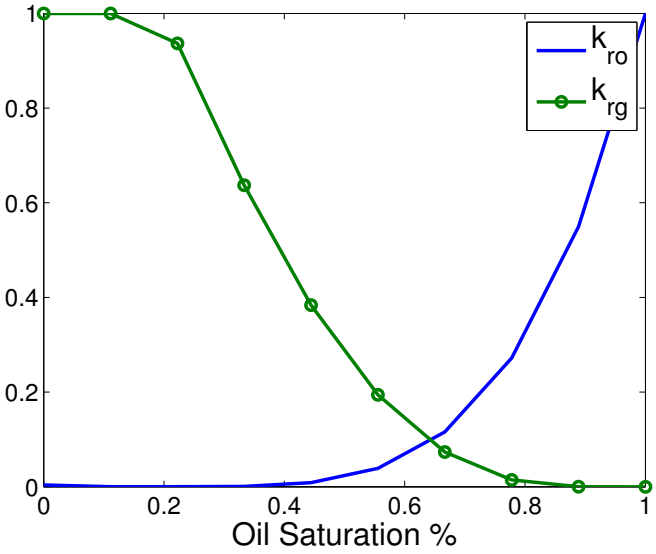

Figure 4.2: Example of relative curves calculated by Coreys equation ($S_{or} = 20\%$, $S_m = 90\%$).

Bejan (2004), the energy balance equation is written as:

$$\overline{\rho C_p}\frac{\partial T}{\partial t} - \phi\beta T\frac{\partial p}{\partial t} = \overline{k_T}\nabla^2 T - \rho c_p u\nabla T + (\beta T - 1)u\nabla p \tag{4.15}$$

where u is velocity, β is the thermal expansion coefficient and the over bars stand for the mean properties for the mixture of fluids and rocks. The discretized form of this equation is explained in Appendix B.

There are five terms in this equation, from left to right, these terms are: transient temperature variation, temperature change caused by temporal fluid expansion, heat conduction, heat convection, temperature change caused by spatial fluid expansion and viscous dissipation. The transient reservoir temperature is a function of mass flow rate. Moreover, due to the thermal effects like expansion and viscous dissipation, temperature variation is also affected by pressure change. Therefore, temperature data are related to the properties of the formation (e.g. permeability, porosity and

heat conductivity etc.) This fact provides us an opportunity to infer flowrate and formation parameters by using temperature data. A further sensitivity study on the relevant parameters in Eq.4.15 is helpful to understand the magnitude of temperature change to different parameter's change. The results of this sensitivity test are shown later in Section 6.3.

4.1.3 Wellbore Pressure Model

Total pressure gradient during wellbore flow is the sum of the static, friction and kinetic gradient, which is described by:

$$-\frac{dp}{dz} = g\rho_m + \frac{f_m V_m^2 \rho_m}{2d} + \rho_m V_m \frac{dV_m}{dz} \tag{4.16}$$

where f is friction coefficient, V is velocity, d is diameter of the flow path, z is the depth and the subscript m stands for mixing fluid.

1. Static gradient

   The mixture density is the volumetric-weighted average of different phases:

   $$\rho_m = \rho_g f_g + \rho_l (1 - f_g) \tag{4.17}$$

   where f_g is the in-situ volume fraction of the gas phase. The difficulty of using Eq. 4.17 comes from the fact that the volume fraction is often not equal to the ratio of the superficial gas velocity to the mixture velocity, although most homogeneous multiphase flow models assume so. To be more specific, the homogeneous model assumes:

   $$f_g = \frac{V_{sg}}{V_m} \tag{4.18}$$

   where V_{sg} means superficial velocity for gas.

However, due to the contrast of the flow properties between gas and liquid phases, flow is not 'homogeneous'. For example, in an oil/gas vertical flow, the gas phase moves faster than the liquid and has larger concentration in the center of the pipe. Thus, in-situ gas velocity is the sum of bubble rise velocity V_∞ and channel center mixture velocity $C_0 V_m$. An expression that combines these two mechanisms can be written as:

$$V_g = C_0 V_m + V_\infty \tag{4.19}$$

where V_g is the flow velocity of the gas phase, C_0 is the profile parameter, which describes the effect of the velocity and concentration profiles, V_m is the volumetric flux of the mixture, and V_∞ is the drift velocity of the gas, describing the buoyancy effect.

Noting that in-situ velocity is the ratio of superficial velocity V_{sg} to volume fraction f_g, thus f_g in Eq.4.18 can be calculated from Eq. 4.20, as long as we have the expressions for C_0 and V_∞. We used the values found by Hasan and Kabir (2007), listed in Table 4.1.

$$f_g = \frac{v_{sg}}{C_0 v_m + v_\infty} \tag{4.20}$$

2. Friction gradient

The friction factor in all flow patterns is estimated from mixture Reynolds number,

$$Re_m = v_m \rho_m d / \mu_m \tag{4.21}$$

in which viscosity μ_m is a mass-average mixture viscosity.

We used the Chen (1979) correlation to calculate friction factor, which is:

$$f_m = \frac{1}{[4log(\frac{\epsilon/d}{3.7065} - \frac{5.0452}{Re_m} log\Lambda)]^2} \tag{4.22}$$

where ϵ is roughness and Λ is:

$$\Lambda = \frac{(\epsilon/d)^{1.1098}}{2.8257} + (\frac{7.149}{Re_m})^{0.8981} \tag{4.23}$$

3. Parameters

The values of the profile parameter Co and the drift velocity V_∞ depend on the flow pattern, well deviation, flow direction and phases. The values and expressions, use by Hasan and Kabir (2007) are summaried in Table 4.1.

Table 4.1: Parameter for drift flux model (for upward cocurrent flow).

Flow Pattern	Flow Parameter C_0	Rise Velocity v_∞
Bubbly	1.2	$v_{\infty b}$
Slug	1.2	$\bar{v}_{\infty b}$
Churn	1.15	$\bar{v}_{\infty b}$
Annular	1.0	0

The parameters in Table 4.1 include:

$$v_{\infty b} = 1.53[g(\rho_l - \rho_g)\sigma/\rho_l^2]^{1/4} \tag{4.24}$$

where σ is the roughness of the tubing material.

and:

$$\bar{v}_{\infty b} = 0.35\sqrt{gD(\rho_l - \rho_g)/\rho_L}(F_\theta)(F_a) \tag{4.25}$$

in which, the well-deviation factor F_θ is given by:

$$F_\theta = \sqrt{cos\theta}(1 + sin\theta)^{1.2} \tag{4.26}$$

and the annulus factor Fa is given by:

$$Fa = (1 + \frac{0.29 d_i}{d_o}) \tag{4.27}$$

where subscript i is the inside of the well, and o is the outside of the well.

4. Pattern Transition Criteria

The use of the Hansan and Kabir drift flux parameters expression should be consistent with their pattern transition criteria (Hasan and Kabir, 2007). Transition from bubbly to slug flow occurs at the volume fraction exceeding a value of 0.25. Thus, the superficial gas velocity needed for transition from bubbly flow is:

$$v_{gb} = \frac{C_0 v_{sL} + v_\infty}{4 - C_0} cos\theta \tag{4.28}$$

However, bubbly flow will persists if the mixture velocity is higher than v_{ms}, given in the following expression (Shoham, 1982):

$$2 v_{ms}^{1.2} (\frac{f}{2d})^{0.4} (\frac{\rho_L}{\sigma})^{0.6} \sqrt{\frac{0.4\sigma}{g(\rho_L - \rho_g)}} = 0.725 + 4.15 \sqrt{\frac{v_{sg}}{v_m}} \tag{4.29}$$

Transition to churn flow from bubbly flow occurs when:

$$v_{sg} > 1.08 v_{sL} \tag{4.30}$$

Transition from churn to annular flow occurs when v_{sg} exceeds the value giving

by the following expression (Taitel et al., 1980):

$$v_{gc} = 3.1[g\sigma(\rho_L - \rho_g)/\rho_g^2]^{1/4} \tag{4.31}$$

5. Computational Algorithm

   We adhered to the following algorithm for assigning flow pattern to any computation cell in the top-down calculation approach. We assumed that at the wellhead, if v_{sg} is greater than that given by Eq. 4.31 and $f_g > 0.7$, then the flow pattern is assigned to be annular flow. We therefore followed this logic down the wellbore until Eq. 4.31 and/or $f_g > 0.7$ is no longer satisfied, at which point annular flow can no longer exist anywhere further down the wellbore.

A result from Hasan and Kabir (2007) showed that the drift flux model reproduced a set of field data more closely than the homogeneous model, as the comparison shows in Figure 4.3.

4.1.4 Wellbore Temperature Model

Energy transportation in the wellbore is governed by heat convection, heat conduction, source/sink and friction heating. By summing up all these terms, the energy balance in the wellbore can be written as Eq. 4.32:

$$c_p\rho\pi r_w^2\frac{\partial T}{\partial t} = c_p\rho\frac{\partial(qT)}{\partial z} + 2\pi r_w(\rho v_e c_p T_e) - 2\pi r_w U(T_w - T_r) + (\beta T - 1)q\nabla p \tag{4.32}$$

where r_w is the radius of the well.

The heat loss from the wellbore to formation is described by the total heat transfer coefficient U, which represents the total heat transfer resistance of the flowing fluid, tubing, casing annulus, casing wall and cement sheath to the heat flow, as shown in Figure 4.4.

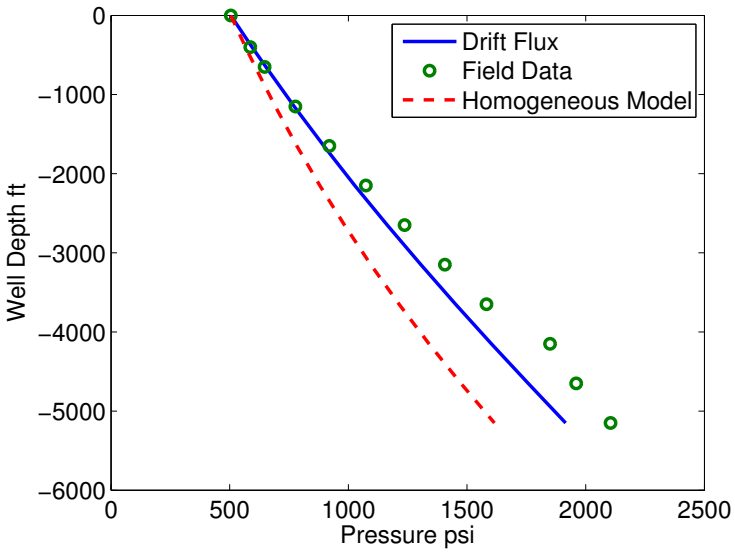

Figure 4.3: Comparison of drift flux model and homogeneous model, from Hasan and Kabir (2007).

We derived an expression for the overall heat transfer coefficient for the case of a hot fluid flowing through tubing insulated with a dry air annulus by considering different heat transfer mechanisms between the fluid and the formation.

The rate of heat transfer between the flowing fluid and the inside tubing wall is given by Eq.4.33:

$$Q = 2\pi r_{ti} h_f (T_f - T_{ti}) \Delta L \tag{4.33}$$

where h_f is heat transfer coefficient influenced by the fluid properties and temperature difference between the fluid and the inside tubing wall, and subscript f refers to fluid, ti refers to inner side of tubing.

Heat flow through the tubing wall, casing wall and the cement sheath occurred through conduction, which can be described by the Fourier law. Fourier discovered that the rate of heat flow through conduction is proportional to the temperature gradient in the medium, and the proportionality factor is termed the thermal conductivity

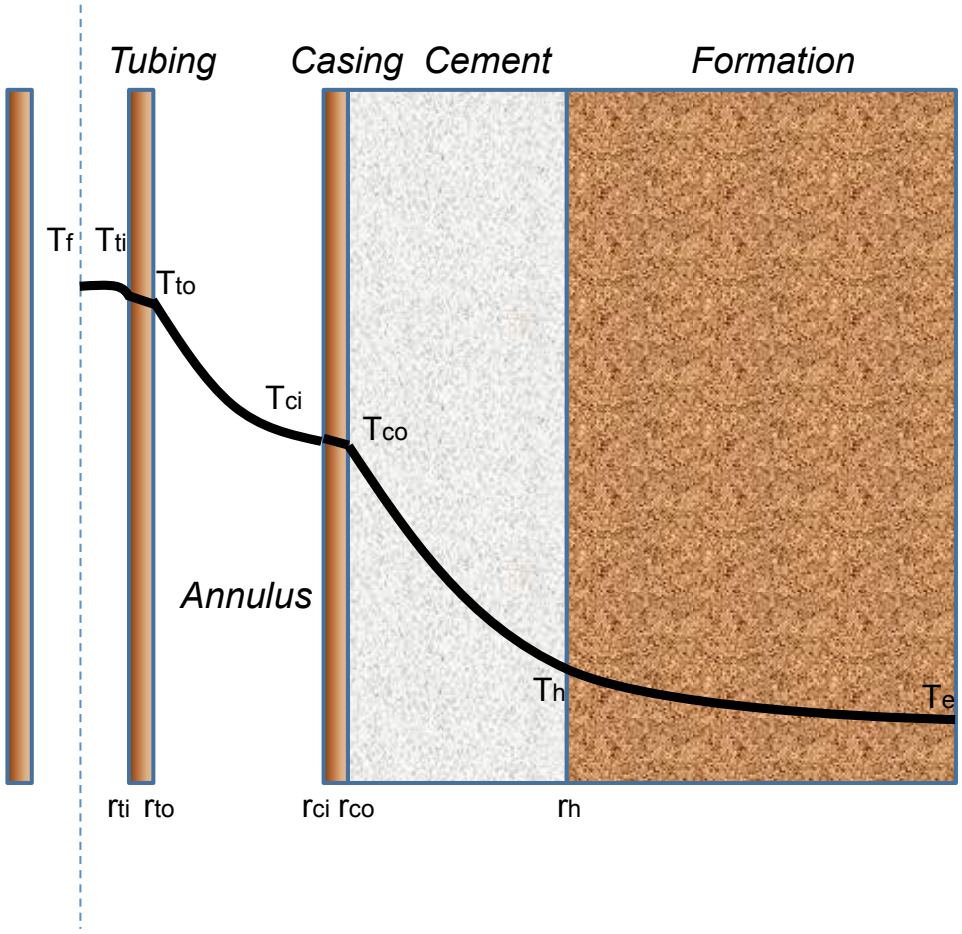

Figure 4.4: Sketch of wellbore geometry.

of the medium. In a radial system, heat flow rate is described by Eq. 4.34:

$$Q = -2\pi r k_h \frac{dT}{dr} \Delta L \tag{4.34}$$

Integration of Eq.4.34 with constant Q gives Eqs.4.35 to 4.37 for conduction through the tubing wall, casing wall and cement sheath:

$$Tubing : Q = \frac{2\pi k_{tub}(T_{ii} - T_{to})\Delta L}{ln\frac{r_{to}}{r_{ti}}} \tag{4.35}$$

$$Casing : Q = \frac{2\pi k_{cas}(T_{ci} - T_{co})\Delta L}{ln\frac{r_{co}}{r_{ci}}} \tag{4.36}$$

$$Cement : Q = \frac{2\pi k_{cem}(T_{co} - T_h)\Delta L}{ln\frac{r_h}{r_{co}}} \tag{4.37}$$

Three mechanisms govern the heat transfer in the annulus between tubing and casing: conduction of the air in the annulus, radiation and natural convection. Radiation is the phenomenon that a heated body emits energy, the rate of which is dependent on the surfaces area and the emitting and absorbing characteristics of each medium. Natural convection is the heat transfer caused by the fluid motion resulting from density variation at different temperatures. The total amount of heat flow is the sum of the heat transferred by each of these three mechanisms. In practice, it is convenient to define the heat transfer rate through the annulus in terms of the heat transfer coefficient h_c (natural convection and conduction) and h_r (radiation), and the heat transfer can be calculated by Eq. 4.38.

$$Q = 2\pi r_{to}(h_c + h_r)(T_{to} - T_{ci})\Delta L \tag{4.38}$$

where subscript *to* refers to outer side of tubing, *ci* refers to inner side of cement.

Note that:

$$T_f - T_h = (T_f - T_{ti}) + (T_{ti} - T_{to}) + (T_{to} - T_{ci}) + (T_{ci} - T_{co}) + (T_{co} - T_h) \quad (4.39)$$

As the heat flow is assumed to be steady-state at any particular time, the values of Q in Eqs 4.33 to 4.37 are equal. Solving for the respective temperature differences in these equations and substituting them into Eq.4.39 to give Eq. 4.40:

$$T_f - T_h = \frac{Q}{2\pi\Delta L}[\frac{1}{r_{ti}h_f} + \frac{ln\frac{r_{to}}{r_{ti}}}{k_{tub}} + \frac{1}{r_{to}(h_c + h_r)} + \frac{ln\frac{r_{co}}{r_{ci}}}{k_{cas}} + \frac{ln\frac{r_h}{r_{co}}}{k_{cem}}] \quad (4.40)$$

Then,

$$U = [r_{to}]^{-1}[\frac{1}{r_{ti}h_f} + \frac{ln\frac{r_{to}}{r_{ti}}}{k_{tub}} + \frac{1}{r_{to}(h_c + h_r)} + \frac{ln\frac{r_{co}}{r_{ci}}}{k_{cas}} + \frac{ln\frac{r_h}{r_{co}}}{k_{cem}}]^{-1} \quad (4.41)$$

Thus, U can be calculated once k_{tub}, k_{cas}, k_{cem}, h_f, h_r and h_c are determined. We followed the procedure of Willhite (1967) to determine these parameters. According to Willhite, the thermal conductivity of tubing and casing steel as well as film coefficient h_f in turbulent flow are much higher than other materials in the wellbore, and they can be removed from the equation without affecting the result much. Eq. 4.41 can be simplified to Eq. 4.42:

$$U = [\frac{1}{(h_c + h_r)} + \frac{r_{to}ln\frac{r_h}{r_{co}}}{k_{cem}}]^{-1} \quad (4.42)$$

1. Radiation h_r

   The radiant heat flux Q_r between the outer surface of the tubing at temperature T_{to} and the inside surface of the casing at T_{ci} can be calculated from the Stefan - Boltzmann law, as shown in Eq. 4.43:

$$Q_r = 2\pi r_{to}\sigma F_{tci}(T_{to}^{*4} - T_{ci}^{*4})\Delta L \tag{4.43}$$

The asterisk refers to absolute temperature in Rankine and σ is the Stefan-Boltzmann constant. F_{tcp} is the view factor representing the fraction of the radiation emitted from the external surface area of tubing A_{to}, which is intercepted by the inner casing surface area A_{ci}. This term relates the geometry of the wellbore and the emitting properties of the tubing and casing surfaces to the radiant heat flux. The emitting property of a surface is expressed in terms of its emissivity, a measure of its ability to absorb radiation. For a concentric annulus,

$$\frac{1}{F_{tci}} = \frac{1}{\overline{F}_{tci}} + (\frac{1}{\varepsilon_{to}} - 1) + \frac{A_{to}}{A_{ci}}(\frac{1}{\varepsilon_{ci}} - 1) \tag{4.44}$$

in which, ε_{to} and ε_{ci} are the emissivities of the external tubing and internal casing surface, respectively. $\overline{F}_{tci}$ is the overall interchange factor between the two surfaces. $\overline{F}_{tci}$ is 1 for wellbore heat transfer. The radiant heat flux Q_r can also be calculated by the equations in terms of heat transfer coefficient h_r:

$$Q_r = 2\pi r_{to} h_r (T_{to} - T_{ci})\Delta L \tag{4.45}$$

By comparing Eq. 4.43 and Eq. 4.45, h_r can be written as:

$$h_r = \sigma F_{tci}(T_{to}^{*2} + T_{ci}^{*2})(T_{to}^{*} + T_{ci}^{*}) \tag{4.46}$$

h_r can be calculated if T_{to} and T_{ci} are known.

2. Natural convection h_c

Heat transfer by conduction and natural convection between the inside casing surface and the outside tubing surface is given by Eq. 4.47.

$$Q_c = \frac{2\pi k_{hc}(T_{ci} - T_{to})\Delta L}{ln\frac{r_{ci}}{r_{to}}} \tag{4.47}$$

where Q_c is the heat transfer rate due to conduction and natural convection, and k_{hc} is the equivalent thermal conductivity of the annular fluid.

Dropkin and Sommersacles (1965) measured values of k_{hc} between enclosed vertical plates. Their data were correlated as a function of the Grashof (Gr) number and Prandtl (Pr) number of the annulus fluid, as shown in Eq.4.48.

$$\frac{k_{hc}}{k_{ha}} = 0.049(GrPr)^{0.333}Pr^{0.074} \tag{4.48}$$

where:

$$Gr = \frac{(r_{ci} - r_{to})^3 g\rho_{an}^2\beta(T_{to} - T_{ci})}{\mu_{an}^2} \tag{4.49}$$

$$Pr = \frac{c_{an}\mu_{an}}{k_{ha}} \tag{4.50}$$

Calculation of the radiation and natural convection coefficients requires knowledge of tubing and casing temperatures. Therefore, the estimation of overall heat transfer coefficient U starts with an initial guess. With this initial guess of U, the temperature of each interface can be calculated, and a new value of U can be estimated to update the initial guess. The final estimation of U can be given after the iteration converges. The iteration result of an example is shown in Figure 4.5.

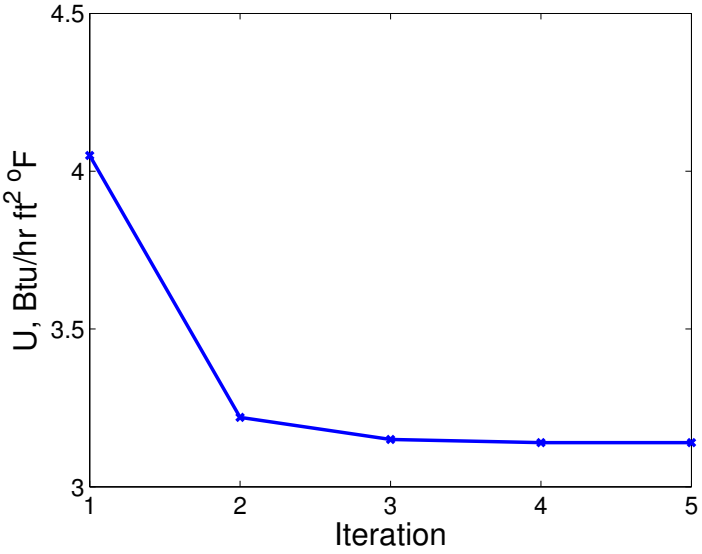

Figure 4.5: Iteration process of overall heat transfer coefficient U.

4.1.5 Compositional Modeling

Our model considers the fluid composition. The compositional model involves different hydrocarbon components: methane, ethane, propane, etc. and nonhydrocarbon: water. Those components can reside in three fluid phases: oil, water and gas. A system with N_c components has $(2N_c+4)$ unknowns and $(2N_c+4)$ equations. According to Livescu et al. (2009), the unknowns are: gas, water, oil phase volume fractions α_g, α_w, and α_o ; the wellbore pressure p^w and temperature T^w ; the mixture velocity (total volumetric flowrate divided by flow path area) V_m; the component mole fraction in the oil phase x_c, and in the gas phase y_c .

If the wellbore is discretized into N_s segments, (usually referred to as a multisegment well model), in each segment, there are $(2N_c + 4)$ equations to solve for these unknowns. We followed the approach of Livescu et al. (2009), and divided these equations into $(N_c + 2)$ primary equations and $(N_c + 2)$ secondary equations. The primary equations include N_c mass balance equations, one energy balance equation

and one pressure drop equation. All these primary equations of wellbore and reservoir were explained in detail in Section 4.1.1 to 4.1.4. Details of the secondary equations are explained next. The secondary equations are mainly for calculating mole fraction of each component in each phase, i.e. x_c and y_c , which are dependent variables determined by pressure, temperature and phase volume fractions. We notice that if we neglect these secondary equations, the model becomes a black-oil model.

These secondary equations are:

One in-situ volume fraction constraint:

$$\sum_p \alpha_p = 1 \tag{4.51}$$

Two mole fraction constraints for oil and gas phases:

$$\sum_{c=1}^{N_c} x_{cp} = 1, p = o, g \tag{4.52}$$

$(N_c - 1)$ phase equilibrium relations between oil and gas phases:

$$f_{c,o} = f_{c,g} \tag{4.53}$$

where $f_{c,o}$ and $f_{c,g}$ are the fugacities of component c in the oil and gas phases respectively.

By giving pressure and temperature, we can perform a flash calculation to determine the mole fraction in each phase of component c. The flash calculation proceeds in the following steps.

1. Initial guess of K value

   K is the ratio of mole fraction in gas phase to liquid phase, as shown in Eq.

4.54:

$$K_i = \frac{y_i}{x_i} \tag{4.54}$$

An empirical expression for K which is close to the true solution is given by the Wilson equation:

$$K_i = \frac{p_{ci}}{p} exp[5.37(1+\omega_i)(1-\frac{T_{ci}}{T})] \tag{4.55}$$

where T_{ci} and p_{ci} are the critical temperature and pressure and eccentric factor for component i.

2. Flash

With the K value and overall composition known, flash the mixture to determine the vapor and liquid compositions. For a two-phase system, a mass balance on 1 mole of mixture yields:

$$z_i = x_i l + y_i(1-l) \tag{4.56}$$

where l is the mole fraction of the mixture that is present as liquid phase.

We can then calculate mole fraction in each phase by the following equations:

$$x_i = \frac{z_i}{l+(1-l)K_i} \tag{4.57}$$

$$y_i = \frac{K_i z_i}{l+(1-l)K_i} \tag{4.58}$$

The sum of all mole fractions in each phase must be one, so:

$$\sum_i x_i - \sum_i y_i = 0 \tag{4.59}$$

Then we can substitute the expressions for x_i and y_i to obtain:

$$f(l) = \sum_i \frac{z_i(1 - K_i)}{K_i + (1 - K_i)l} = 0 \tag{4.60}$$

This equation is solved iteratively to obtain the liquid fraction and Eq. 4.57 and 4.58 are used to obtain the mole fraction the component i in liquid and vapor phase.

3. Equation of State (EOS) parameter

The phase compositions from Step 2 can be used to calculate all necessary parameters for the EOS. Recall that the EOS for a multicomponent system makes use of mixing rules that rely on phase compositions. We used the Peng-Robinson EOS to calculate fugacity coefficients and enthalpies for each component. We refer to Varavei et al. (2009) and Nasri and Binous (2009) for the expressions of Peng-Robinson EOS, the main features of which are described as follows.

$$P = \frac{RT}{\bar{v} - b} = \frac{a}{\bar{v}(\bar{v} + b) + b(\bar{v} - b)} \tag{4.61}$$

The parameters a and b for a pure component are computed from:

$$a = 0.45748 \frac{R^2 T_c^2}{P_c} \alpha\sqrt{\alpha} = 1 + f_w(1 - \sqrt{\frac{T}{T_c}}) \tag{4.62}$$

$$b = 0.07780 \frac{RT_c}{p_c} \tag{4.63}$$

For a multicomponent mixture, the mixing rules for the two parameters are:

$$a_{i,k} = \sqrt{a_i a_k}(1 - \delta_{ik}) \tag{4.64}$$

$$a_{m,j} = \sum_{i=1}^{n_c} \sum_{k=1}^{n_c} x_{ij} x_{kj} a_{i,k} \tag{4.65}$$

$$b_{m,j} = \sum_{i=1}^{n_c} x_{ij} b_i \tag{4.66}$$

where the constant δ_{ik} is called the binary interaction coefficient between components i and j.

$$A_j = \frac{a_{m,j} P}{(RT)^2} \tag{4.67}$$

$$B_j = \frac{b_{m,j} P}{RT} \tag{4.68}$$

Hence, by employing the related parameters for each phase, the compressibility factor for the phase is calculated.

$$\frac{\partial a_{m,j}}{\partial T} = \frac{1}{2} \sum_{i=1}^{n} \sum_{k=1}^{n} x_{ij} x_{kj} (a_i a_k)^{-\frac{1}{2}} (a_i \frac{\partial a_k}{\partial T} + a_k \frac{\partial a_i}{\partial T})(1 - \delta_{ik}) \tag{4.69}$$

$$f_w = 0.48 + 1.574w - 0.176w^2 \tag{4.70}$$

$$\begin{aligned} \frac{\partial^2 a_{m,j}}{\partial T^2} &= \sum_{i=1}^{n} \sum_{k=1}^{n} x_{ij} x_{kj} [-\frac{1}{4} (a_i a_j)^{-} \frac{3}{2} (a_i \frac{\partial a_k}{\partial T} + a_k \frac{\partial a_i}{\partial T}) \\ &\quad + \frac{1}{2} (a_i a_j)^{-\frac{1}{2}} (a_i \frac{\partial^2 a_k}{\partial T^2} + 2 \frac{\partial a_i}{\partial T} \frac{\partial a_k}{\partial T})](1 - \delta_{ik}) \end{aligned} \tag{4.71}$$

$$\frac{\partial a_i}{\partial T} = -\frac{0.442748 R^2 T_c^2}{p_c} [f_w \frac{1}{T_c^{1.5}} (1 - \sqrt{T_r})] \tag{4.72}$$

The expressions for fugacity coefficient and enthalpy are:

$$\varphi_i = exp(\frac{b_i}{b_m}(Z_i - 1) - Ln(Z_i - B) - \frac{A}{2\sqrt{2}B}(\frac{2\sum_j y_j A_{ij}}{A} - \frac{B_i}{B})Ln\frac{Z_i + (1+\sqrt{2})B}{Z_i + (1-\sqrt{2})B}) \tag{4.73}$$

$$H = RT(Z-1) + \frac{1}{2\sqrt{2}B\frac{RT}{p}}Log(\frac{Z + (1+\sqrt{2})B}{Z + (1-\sqrt{2})B})(T\frac{d}{d}(A\frac{(RT)^2}{p}) - A\frac{(RT)^2}{p}) \tag{4.74}$$

4. Solve EOS for vapor and liquid volume

   With all the necessary parameters known, the liquid and vapor volumes are computed using the EOS. It is easiest to compute the compressibility factor of each phase, Z^l and Z^v, and then calculate V^l and V^v with appropriate value of P, R and T.

5. Calculate liquid and vapor fugacities

   Once the liquid and vapor volumes are known, the fugacities are found simply by substituting into the appropriate expressions. Thus,

$$\hat{f}_i^l = \hat{f}_i^l(V^l, P, T, x_1, x_2, \cdots), \hat{f}_i^v = \hat{f}_i^v(V^v, P, T, y_1, y_2, \cdots) \tag{4.75}$$

6. Convergence

   The system is in equilibrium when:

$$f_i^l = f_i^v, i = 1, N_c \tag{4.76}$$

   Numerically, this means that the system can be considered converged when:

$$\left|\frac{f_i^l}{f_i^v} - 1\right| < \varepsilon \tag{4.77}$$

7. Updating K values

   If the system is not at equilibrium, new K values are estimated and the entire procedure is repeated. The easiest approach is the successive substitution by the following equation.

$$(K_i)^{k+1} = (\frac{f_i^l}{f_i^v} K_i)^k \tag{4.78}$$

   where the index k is the iteration count.

The primary equations and secondary equations are solved sequentially at each time step, and the iteration flowchart can be represented as in Figure 4.6. With a set of initial guesses of pressure and temperature, the secondary equations can compute the mole fraction of each phase, and calculate the fluid PVT properties, e.g. density and enthalpy. Then these PVT properties are used by the primary equations for calculating a new set of pressure and temperature, which is used to update the initial guess. This iterative process continues until convergence is achieved.

4.1.6 Numerical Solution Scheme

Both the equations of wellbore and reservoir were solved numerically by finite-difference method. To make it simpler to implement the numerical method, a gridding method based on a two-dimentional (both in reservoir radial direction r and depth direction z) radial coordinate system was generated, as shown in Figure 4.7.

To improve the efficiency of numerical method while preserving the accuracy, a nonuniform grid block distribution was used. The lengths of each grid follow a logarithmic sequence, and the radial distance can be defined through Eqs. 4.79 to 4.81 (Sui et al. 2008).

$$x = log_{a_{lg}}(r/r_w), x = i\Delta x, \Delta x = 1 \tag{4.79}$$

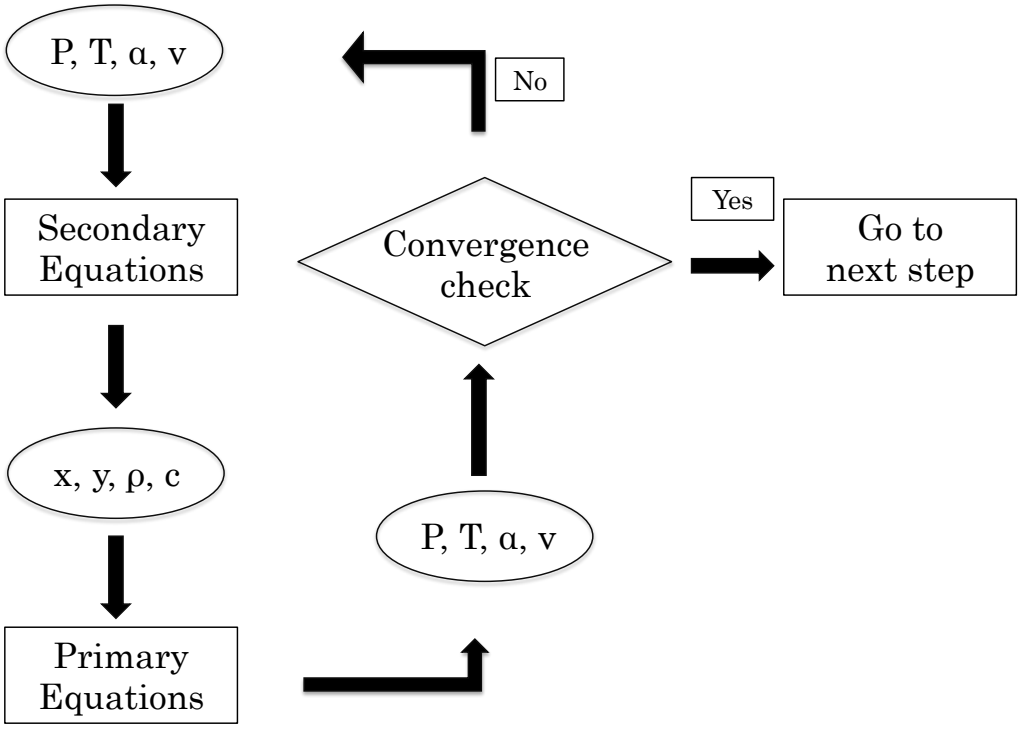

Figure 4.6: Flowchart of solving primary and secondary equations.

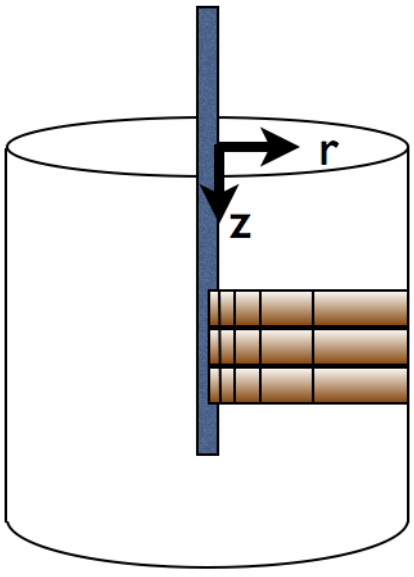

Figure 4.7: Radial coordinates and logarithmic gridding.

where a_{lg} is:

$$a_{lg} = (\frac{r_e}{r_w})^{\frac{1}{NR-1}} \tag{4.80}$$

where r_e is the radius of the reservoir, while r_w is the wellbore radius.

Thus, the radial distance is:

$$r_i = r_w a_{lg}^i \tag{4.81}$$

Subsequently, the partial derivatives of pressure and temperature with respect to space variables are given by Eqs. 4.82 to 4.84.

$$\frac{\partial T}{\partial r} = \frac{\partial T}{\partial x} \cdot \frac{1}{r ln a_{lg}} \tag{4.82}$$

$$\frac{1}{r}\frac{\partial}{\partial r}(r\frac{\partial T}{\partial r}) = (\frac{1}{ln a_{lg}})^2 \frac{1}{r^2}\frac{\partial^2 T}{\partial x^2} \tag{4.83}$$

$$\frac{\partial p}{\partial r} = \frac{\partial p}{\partial x} \cdot \frac{dx}{dr} = \frac{\partial p}{\partial x} \cdot \frac{1}{r ln a_{lg}} \tag{4.84}$$

Derivatives are approximated by finite differences. The first-order derivative is approximated by a forward difference and the second-order derivative by central differences:

$$\frac{\partial T}{\partial t} = \frac{T_{i,j}^{n+1} - T_{i,j}^{n}}{\Delta t} \tag{4.85}$$

$$\frac{\partial p}{\partial t} = \frac{p_{i,j}^{n+1} - p_{i,j}^{n}}{\Delta t} \tag{4.86}$$

$$\frac{\partial T}{\partial x} = \frac{T_{i+1,j}^{n+1} - T_{i-1,j}^{n+1}}{2\Delta x} \tag{4.87}$$

$$\frac{\partial p}{\partial x} = \frac{p_{i+1,j}^{n+1} - p_{i-1,j}^{n+1}}{2\Delta x} \tag{4.88}$$

$$\frac{\partial^2 T}{\partial x^2} = \frac{T_{i+1,j}^{n+1} - 2T_{i,j}^{n+1} + T_{i-1,j}^{n+1}}{\Delta x^2} \tag{4.89}$$

The initial temperatures in the reservoir and wellbore are the same as the geothermal temperature. Initial pressure of the reservoir can be set with different values in different cases. The reservoir boundary condition is set to be no-flow.

The mass balance equation Eq. 4.6, which is a first-order convection equation, is different from the energy balance equation Eq. 4.15, which is a second-order convection-diffusion equation. We used the implicit Euler scheme (Eq. 4.90) to solve the mass balance, and linearization by Jacobian matrix (Eq. 4.91) to solve the energy balance.

A general form of the implicit Euler method used in time stepping is stated in Eq. 4.90:

$$\frac{dy}{dt} = f_y y^{n+1} = y^n + \Delta t f_{y^{n+1}} \tag{4.90}$$

Linearization can be described as follows:

$$(I - \frac{h}{2}A_n)u^{n+1} = (I - \frac{h}{2}A_n)u^n + \frac{h}{2}[f(u^{(n)}, t_n) + f(u^{(n)}, t_{n+1})] \tag{4.91}$$

where:

$$A = \begin{bmatrix} \frac{\partial f_1}{\partial u_1} & \frac{\partial f_1}{\partial u_2} & \cdots & \frac{\partial f_1}{\partial u_m} \\ \vdots & & & \vdots \\ \frac{\partial f_m}{\partial u_1} & \frac{\partial f_m}{\partial u_2} & \cdots & \frac{\partial f_m}{\partial u_m} \end{bmatrix}_{u^n, t_{n+1}} \tag{4.92}$$

The input information into this model is total phase rate at the surface (then the well is total-flowrate-control), initial geothermal temperature, initial pressure,

rock and fluid thermal and flowing properties. The unknowns would be pressure and temperature distributions in the reservoir and wellbore, and the flowrate profile in the wellbore.

4.1.7 Couple Wellbore and Reservoir Models

The wellbore and reservoir are always coupled in practice, as they provide pressure and temperature boundary conditions for each other. We used different methods for coupling pressure and temperature.

The pressure equations of wellbore and reservoir can be combined into a single coefficient matrix, and the pressure in the wellbore and reservoir can be solved simultaneously. For illustration, we show an example of a well producing from two layers, as sketched in Figure 4.8. The total fluid production rate at the surface is specified, and the flowrates from each layer is summed up to the total flowrate, as shown in Eq. 4.93:

$$Q^w = \Upsilon^w[p_1 - p_1^w] + \Upsilon^w[p_2 - p_2^w] \tag{4.93}$$

where Q^w is the total flowrate from the well, Υ^w is well transmissibility defined in Eq 4.8, p_1 is the pressure at the center of gridding cell 1, p_2 is the pressure at the center of cell 2, and p_1^w and p_2^w are wellbore pressure at cell 1 and 2. These two pressure are related to a reference pressure p^w, which is usually set to be the pressure at the wellhead, as in Eqs. 4.94 and 4.95.

$$\Delta p_1 = p_1^w - p^w \tag{4.94}$$

$$\Delta p_2 = p_2^w - p^w \tag{4.95}$$

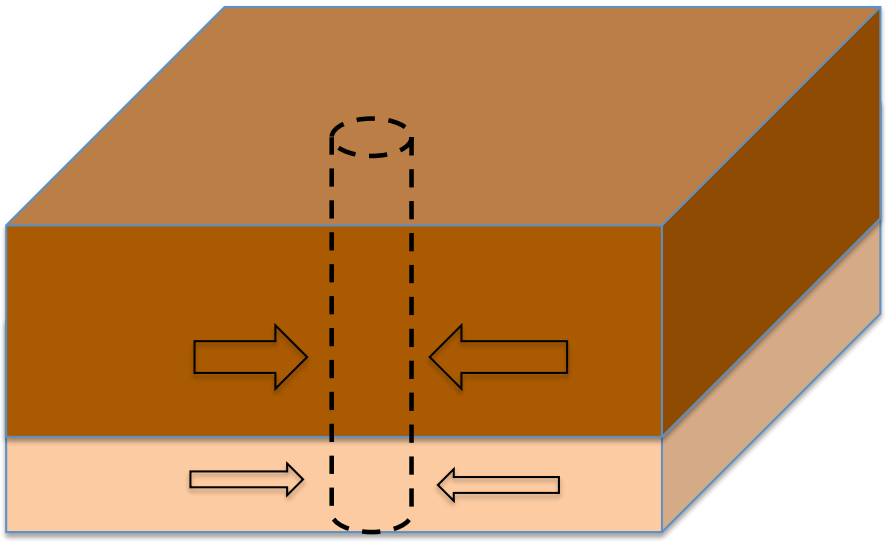

Figure 4.8: A well producing from two layers.

The pressure drop in the wellbore can be calculated by the drift-flux model we explained in Section 4.1.3.

Comparing with a well producing from a single layer, the case of a well producing from multiple layers has an additional unknown p^w and an extra equation residual Eq. 4.93. If there are six gridding cells, as shown in Figure 4.9, there are totally seven unknowns for a single-phase problem. For the finite-difference method, the coefficient matrix A and the unknown vector x of the linear system $Ax = b$ will be in the format as shown in Figure 4.10.

Rather than solving simultaneously for the pressure in wellbore and reservoir, we used a sequential solution method to couple the temperature in the wellbore and reservoir. We know that the wellbore and reservoir interact in two ways: the reservoir supports energy transport into the well by inflow of fluid at temperature T_e, or entry temperature (T_e is a part of the source term in Eq. 4.32), which is the interaction between *Region* 1 and 2 in Figure 4.11; meanwhile, the wellbore loses heat into the reservoir, which occurs between *Region* 2 and 3 in Figure 4.11. The

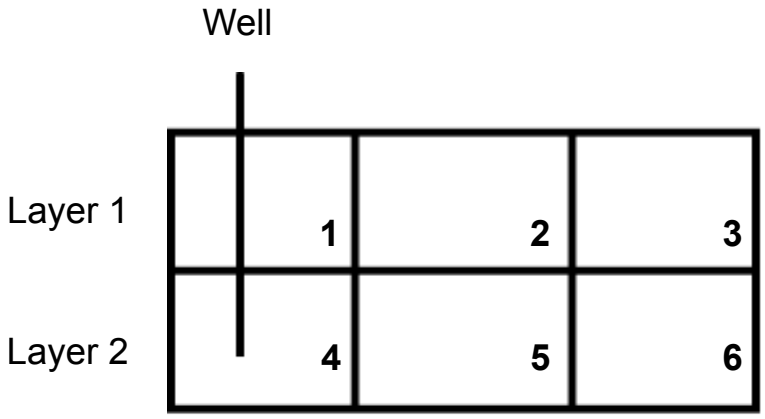

Figure 4.9: Gridding cells of a well in two layers.

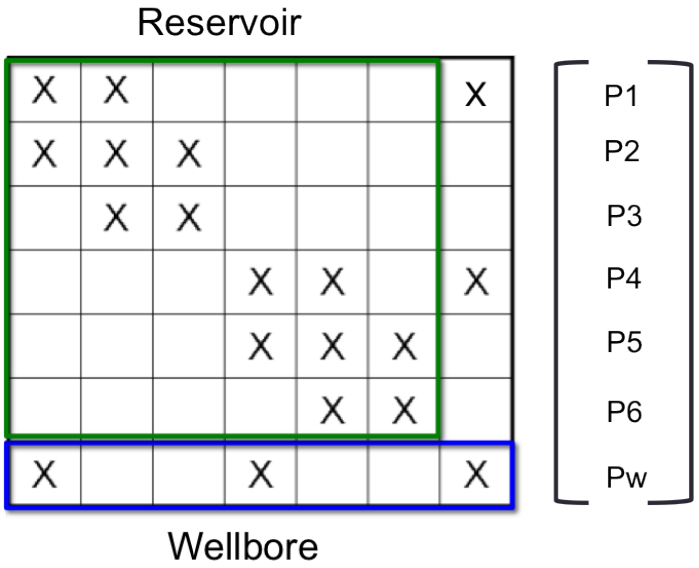

Figure 4.10: Coefficient matrix and unknown vector for a well in two layers.

temperature distribution in the reservoir is solved first, which can give us a value of entry temperature T_e, and then considering this T_e as a boundary condition, the wellbore temperature model can be solved.

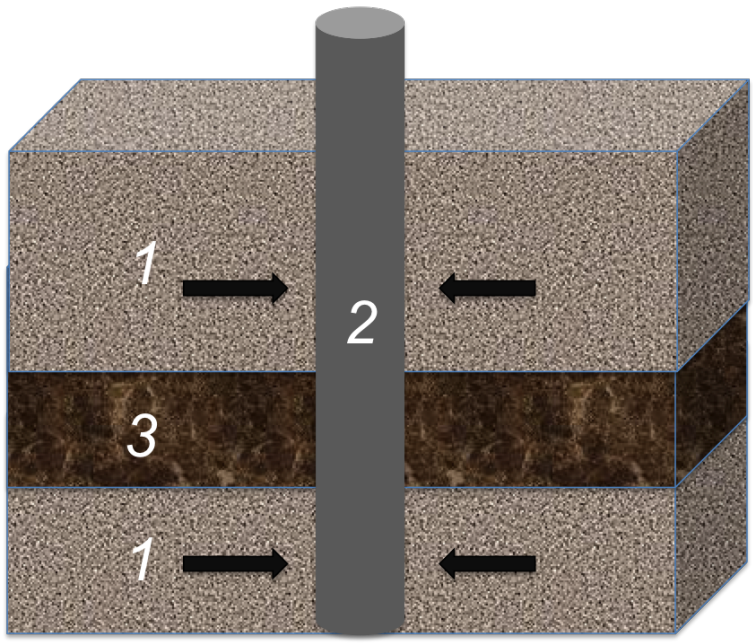

Figure 4.11: Sketch of two producing layers reservoir. (*Region* 1- Hydrocarbon-bearing layer, *Region* 2-Wellbore, *Region* 3-Shale layer)

One assumption made here is that the heat transfer between *Region* 1 and *Region* 3 in Figure 4.11 is not calculated, in other words, the boundary conditions for solving energy equations in *Region* 1 and 3 are no-heat-flow. The consequence is that the calculated temperature at the boundary of *Regions* 1 and 3 might be different.

In summary, the coupling method is shown as the flowchart in Figure 4.12. Pressures in the wellbore and reservoir are solved first, in which a matrix formed as in Figure 4.10 is solved. The pressure difference between the inside and outside of the wellbore can then be used to calculate the flowrate profile. After we have the pressure distribution in the reservoir, the temperature distribution in the reservoir can be solved, to obtain the entry temperature T_e. Finally, through the wellbore temperature

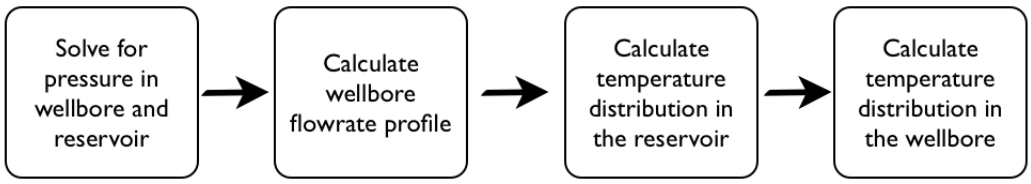

Figure 4.12: Flowchart of solving pressure, flowrate and temperature.

model, the wellbore temperature profile is calculated.

4.2 Model Outputs and Verification

The model can compute the pressure and temperature distribution in the reservoir and wellbore both in temporal and spatial dimensions, in other words, it simulates the transient phenomena and distributed phenomena in the reservoir and wellbore. We used Case 1-A.1 to show the simulation result, which is a single-phase oil well producing from two layers. The properties of fluid and reservoir are listed in Table 4.2, and the simulation parameters are listed in Table 4.3. The simulated results in the reservoir domain were studied first, followed by the wellbore domain. Then, we verified our model by comparing with results published in the literature.

4.2.1 Outputs in Reservoir Domain

When the fluid is flowing towards the wellbore, the pressure drop in the wellbore diffuses into the reservoir. During the radial flow period, the pressure distribution in the reservoir shows a straight line on semilog plot of pressure in temporal and spatial dimensions, i.e. p vs. t and p vs. r, as shown in Figure 4.13. By contrast, the process of energy transportation is a convection-conduction process. Therefore, the temperature distribution in the reservoir is not a strictly straight line on a semilog plot

Table 4.2: Parameter for Case 1-A.1.

Permeability of upper and lower layer $[md]$	5/20
Porosity [%]	0.5
Reservoir radius $[ft]$	1000
Distance between two layers [ft]	300
Layer thickness $[ft]$	1500
Wellbore depth $[ft]$	5000
Fluid density $[kg/m^3]$	800
Heat capacity $[J/kg/K]$	1880
Thermal conductiivty $[W/m/K]$	0.05
Thermal expansion coefficient β $[1/K]$	1.2e-6
Viscosity $[cp]$	2
Rock thermal conductivity $[W/m/K]$	0.25
Rock solid density $[kg/m^3]$	2300
Rock bulk density $[kg/m^3]$	1550
Total flowrate $[bbl/day]$	2500

Table 4.3: Simulation configuration for Case 1-A.1.

Cell number in well depth direction	100
Cell number in reservoir radius direction	50
Time step $[days]$	0.02

of T vs. t and T vs. r, as shown in Figure 4.14. Another difference between Figure 4.13 and Figure 4.14 is that the temperature signal at the wellbore is transported into the formation at much slower rate than the pressure signal. At the time that pressure has diffused around 200 ft into the formation (shown in the lower right plot in Figure 4.13), the temperature is only transported around 10 ft into the formation (shown in the lower right plot in Figure 4.13), which means the investigation radius of the temperature signal is much smaller than that of pressure signal. In other words, temperate data are more suitable for evaluating the $near - wellbore$ formation than are the pressure data.

During the process of energy transportation from reservoir to the wellbore, due to the viscous dissipation and adiabatic expansion, the temperature of the oil increases when it flows towards the well, as shown in Figure 4.14. As we mentioned in Chapter 3, Joule-Thomson coefficient μ_{JT} is usually negative for gases, resulting in a cooling effect when pressure drops. Therefore, the temperature decreases towards the wellbore for a gas well, as shown in Figure 4.15.

4.2.2 Outputs in Wellbore Domain

Case 1-A.1 has two production layers, with total flowrate at the well head specified, and the simulation takes a while for the two layers to stabilize after production, as shown in the simulation result of flowrate in each layer (Figure 4.16). The distribution of temperature in the wellbore shows a 'dip' at the location of the entry point (Figure 4.17), which is a signature that can be used to invert flowrate profiles from temperature profiles. The temperature heats up as production continues, as shown in Figure 4.17. This heating-up is sustained by two sources: 1. more hot fluid from the lower layer enters the well; 2. the temperature in the reservoir heats up as the pressure drop increases. When flow is stopped, these two heating sources disappear, and the temperature decreases. As in Case 1-A.2, which has a shut-in periods, the

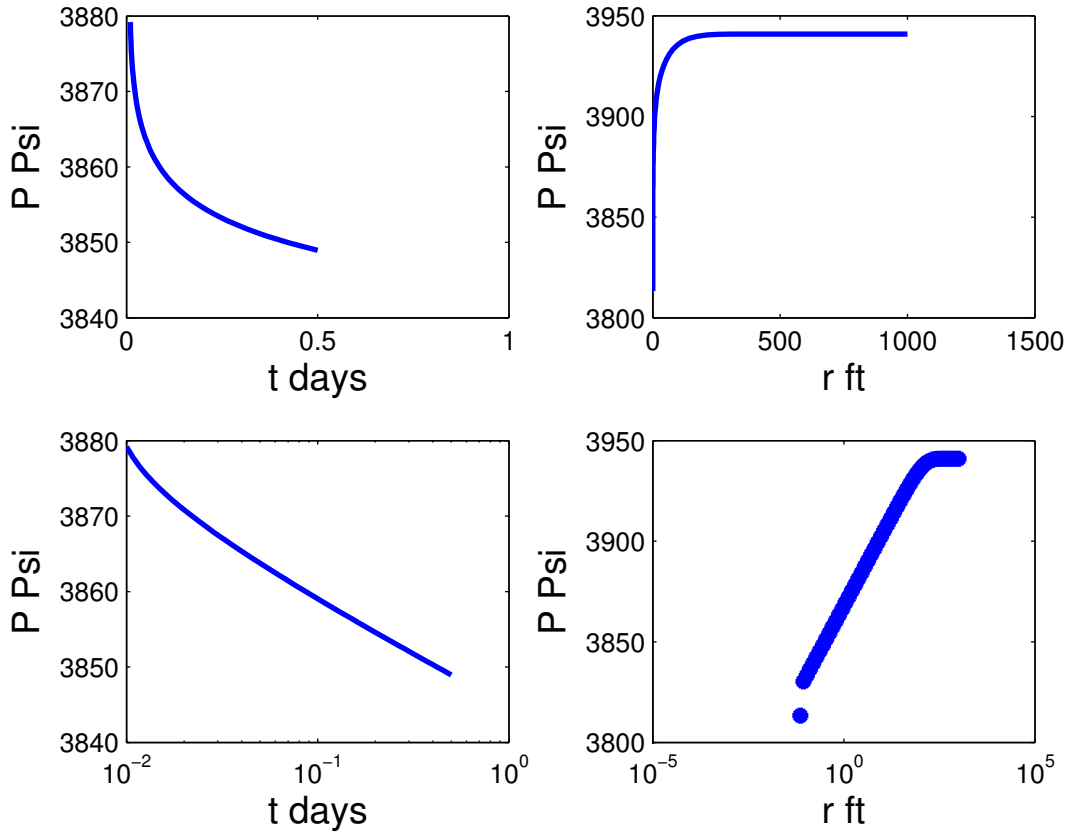

Figure 4.13: Cartesian plot (two plots at the top) and semilog plot (two plots at the bottom) of pressure in spatial and temporal dimensions during radial flow, single-phase oil flow

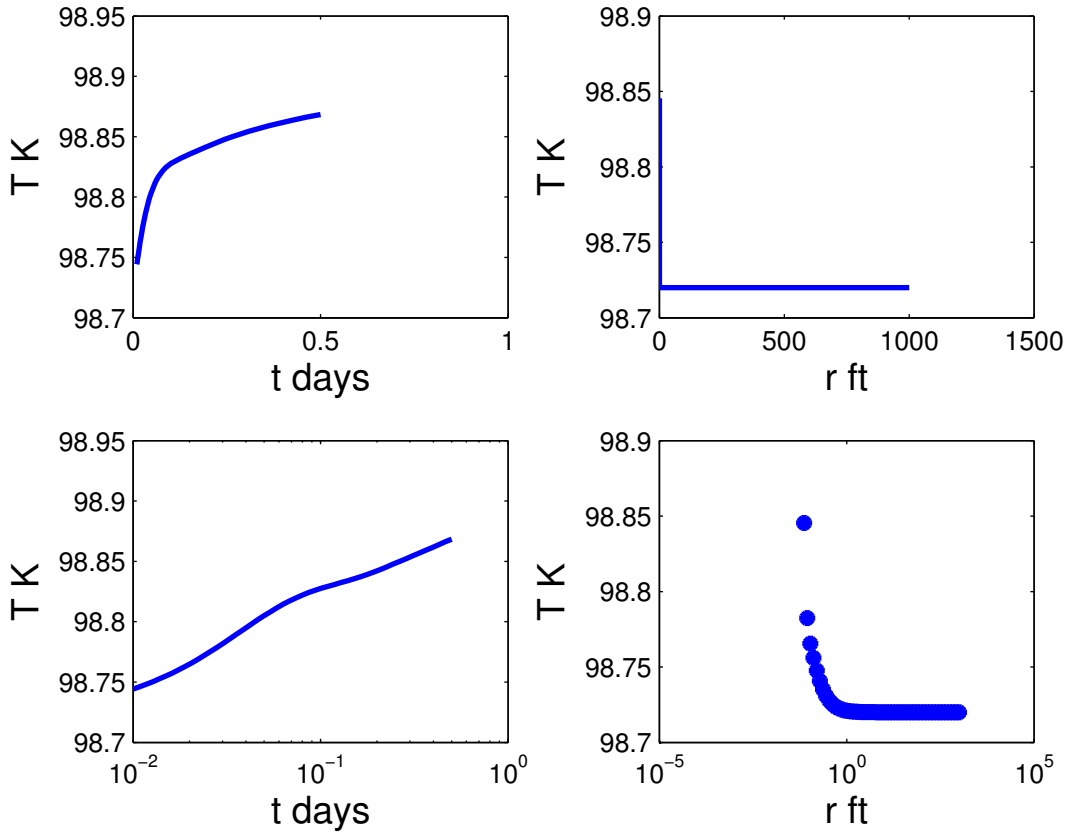

Figure 4.14: Cartesian plot (two plots at the top) and semilog plot (two plots at the bottom) of temperature in spatial and temporal dimensions during radial flow, single-phase oil flow

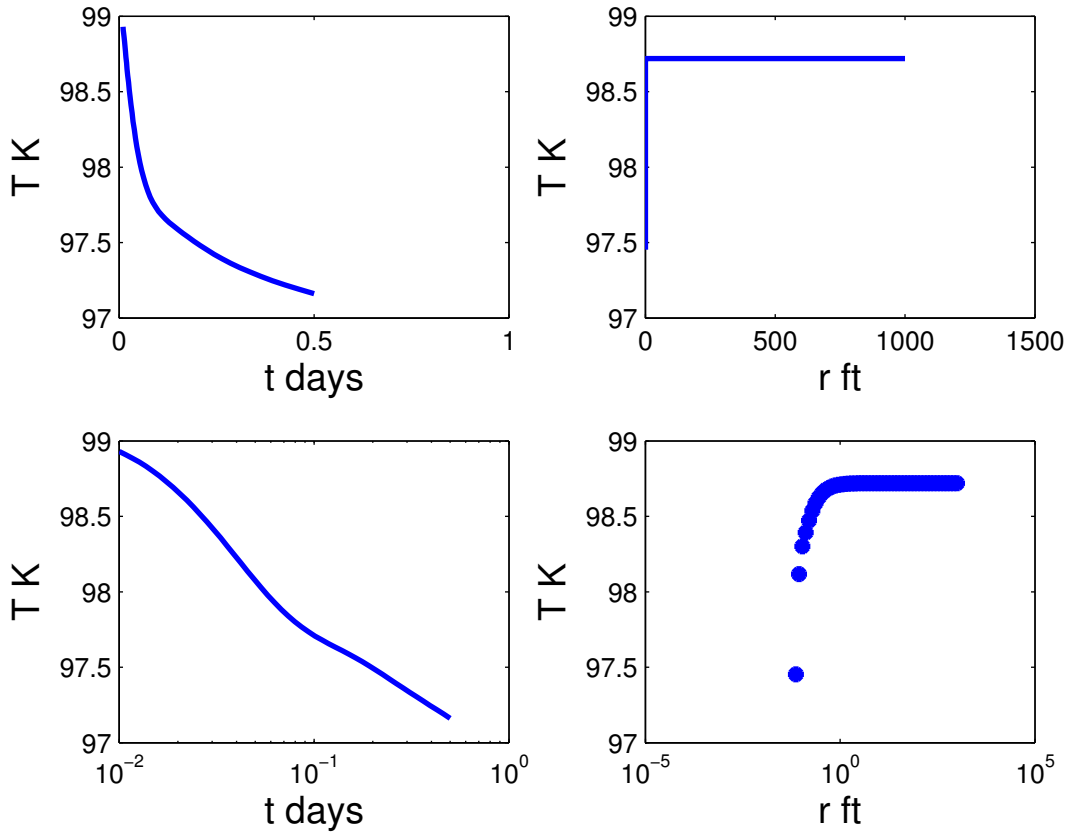

Figure 4.15: Temperature distribution in the spatial and temporal dimensions of single-phase gas flow.

fluid is cooled down after the flow stops (Figure 4.18). Other than the fact that heating sources cease, there are two other reasons for this cooling down: 1. heat is lost to the formation through conduction; 2. increase of pressure during the buildup period has a cooling effect due to Joule-Thomson effect. The magnitudes of temperature increase during the flowing period, and decrease during the shut-in period are a function of flowrate, fluid and formation properties. Therefore, both the distributed temperature and transient temperature are important for understanding production status and formation properties.

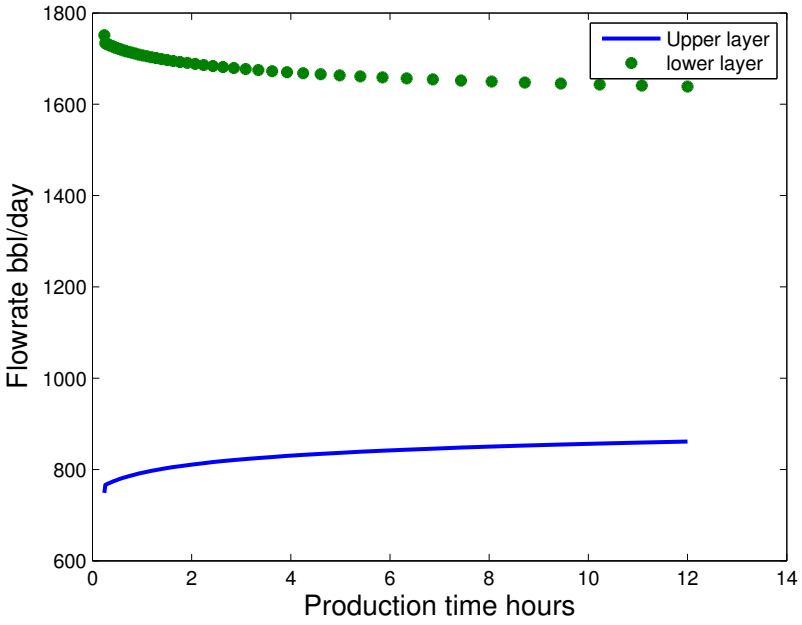

Figure 4.16: Flowrate history of each layer.

4.2.3 Verification

Our model was verified by comparing with two published cases. The first case (Case 1-B.1) we simulated is based on a production scenario made up by Alves et al. (1992), in which gas-condensate is flowing in a vertical well. The relevant data of the fluid

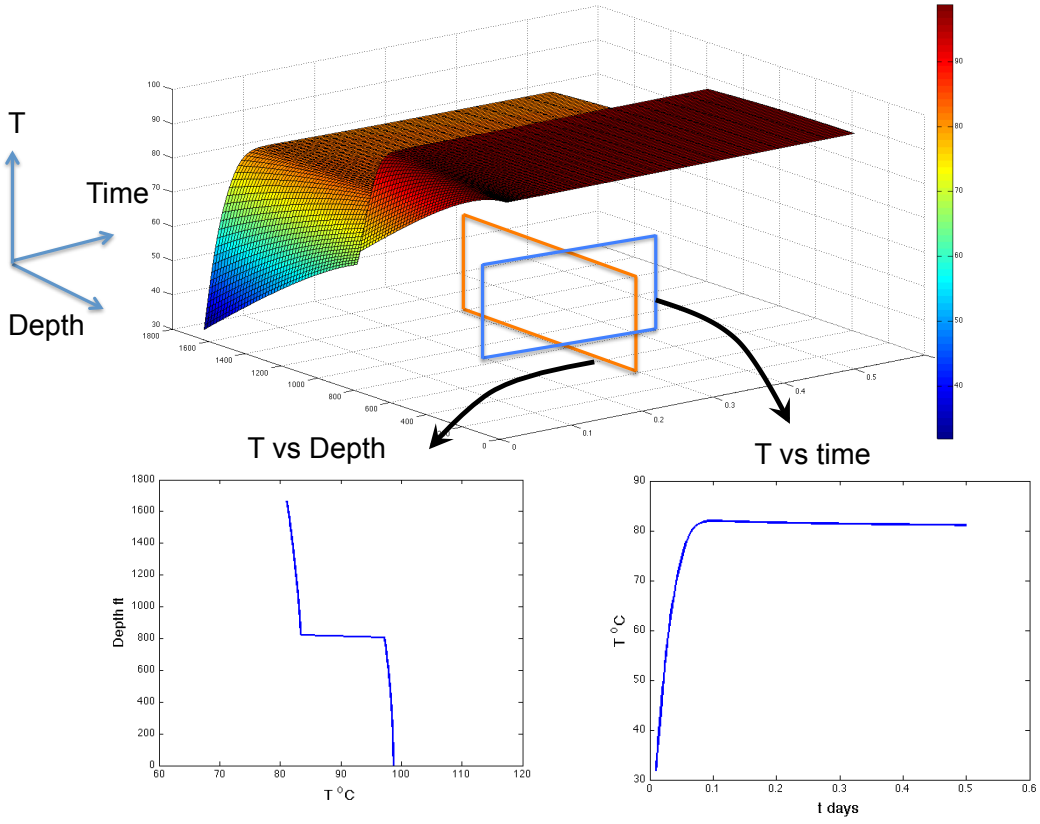

Figure 4.17: Different views of wellbore temperature data (DTS data).

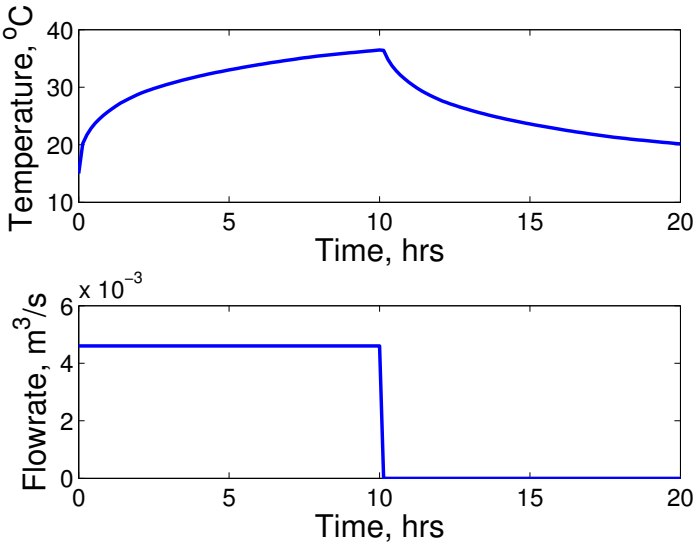

Figure 4.18: Temperature decreases during a shut-in period.

composition and operation condition can be found in Alves et al. (1992). In our model, in the reservoir direction r, the total radius of reservoir was set to be 300 ft, and discretized into ten logarithmic grids; for the wellbore direction z, we used 20 uniform grids. Time step was set to be 0.02 days, and the simulated production time is 30 days. Steady state was achieved. The phase diagram and simulated wellbore pressure and temperature at the steady state are shown in Figure 4.19, from which we can see that there is phase change occurring during flow within the wellbore. Figure 4.20 shows three simulation results: rigorous enthalpy-balance results from Alves et al. (1992), our compositional model results and Ramey's (1961) analytical solution. Our model has a good match to the Alves et al. results, which verifies our numerical model. Another observation is that the Ramey solution does not give a correct temperature prediction in this case. The difference between the Ramey model and our numerical model is the treatment of the frictional heating effect and phase change: these two terms are neglected in Ramey's model while they are modeled rigorously through energy balance equation and drift-flux model in our approach. In this

case, phase change is encountered and the well production rate is high, both leading Ramey's model to an inaccurate temperature prediction. This comparison emphasizes the importance of building a compositional model for complicated production scenarios. In addition, this shows the effect of the presence of gas on the temperature distribution, which is instructive for the estimation of phase flowrate or gas-oil ratio from DTS data.

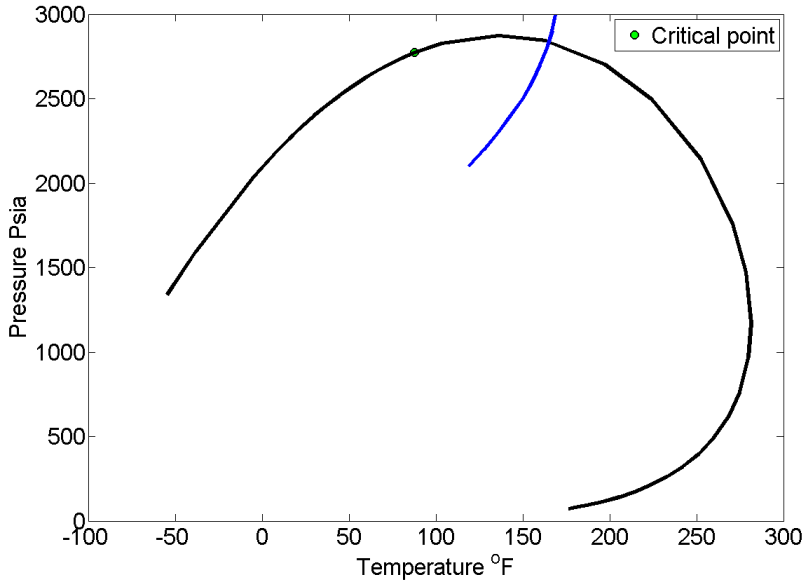

Figure 4.19: Phase diagram (black line) and simulated wellbore pressure temperature (blue line) of gas-condensate case (Case 1-B.1).

The second case (Case 1-B.2) is a well producing volatile oil, following Pourafshary et al. (2008). Composition is shown in Table 4.4. The phase diagram and simulated wellbore pressure and temperature from Pourafshary's model and our model are shown in Figure 4.21. Our model matches Pourafshary's compositional model. Again, this verifies our model. However, we observe a significant difference between the pressure prediction from the black-oil model and that of the compositional model, as shown in Figure 4.22. As we mentioned earlier, the only difference of these two

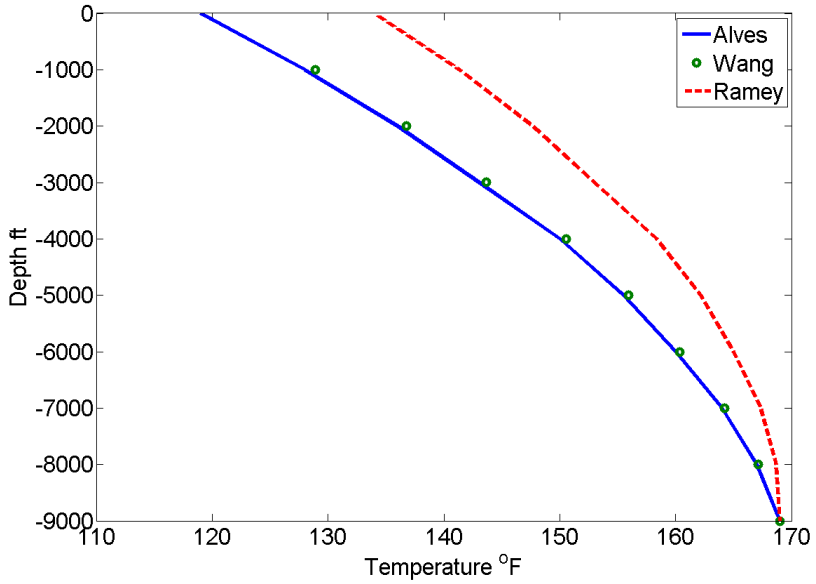

Figure 4.20: Temperature prediction of gas-condensate case (Case 1-B.1).

models is the approach to calculate fluid phase properties. The pressure difference (Eq. 4.16) consists mainly of the hydraulic pressure change, which depends on fluid mixture density, therefore, the different approaches which give different density outputs have different pressure predictions. However, temperature distribution does not have such a close relationship with the fluid PVT properties, and there is no clear discrepancy between the temperature predictions from these two models.

Table 4.4: Composition for the case of a volatile-crude oil, Case 1-B.2.

Component	Mole Fraction
C1	0.55
C3	0.1
C4	0.1
C5	0.1
C7	0.075
C8	0.075

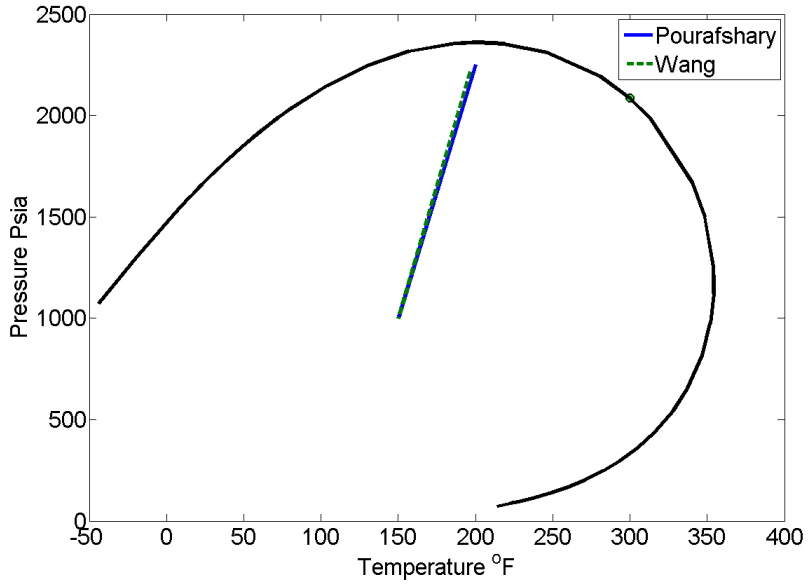

Figure 4.21: Phase diagram and simulated wellbore pressure temperature of volatile oil case (Case 1-B.2).

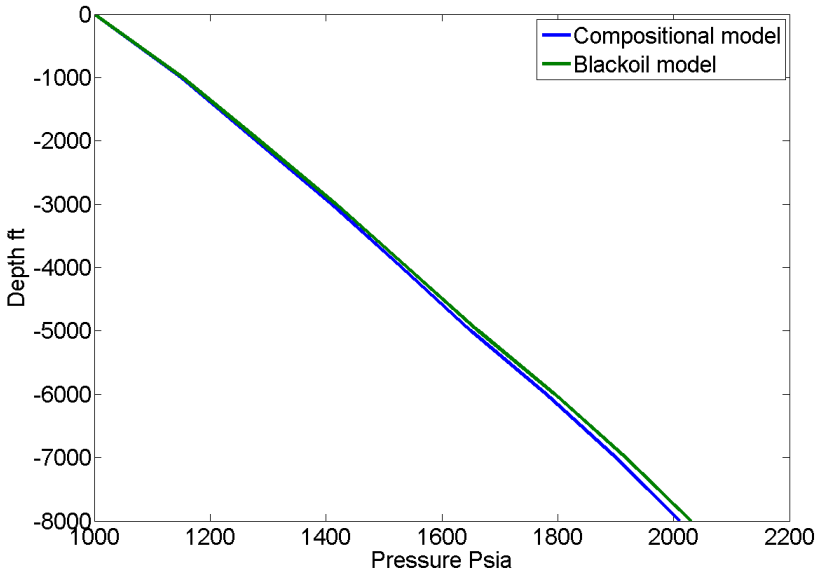

Figure 4.22: Pressure prediction from black-oil and compositional model.

4.3 Sensitivity Test

There are several parameters affecting the model output. A sensitivity test is useful to give us a sense of how important each factor is. The parameters that we tested are: thermal expansion coefficient of the fluid, rock thermal conductivity, porosity of rock, permeability and flowrate. The sensitivity test was based on a case of a single producing layer (Case 1-C), the parameters of the Case 1-C are shown in Table 4.5.

Table 4.5: Parameter for Case 1-C.

	Rock	Fluid
Permeability [md]	20	
ϕ	0.5	
β [1/K]		0.0001206
Surface flowrate [bbl/day]		2500

A comparison of the sensitivity tests is shown in Figure 4.23 to 4.27. There are two types of figures: (1) transient entry temperature T_e (temperature in sand face), (2) temperature distribution in the wellbore after producing for 7 days.

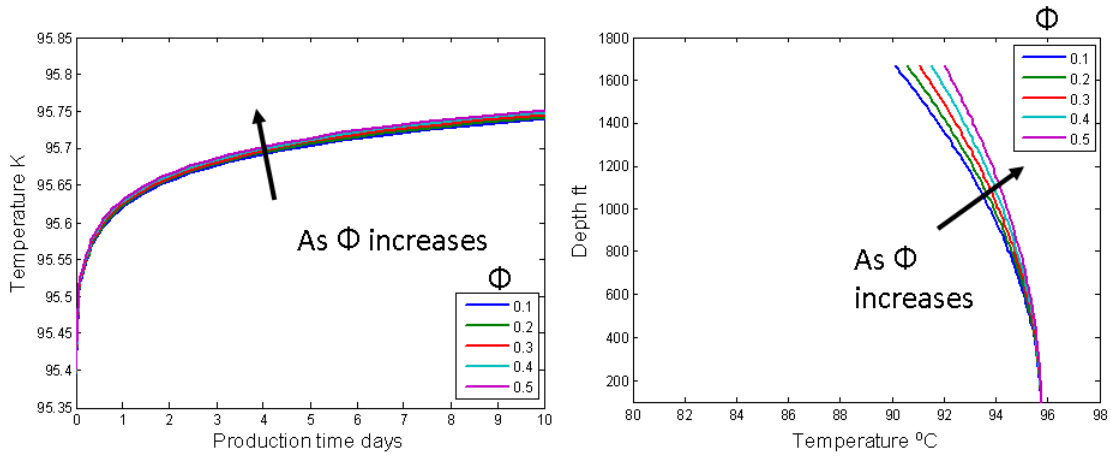

Figure 4.23: Sensitivity to porosity ϕ.

From the sensitivity test, the first important finding was that the temperature responses (both distributed temperature and transient temperature) are sensitive to

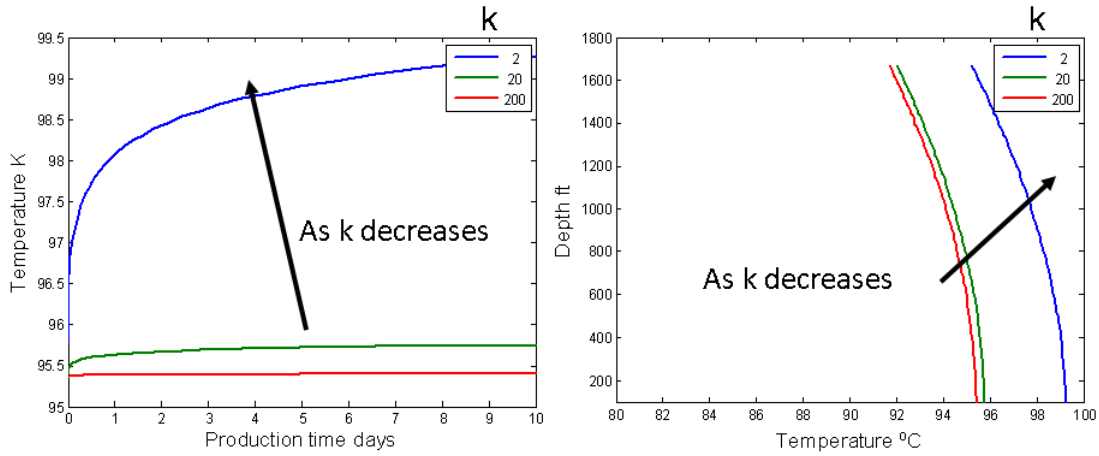

Figure 4.24: Sensitivity to permeability k.

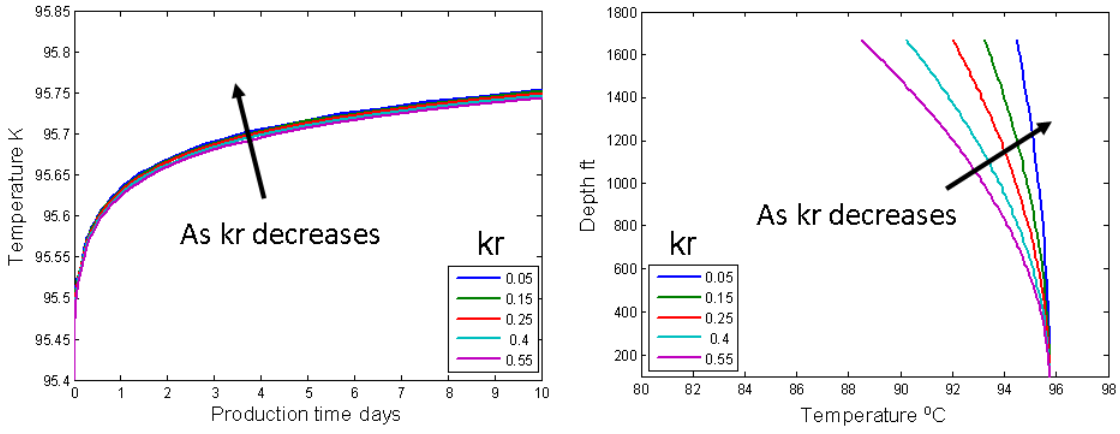

Figure 4.25: Sensitivity to rock thermal conductivity k_r.

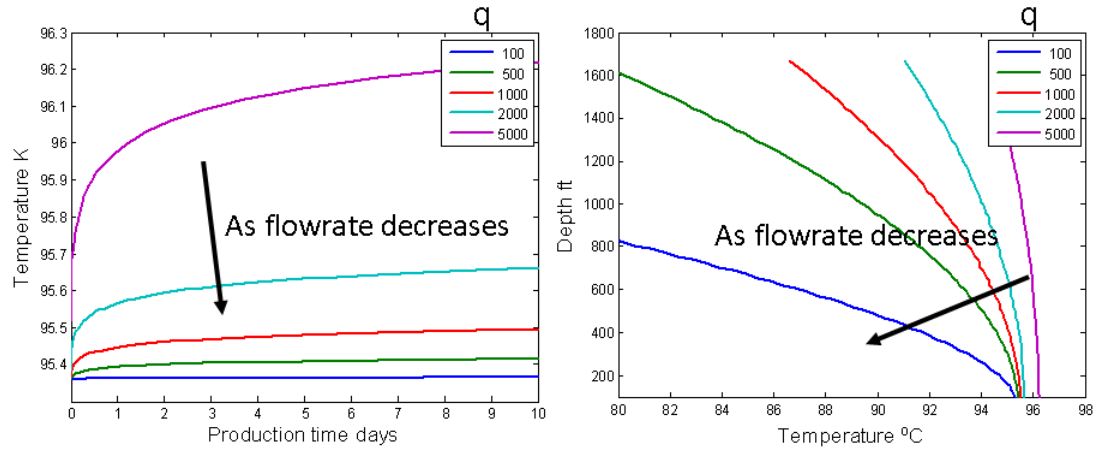

Figure 4.26: Sensitivity to flowrate q.

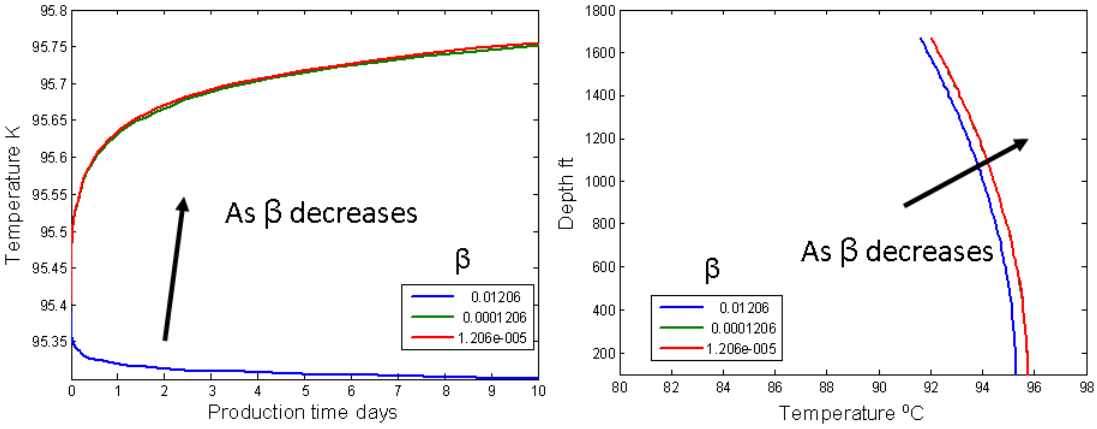

Figure 4.27: Sensitivity to thermal expansion coefficient β.

permeability and flowrate. As shown in Figures 4.24 and 4.26, there is a temperature difference of almost 4 ^oC corresponding to a ten-time difference of permeability, and 0.8 ^oC temperature difference as a result of five times difference of flowrate. These temperature variations can be distinguished easily in DTS data, considering the DTS data resolution is 0.1 ^{o}C. Therefore, it is promising to estimate permeability and flowrate from DTS data.

The second finding is that the temperature change follows a different trend with different thermal expansion coefficients. As shown in Figure 4.27, when the β value is large, the fluid is mostly probable in gaseous phase, and the temperature decreases at a pressure decreasing gradient according to the Joule-Thomson effect. By contrast, the temperature increases due to pressure decreasing when β is small, which indicates a liquid phase. One application of this phenomenon is to use DTS data as a method to identify the type of entering fluid. Fluid identification is useful in production monitoring, and even more valuable in horizontal well operation and interwell correlation tests.

4.4 Summary

In this chapter, the process of building a compositional wellbore/reservoir coupled thermal model has been presented. This model is capable of computing pressure and temperature distribution in the wellbore and reservoir under multiphase flow. Accuracy of this model is assured in the following three ways: 1. using drift flux model to predict multiphase flow pressure; 2. fluid PVT properties were obtained by solving Equations of State, which is more accurate than the values obtained by averaging or mixing rules; 3. using numerical methods to solve the heat transfer between wellbore and formation, avoiding the assumption of an invariant relaxation length. This model was verified by comparing with published results.

Furthermore, based on this well model, several phenomena (e.g. multiphase flow, Joule-Thomson effect) affecting the pressure and temperature distribution were studied and their influences were evaluated.

We concluded that a rigorous and complete well model is important for accurate prediction of the temperature profile under complicated flow scenarios. This work allows flowrate profiling based on DTS data. The understanding of how different phenomena influence the temperature distribution is helpful to understand downhole production scenarios.

Chapter 5

Flowrate Profiling by Temperature

The simulation results in Chapter 4 showed that temperature distribution in the wellbore is affected by flowrate profile, which makes estimating flowrate profile from Distributed Temperature Survey (DTS) data possible. In practice, downhole flowrate profiling is a time-consuming process for the traditional methods, in which spinner is run through the target interval and measures flowrate only in a point-by-point fashion. Even worse, sophisticated well geometries and complicated flow scenarios limit the applicability of running a spinner tool. By contrast, the DTS system, in which only optical fibers are installed downhole, can measure all the downhole points simultaneously, providing us real-time monitoring of the whole downhole interval. It is worthwhile to do research on inverting flowrate profile from the temperature profile, making the DTS data more useful for downhole production surveillance.

In this chapter, different inverse methods were developed to invert flowrate profile from the temperature profile. Two kinds of inverse model, i.e. Least-Square model and Linear Inverse model based on Bayes' Theory, were studied and compared. After understanding the limitation of each method, the best-performing method was applied to several cases of single-phase flow and multiphase flow, to explore the applicability of inverting flowrate from DTS data.

5.1 Problem Setup

As we mentioned in Chapter 2, several research works about estimating flowrate from temperature data have been published. For an example, Ouyang and Belanger (2006) used mixing temperature profile to estimate flowrate profile in vertical wells; Brown (2005) was able to estimate flowrate profiles by using both mixing temperature and entry temperature; Sui et al. (2008) also succeeded in estimating flowrate profiles by using mixing temperature. Depending on the DTS installation methods, the data available to us can be of three kinds: 1. entry temperature only, 2. mixing temperature only, 3. both entry and mixing temperature. (*The concept of mixing and entry temperature was sketched in Figure 1.2 in Chapter 1.*) However, in each of these published studies, only one temperature data source was discussed. The estimation result by using one kind of data source was not compared with another one. It is very common that entry and mixing temperature data are not both available. Therefore, in our research, we studied and compared the estimation results by using entry temperature OR mixing temperature.

We showed that the mixing temperature (denoted as T_m) distribution is a function of the flowrate and entry temperature (T_e) of the entering fluid from each entry point, and we also mentioned that both the T_m and T_e can be measured by DTS. As shown in Figure 5.1, in the gridding cells of the wellbore, both the T_m and T_e are data, and they are full vectors. Note that T_e is not necessarily obtained from DTS measurement, but can also be calculated by the reservoir/wellbore coupled thermal model. However, the thermal model requires the knowledge of formation permeability. We reserve the discussion of the relationship between temperature data and formation permeability to the next chapter. Hence, in this chapter, the discussion is constrained to the domain of wellbore, excluding the reservoir domain.

The unknown is then set to be the flowrate profile of the well. However, there

are two very different options. The first one is to set the unknown as the flowrate of every point in the well, resulting in a full unknown vector, as shown in Figure 5.1. For the other option, we can choose the locations of entry points, and set the flowrate of each entry point as unknown. The unknown vector is then sparse, and it only has nonzero elements at the locations of entry points. Therefore, the number of unknowns is reduced greatly to the number of the entry points, as shown in Figure 5.2.

After the knowns and unknowns are specified, the inverse model is built by two methods, with different objective function and method of solution. These two methods are the Least-Square method and Linear Inverse method, and they are discussed in the following sections.

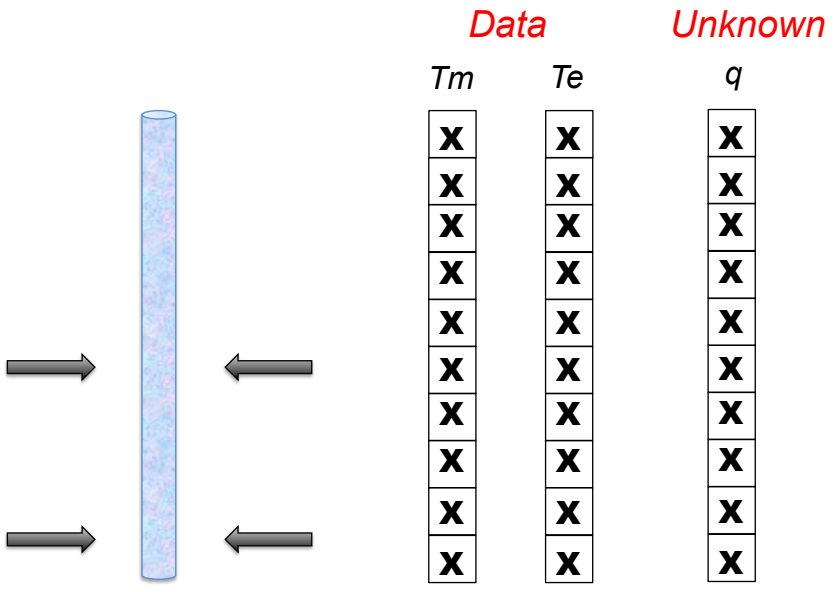

Figure 5.1: The unknowns are set to be flowrate profile q, resulting in a full unknown vector.

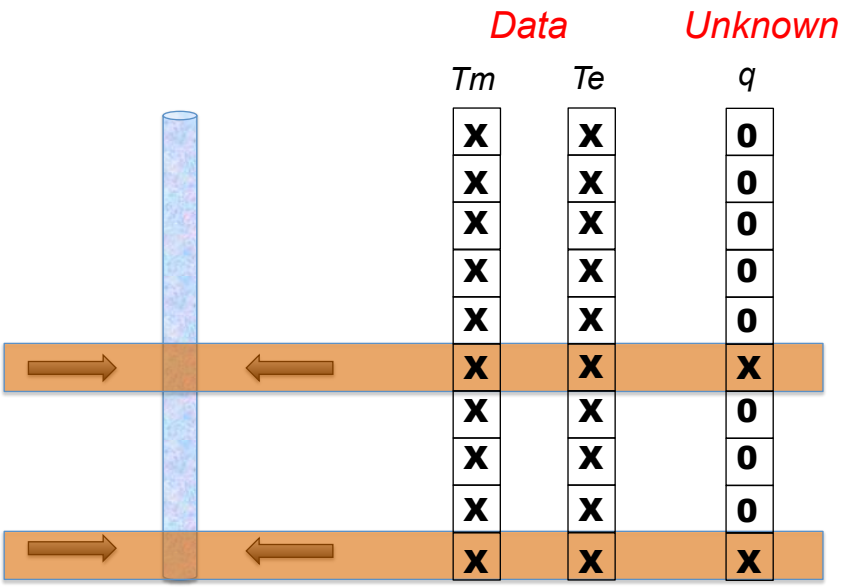

Figure 5.2: The unknowns are set to be entry flowrate q_e, resulting in a sparse vector.

5.2 Least-Square Method

5.2.1 Levenberg-Marquardt Least-Square Algorithm

A straightforward approach of setting up an inverse model is data-fitting by Least-Square method (refered as L-S method in the following). The objective is to adjust the parameters of a model function to best fit a data set. A data set consists of n points (data pairs) (x_i, y_i), $i = 1, \cdots, n$, where x_i is an independent variable, and y_i is a dependent variable whose value is obtained by observation. The model function has the form $f(x, \beta)$, where there are m adjustable parameters held in the vector β. The goal is to find the parameter values for the model which 'best' fits the data. The Least-Squares method finds its optimum when the sum of squared residuals S is a minimum.

$$S = \sum_{i=1}^{n} r_i^2 \tag{5.1}$$

A residual r is defined as the difference between the actual value of the dependent

variable and the value predicted by the model.

$$r_i = y_i - f(x_i, \beta) \tag{5.2}$$

We used a numerical minimization algorithm, Levenberg-Marquardt, to solve this problem. Like other numeric minimization algorithms, the Levenberg-Marquardt algorithm is an iterative procedure. The process starts from an initial guess for the parameter vector, β. In each iteration step, the parameter vector β, is replaced by a new estimate, $\beta + \delta$. To determine δ, the functions $f(x_i, \beta + \delta)$ are approximated by their linearization.

$$f(x_i, \beta + \delta) \approx f(x_i, \beta) + J_i\delta \tag{5.3}$$

where:

$$J_i = \frac{\partial f(x_i, \beta)}{\beta} \tag{5.4}$$

At the minimum of the sum of squares, the gradient of S with respect to δ will be zero. The first-order approximation of $f(x_i, \beta + \delta)$ gives:

$$S(\beta + \delta) \approx \sum_{i=1}^{m}(y_i - f(x_i, \beta) - J_i\delta)^2 \tag{5.5}$$

Taking the derivative with respect to δ and setting the result to zero gives:

$$J_T J\delta = J^T[y - f(\beta)] \tag{5.6}$$

where J is the Jacobian matrix whose i^{th} row equals J_i, and f and y are vectors with i^{th} component $f(x_i, \beta)$ and y_i, respectively. This is a set of linear equations which can be solved for δ.

Levenberg's contribution is to replace this equation by a "damped version":

$$(J^T J + \lambda I)\delta = J^T[y - f(\beta)] \tag{5.7}$$

where I is the identity matrix.

The (nonnegative) damping factor, λ, is adjusted at each iteration. If reduction of S is rapid, a smaller value can be used, bringing the algorithm closer to the Gauss-Newton algorithm. On the other hand, if an iteration gives insufficient reduction in the residual, λ can be increased, giving a step closer to the steepest descent direction. For large values of λ, the step will be taken approximately in the direction of the gradient.

In the next section, we report the test of the performance of L-S method using a synthetic case.

5.2.2 Different Unknown Vector Setups

The case 2-A.1 was used to test the performance of the L-S method, in which a well is producing from two layers. In the process of generating the synthetic data, the flowrate profile was specified. As mentioned earlier, the reservoir model is not involved in this problem, and for the convenience of computation, entry temperature (T_e) was assumed to be the same as geothermal temperature. By specifying the flowrate profile (only a temperature profile at a single time step was used, as shown in the left plot in Figure 5.3, which is the temperature distribution after production for 7 days) and properties of fluid, listed in Table 5.1, a synthetic set of T_m (Figure 5.3) was calculated from the well thermal model. In the inverse model, T_m, T_e and fluid PVT properties (Table 5.1) are given as inputs, in order to estimate the flowrate profile.

We first set the unknown to be the flowrate at every point in the well, as shown in Figure 5.1. The result of using L-S method is shown in Figure 5.4. This method performs poorly. Even though case 2-A.1 is a simple production well, with single-phase flow, and has only two entry points and no outflow (outflow is the flow in the direction from wellbore back to the formation), as shown in Figure 5.4, this method

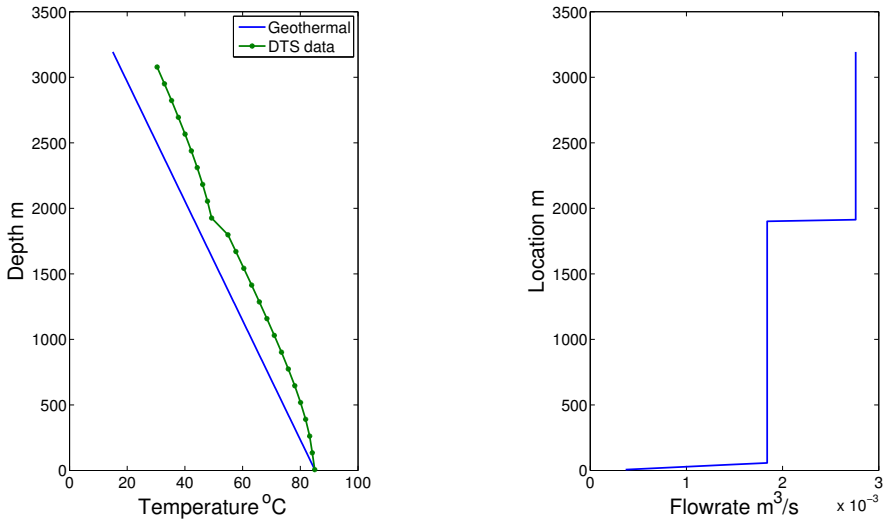

Figure 5.3: Synthetic data set of case 2-A.1.

Table 5.1: Well and fluid parameters of case 2-A.1.

Fluid density (kg/m^3)	800
Heat capacity $(J/kg/k)$	1601.8
Wellbore radius $(inch)$	1.5
Wellbore length (m)	3200
Surface flowrate (bbl/day)	1200

still cannot estimate flowrate profile correctly from the input data. Even if we started from a nonuniform initial guess, which contains the information about the locations of entry points implicitly, the estimation (as shown in Figure 5.5) is still not good.

The reason of this failure is neither that the data set is not large enough, (we also tried using synthetic data set generated on a finer grid, and did not improve the result), nor that the stopping criteria for the iteration process is too loose or too tight. As the residual after the inverse problem is very low, which is shown in Figure 5.6, the DTS data can be reproduced very well, which means that both the true flowrate (the left plot in Figure 5.3) and the estimated (but 'wrong') flowrate profile shown in Figure 5.4 can generate the same shape of temperature profile (Figure 5.3).

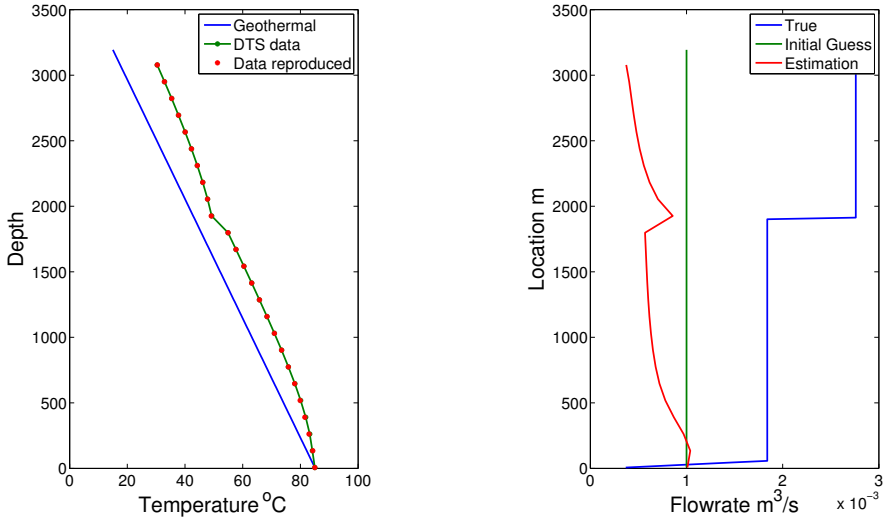

Figure 5.4: Estimation result of setting flowrate profile as unknown, starting from uniform initial guess.

To improve this model, adding more constraints into this problem was considered, e.g. assuming that the flowing profile is increasing monotonically upwards in the wellbore. However, this assumption would prevent the general application of this inverse model: because the wellbore might encounter outflow, this constraint would

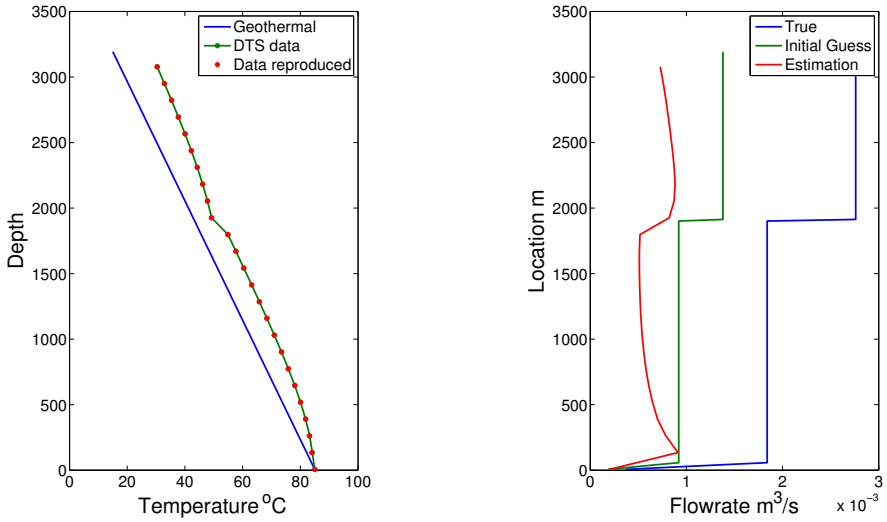

Figure 5.5: Estimation result of setting flowrate profile as unknown, starting from nonuniform initial guess.

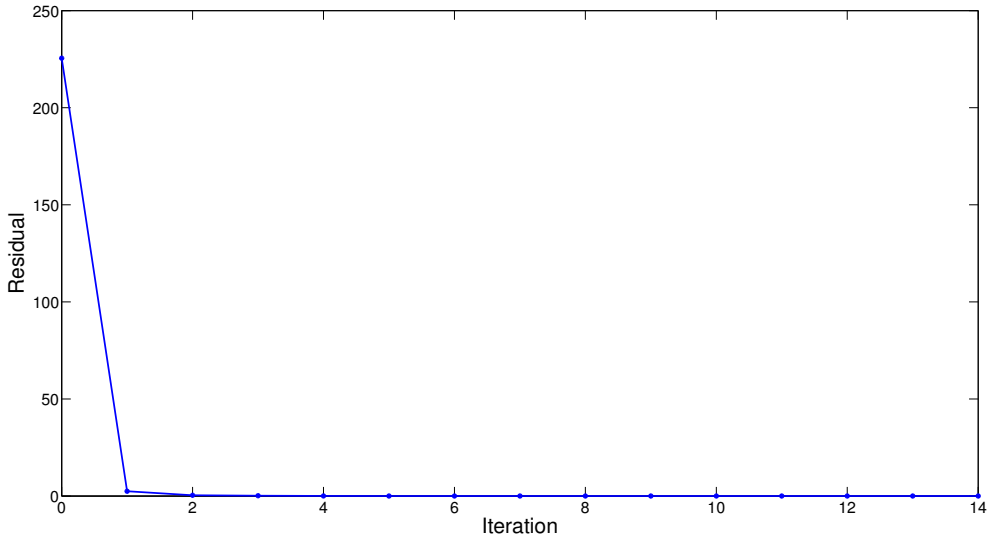

Figure 5.6: Residual value of each iteration.

lose the potential application of using DTS to detect the leaking points. Therefore, we did not add such constraints to the inverse model.

The second option for setting the unknowns to be entry flowrates (as sketched in Figure 5.2) was then studied. Compared with the full vector in the first approach, in this method, the number of unknowns is reduced to two. As shown in Figure 5.7, the flowrate can be estimated accurately. However, the success of this method depends on the accuracy of input of the entry point locations. As an example shown in Figure 5.8, if the location of upper layer is misplaced by 100 m, the estimation will be misleading. Therefore, we learned that the accurate information about entry point location is crucial for the success of the L-S method. As the temperature profiles of mixing temperature and entry temperature can be measured by DTS, we studied how to locate entry points from the DTS data. The results of our study are shown in the next section.

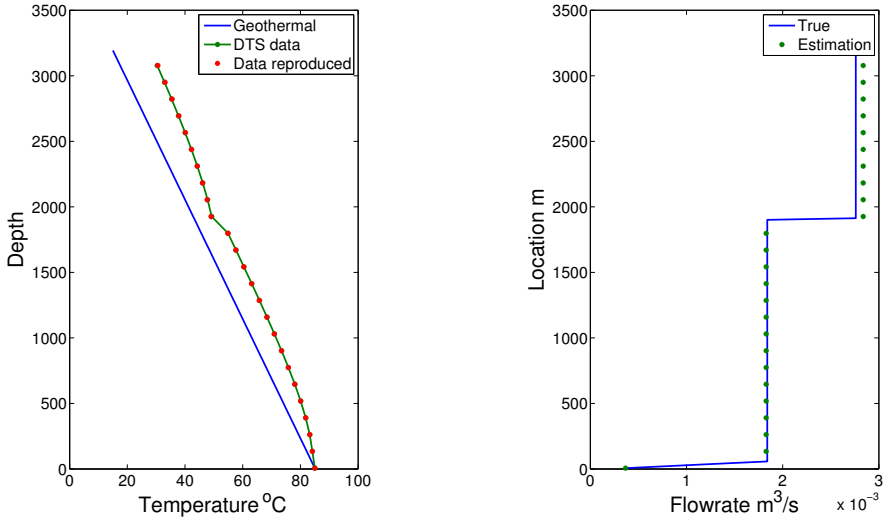

Figure 5.7: Estimation result when entry flowrates are set as unknown.

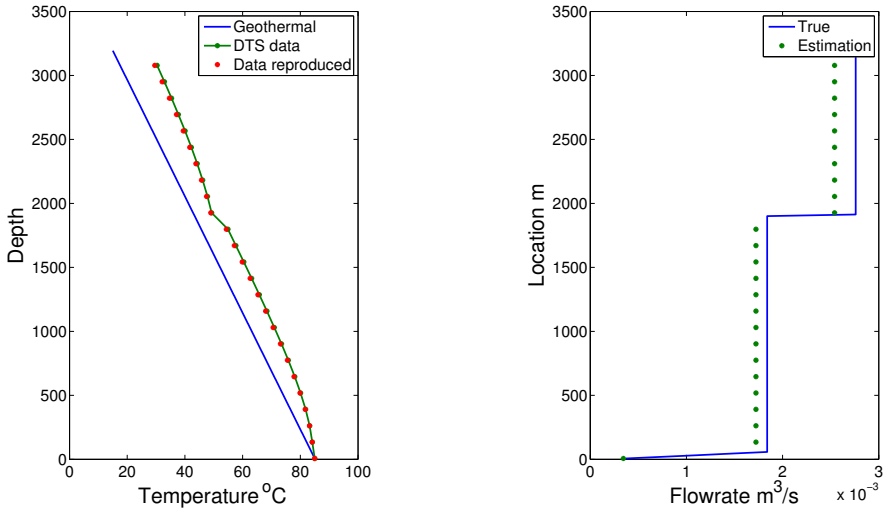

Figure 5.8: Estimation result when wrong entry points locations are input.

5.2.3 Locate Entry Points Using DTS Data

Both the entry temperature and mixing temperature are sensitive to flowrate, and thus it is possible to locate each entry point from either mixing temperature profile or entry temperature profile.

- Entry points located by T_m

By examining the mixing temperature profile (Figure 5.3), there are small changes on the mixing temperature profile at the locations of each individual entry point. The derivative of temperature over the depth dT/dz shows spikes at the location of entry points, as seen in Figure 5.9. However, this method of finding entry points cannot be used on noisy data sets. For example, if the DTS data set is augmented with noise with normal distribution, as shown in Figure 5.10, when the Singal-Noise Ratio of the noise is 15 dB noise (Signal-Noise Ratio is defined as the amplitude of signal to noise, as in Eq. 5.8), the entry points cannot be identified on the derivative curve.

$$SNR = 10log_{10}(\frac{A_{signal}}{A_{noise}})^2 \tag{5.8}$$

A suitable denoising technique for this problem should be able to remove local variation while keep the general trend. As wavelet theory has the advantage of resolution-by-resolution analysis of data set, it is suitable for locating entry points on noisy temperature data. We denoised the data by different wavelet levels (Symlets 4 wavelet was used), i.e. level 3, 5, and 8. The derivatives of these denoised data at different level are shown in Figure 5.11, 5.12 and 5.13. At level 5, the derivative of the denoised data has a clear spike at the location of entry point, however, level 3 or level 8 does not give good result, they give results either still too noisy or too smoothed.

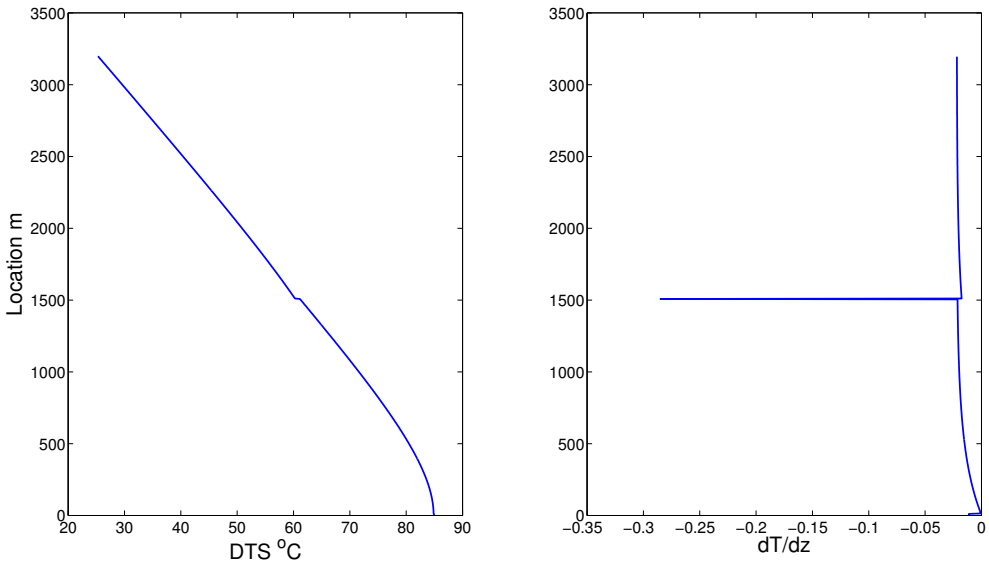

Figure 5.9: dT/dz of a mixing temperature profile.

- Entry points located by T_e

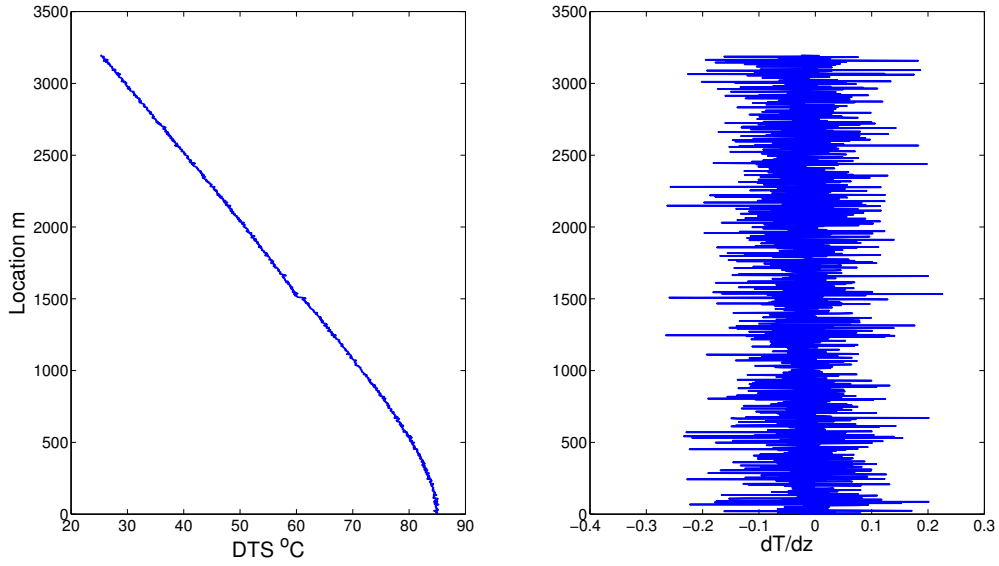

Figure 5.10: dT/dz of a noisy data set.

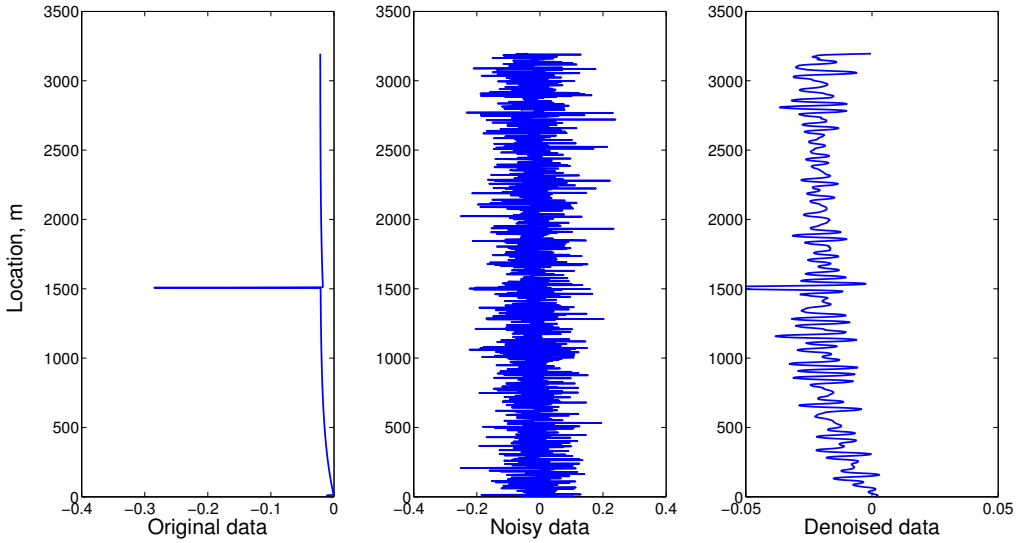

Figure 5.11: dT/dz of the denoised data by wavelet level 3.

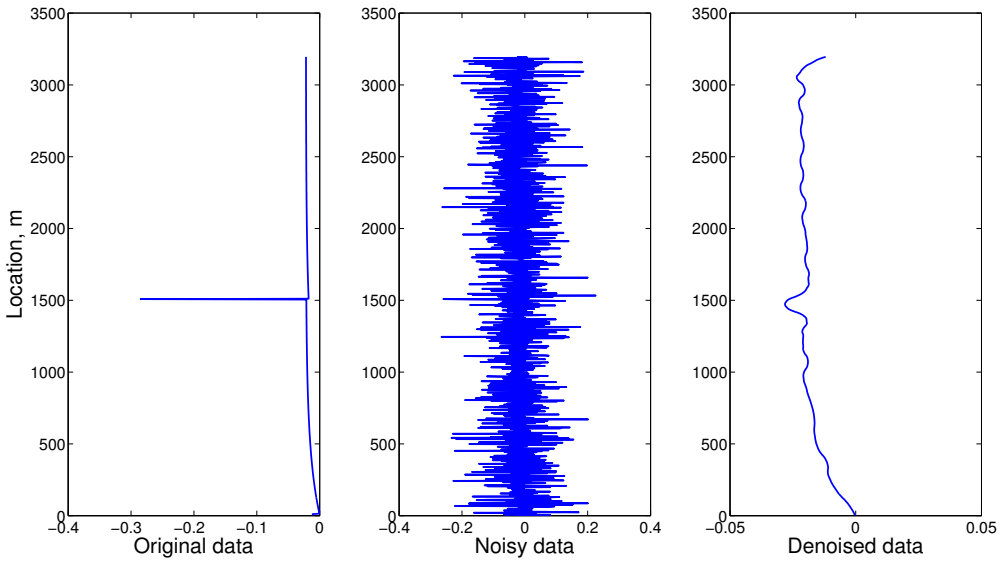

Figure 5.12: dT/dz of the denoised data by wavelet level 5.

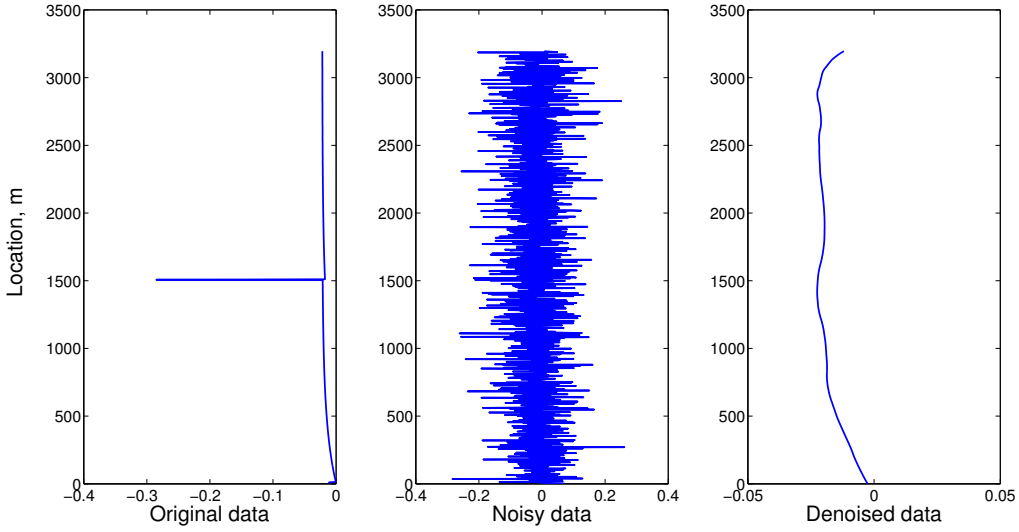

Figure 5.13: dT/dz of the denoised data by wavelet level 8.

On the profile of entry temperature (denoted as T_e), because the entry temperature is different from the original geothermal temperature, the T_e profile also shows signature at the depths of the entry points (Figure 5.14). There are humps/dips on the T_e profile corresponding to the fluid flow. However, this is not always true. The variation magnitude depends on the fluid properties and rock permeability and thermal conductivity. For example, when the formation has the properties shown in Table 5.2, the entry temperature is almost the same as geothermal temperature (Figure 5.15). Therefore, entry points cannot be identified by the T_e profiles in this case.

Table 5.2: Formation properties for Figure 5.15.

Rock density (kg/m^3)	2000
Heat capacity ($J/kg/k$)	400
Porosity radius	0.3
Thermal conductivity ($W/m/K$)	2
Permeability (md)	50

Another risk of using T_e profile to locate entry points is from the leakage of the fluid in the cement (as sketched in Figure 5.16). As shown in Figure 5.17, when the fluid is leaking in the cement, the T_e profile will not give accurate estimate of locations of entry points.

5.3 Linear Inverse Model

As introduced in Chapter 3, the linear inverse model based on Bayes' theory includes both data and prior information into the objective function, and the estimation can be regulated by structure parameters (Q_1 and Q_2), to obtain results that are a reasonable balance between curve smoothness and noise suppression. (The process of choosing Q_1 and Q_2 is explained in Appendix A.)

We used the case 2-A.1 to test this method, and the unknown was set to be flowrate at each point in the well, which is a full vector, as shown in Figure 5.1. Fluid

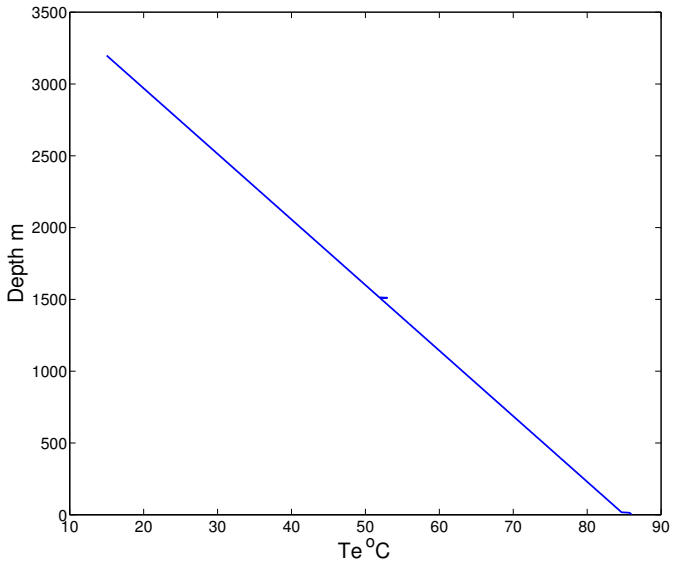

Figure 5.14: T_e profile.

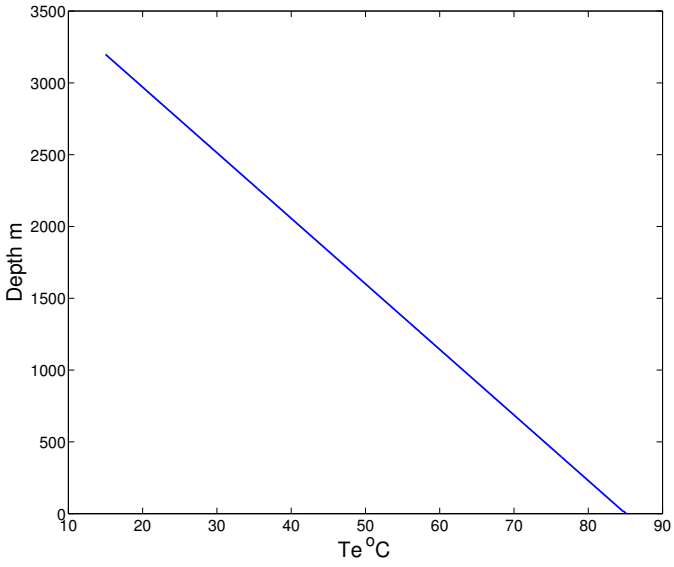

Figure 5.15: T_e profile when entry temperature is close to geothermal temperature.

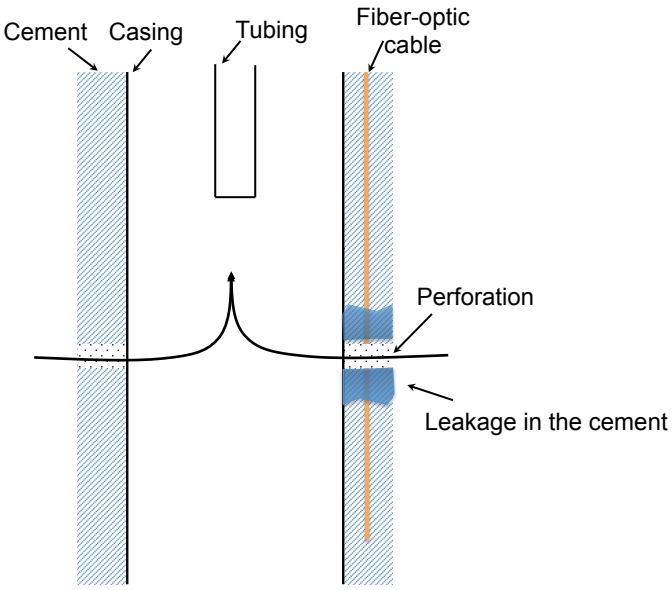

Figure 5.16: Fluid is leaking in the cement.

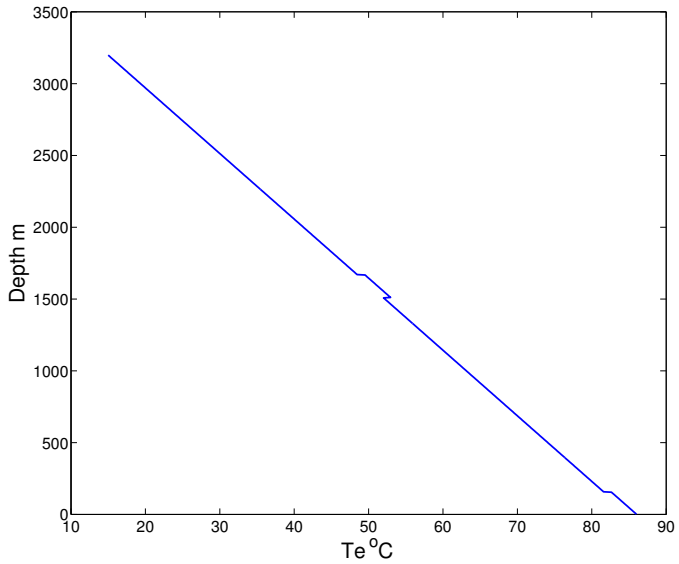

Figure 5.17: T_e profile when leakage occurs in cement.

parameters are shown in Table 5.1. The final result - the best estimate is shown in Figure 5.18. The estimation is close to the true values, and can reproduce the DTS data very well.

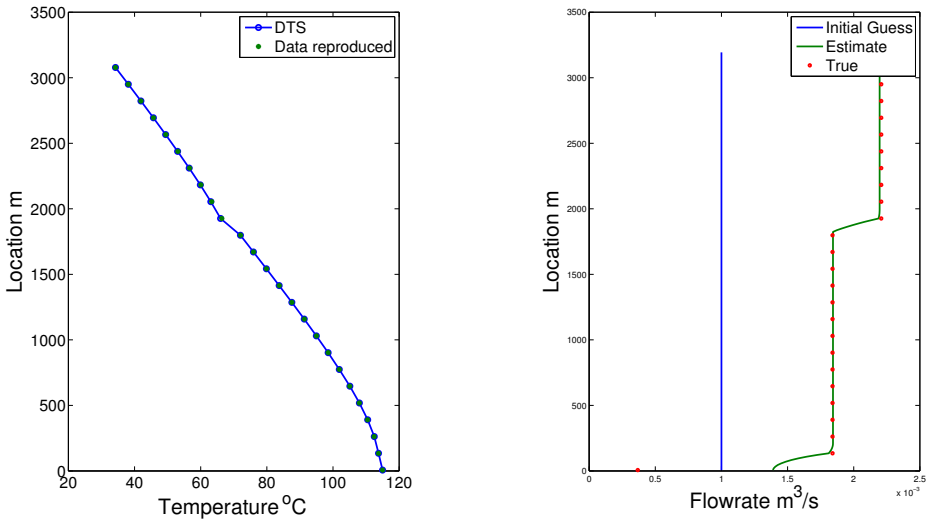

Figure 5.18: Estimation result of linear inverse model for case 2-A.1.

We then used this model to study the influence of data qualities on flowrate estimation: noise and data resolution.

- Effect of data noise

This method can tolerate a certain degree of noise. We added noise with normal distribution to the synthetic temperature data. As shown in Figure 5.19, when the noise has the Signal-Noise Ratio (SNR is defined in Eq. 5.8) at 10 dB, the estimation is still within an acceptable range. But when the SNR of the noise is 1 dB, as shown in Figure 5.20, this methods fails.

- Effect of data spatial resolution

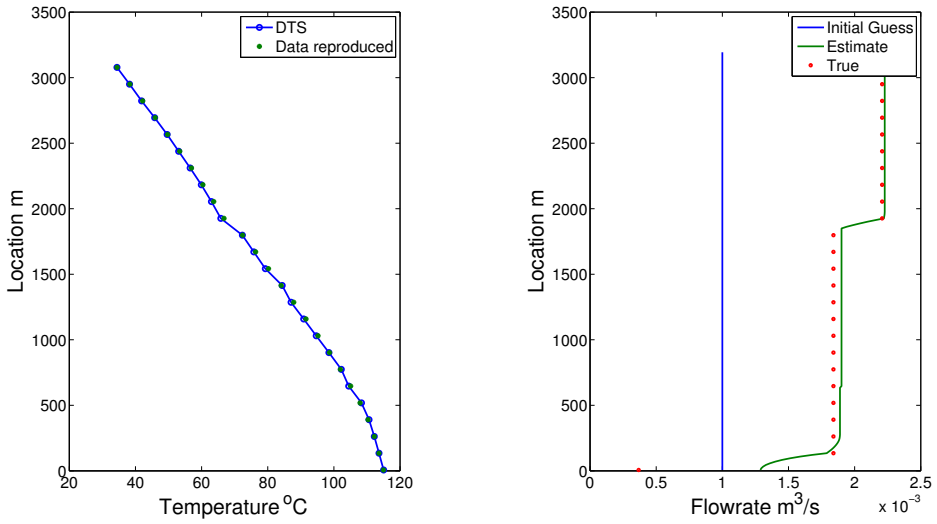

Figure 5.19: Estimation result of 10 dB Signal-Noise Ratio noisy data.

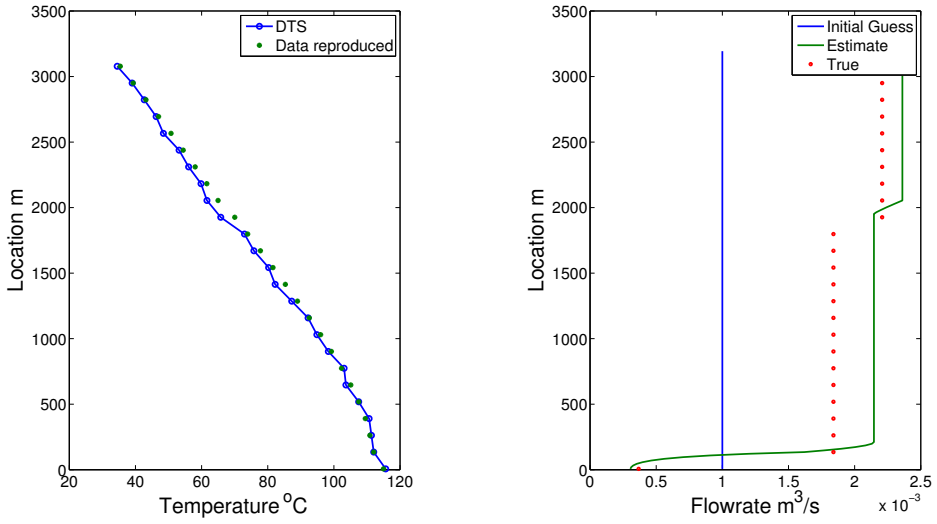

Figure 5.20: Estimation result of 1 dB Signal-Noise Ratio noisy data.

Usually, sparsity in the data set deteriorates parameter estimation. In the previous test (result as shown in Figure 5.18), the simulation grid m has 250 cells, while the data number n is 25. When the data number is smaller, for example, n is set to be 10, the estimation result is worse (Figure 5.21). The Mean Square Error of the estimation of flowrate in Table 5.3 becomes larger as the number of data is less. In other words, data with high spatial-dimension resolution is helpful for estimation.

However, there is also an issue when the data number increases. By comparing the case $m = 250$, $n = 25$ and $m = 250$, $n = 50$ in Table 5.3, we find that larger n leads to worse estimations. The reason comes from the coarse simulation grid. If we increase simulation grid point number (m) according the data point number, the estimation can be improved. As shown in Table 5.3, for the case that $n = 50$, the error of $m = 500$ is smaller than the case $m = 250$.

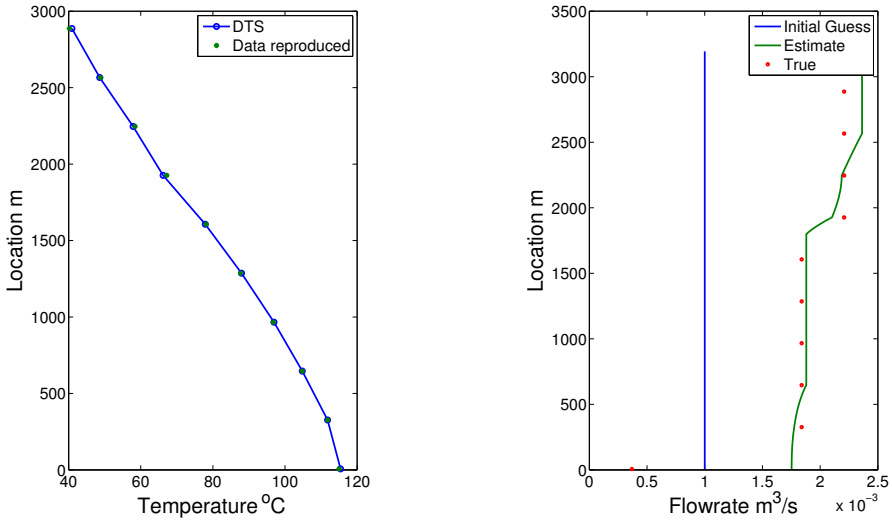

Figure 5.21: Estimation result when $n = 10$.

Table 5.3: Error of different m and n

Simulation grid number m	Data point number n	m/n	Error
250	5	50	52
250	10	25	11.5
250	25	10	6.7
250	50	5	7.5
500	50	10	6.7
1000	50	20	6.6

5.4 Estimate Flowrate in Single-Phase Flow

The Linear Inverse model was used to study more cases of single-phase flow, to explore the applicability of using this method to estimate flowrate from temperature data. The following single-phase cases were generated by modifying case 2-A.1, and the fluid properties are the same as Table 5.1.

1. Large number of entry points

   If the well has multiple entry points, for example if there are five entry points, as shown in Figure 5.22, the estimation is acceptable.

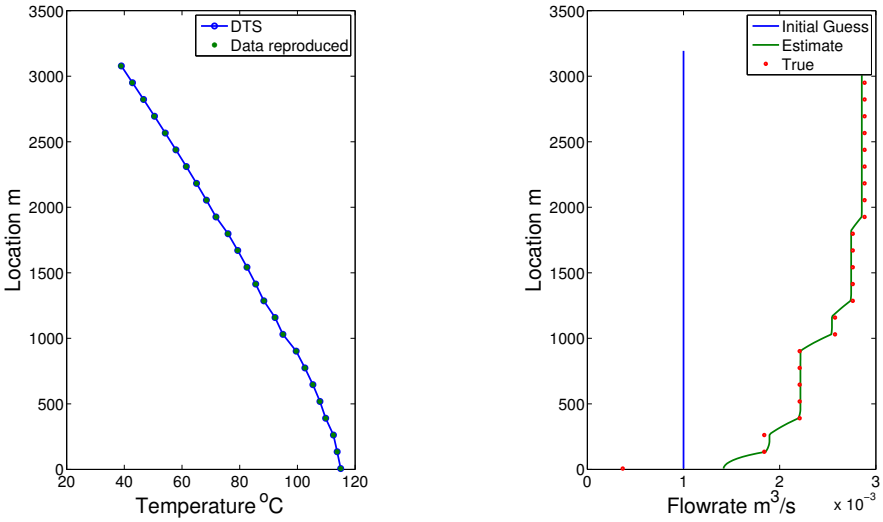

Figure 5.22: Large number of entry points.

2. Small flowrate

   If the upper layer has a very small entry flow rate (200 bbl/day) compared with the lower layer (1500 bbl/day), and there is not a clear signature on the temperature profile at the depth of entry point, as shown in Figure 5.23. However, the estimation still identifies two entry points and matches the true data.

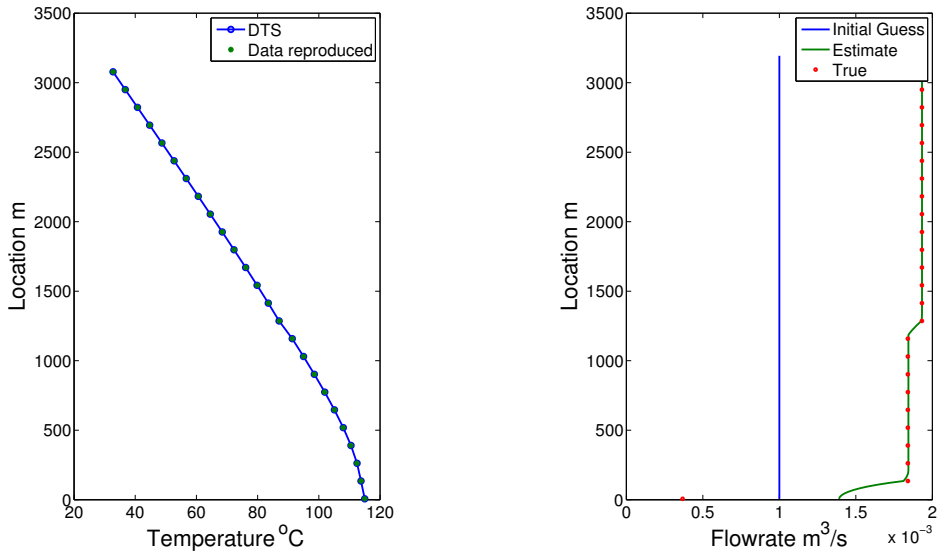

Figure 5.23: Small flowrate.

3. Close-by entry points

   As shown in Figure 5.24, the well has two pairs of close-by entry points. The layers are 100 meters apart in these two pairs. The inverse model can find all four entry points, and gives the right estimation.

4. Outflow

   In the upper layer, the entry flowrate is set to be negative to have outflow at this depth, as shown in Figure 5.25. Because the model was not imposed by monotonic curve constraint, it can give the right estimation. This method can help DTS data to identify a leaking point in the well.

5. Deviated well

   When the well is deviated for 45^o, as shown in Figure 5.26 , the estimation is also acceptable.

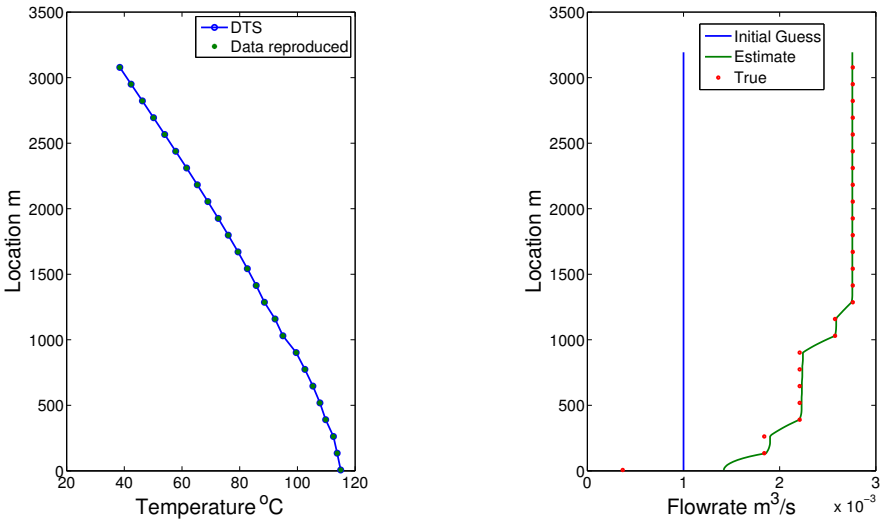

Figure 5.24: Close-by entry points.

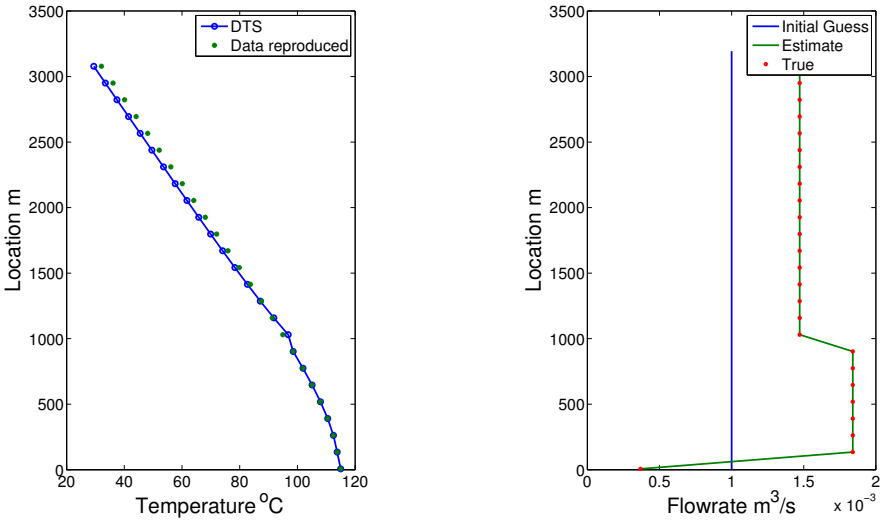

Figure 5.25: Outflow.

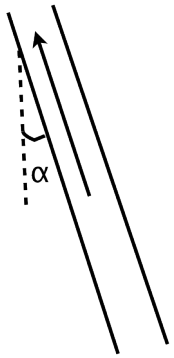

Figure 5.26: A sketch of deviation angle.

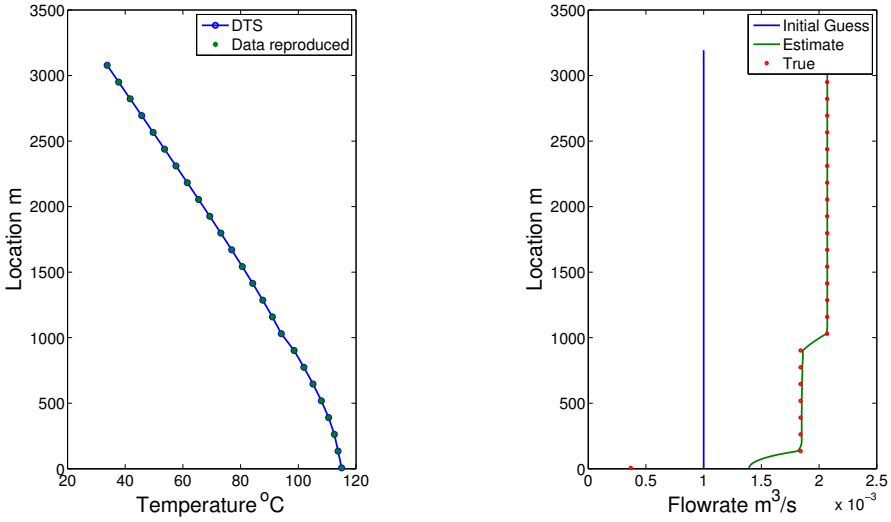

Figure 5.27: Deviated well.

6. Changing flowrate

   For this case, we used a single DTS profile to estimate a single flowrate profile. In the case that flowrate is changed during production, if the set of transient DTS data is available, this model can reconstruct the flowrate profile as a function of time, as shown in Figure 5.28. This real-time interpretation of DTS data is helpful for achieving real-time downhole production surveillance.

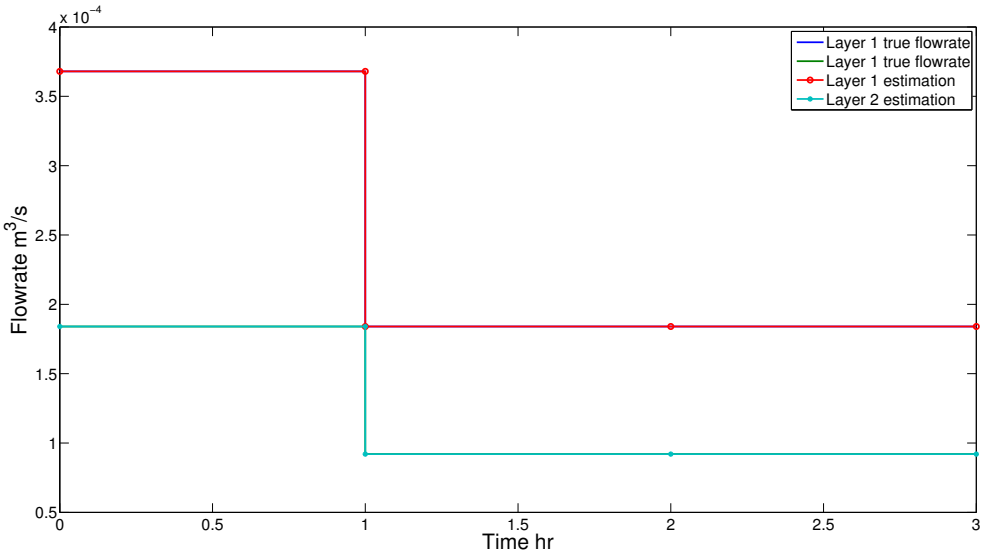

Figure 5.28: Changing flowrate.

5.5 Estimate Flowrate in Multiphase Flow

5.5.1 Problem Setup

A set of synthetic data was generated by our numerical model. In this synthetic case (named as case 2-B.1), a vertical well produces hydrocarbon both in liquid and gas phases from two entry intervals. The composition is listed in Table 5.4, and the pressure-temperature diagram is shown in Figure 5.29. In the forward simulation, the total phase flowrates were specified, and the calculated phase flowrate profiles are shown in Figure 5.30. The pressure, temperature and holdup distribution in the wellbore were obtained by forward simulation, as shown in Figure 5.31, 5.32 and 5.33.

Table 5.4: Composition for case 2-B.1.

Components	Mol Fracton (%)
C_1	24
C_4	16
C_6	20
C_8	40

In the inverse model, we assumed that the locations of all the entry intervals were known, and the unknowns are set to be the entry flowrate of each phase. Therefore, there are four unknowns: oil and gas flowrates from each of two entry points. Least-Square method was used to solve this inverse model. The available data are the profiles of mixing temperature (T_m) and entry temperature (T_e), pressure profile and wellhead flowrate of each phase. We note that it may be difficult to measure pressure profile in practice, as the Distributed Pressure Sensor is technically immature and not yet widely applied. It is best for the inverse model to minimize the usage of pressure profile information, and thus we conducted the following tests, in an order of increasing information usage.

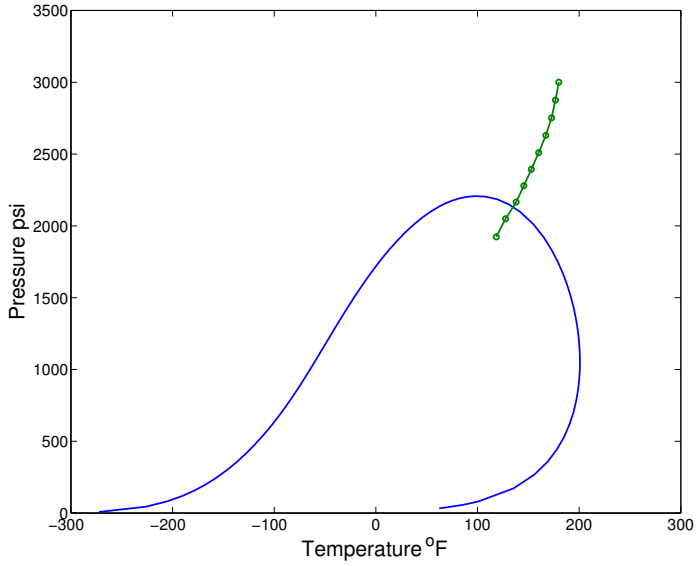

Figure 5.29: Pressure-Temperature diagram of case 2-B.1.

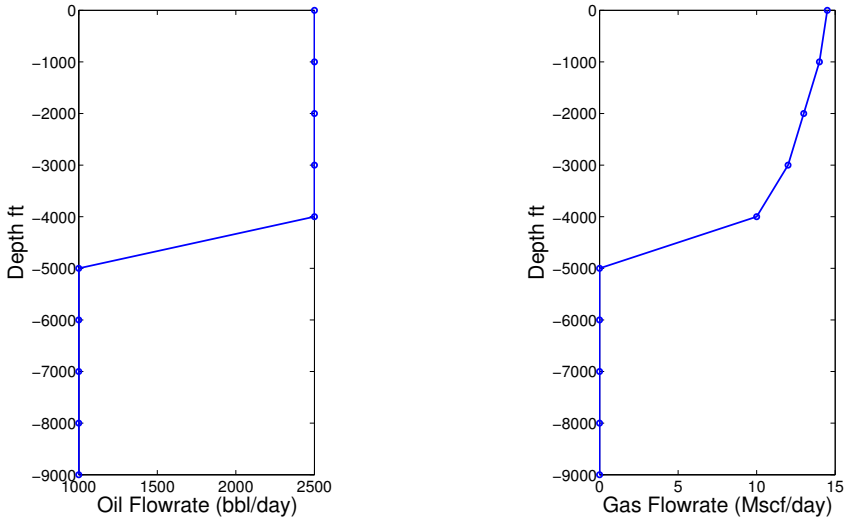

Figure 5.30: Phase flowrate profile of case 2-B.1.

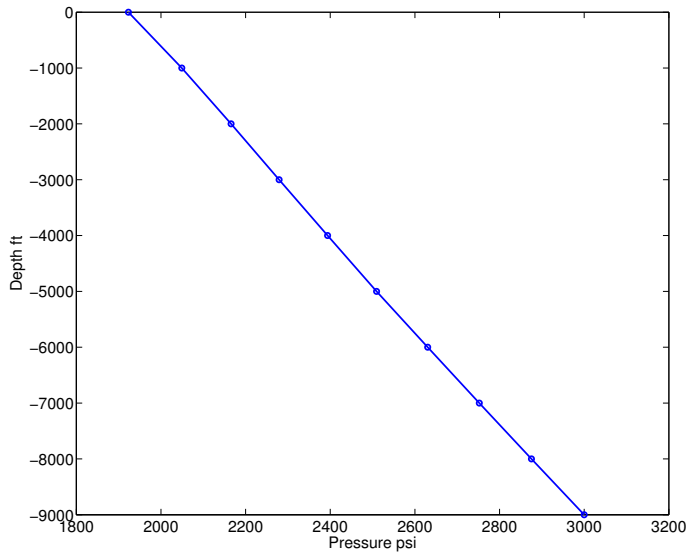

Figure 5.31: Pressure profile of case 2-B.1.

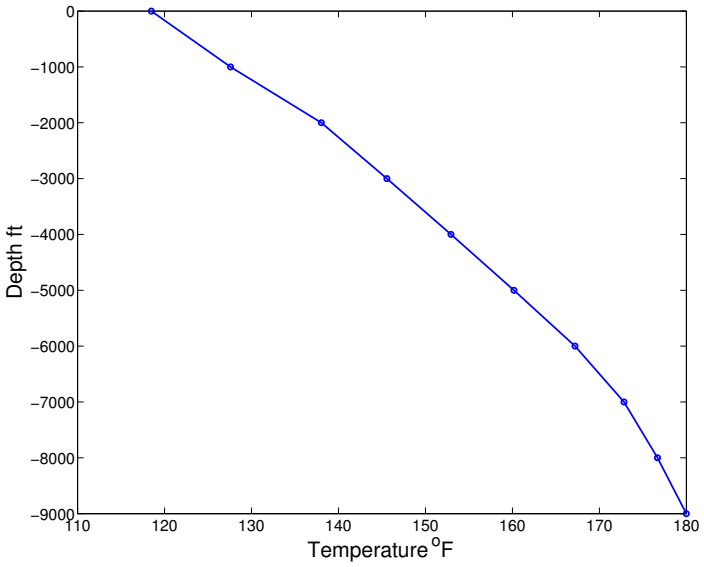

Figure 5.32: Temperature profile of case 2-B.1.

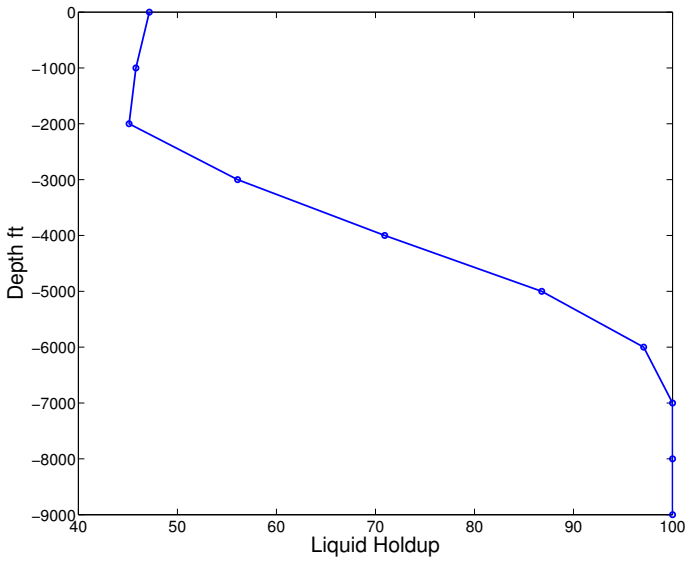

Figure 5.33: Hold up of case 2-B.1.

5.5.2 Flowrate Estimation Results

- Test #1: no pressure information used

Our first estimation was made by specifying profiles of mixing temperature, entry temperature and wellhead phase flowrates of oil and gas. Although we can reproduce the temperature profile perfectly (the mean square error is 0.00046), the estimation of phase flowrates depends on initial guess and converges to a local minimum, which is not unique and thus not acceptable, as shown in Figure 5.34. Transient DTS data are still not sufficient to solve this problem: when we included daily temperature profiles over 20 days as constraints, a unique solution was still not achieved. This result coincides with our discussion in Chapter 4, suggesting that temperature is not very sensitive to phase behavior. On the other hand, pressure is related closely to phase properties, which means pressure data would reduce the uncertainty to a great extent in this problem. Therefore, in the following tests, pressure data were added to

the inverse model to obtain a better estimation.

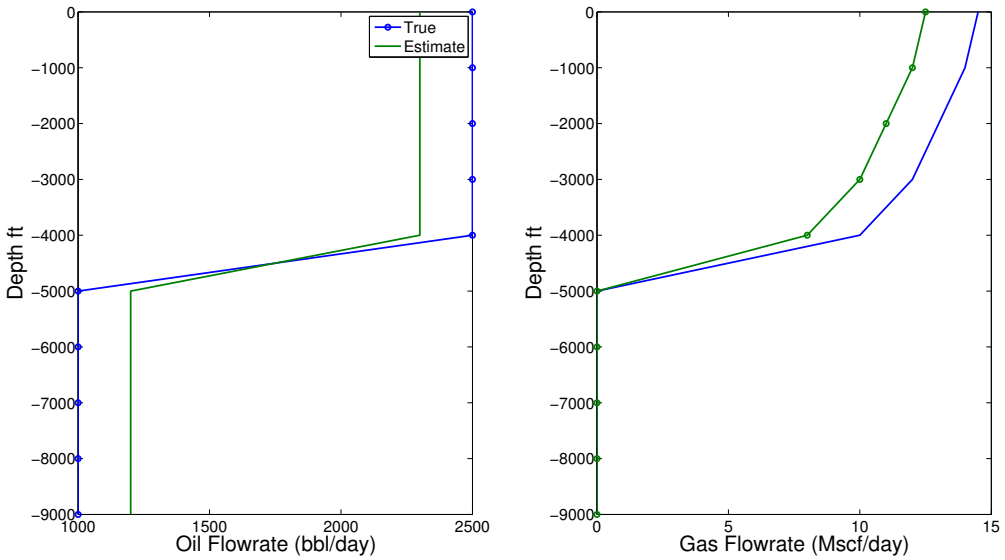

Figure 5.34: Result of Test 1.

- Test #2: single pressure value used

In this test, in addition to the data used in Test #1, a pressure value at a single location (at the wellhead) and a single time point (at the same time of the DTS measurement) was added. As shown in Figure 5.35, the estimation improved, but still was not correct.

- Test #3: pressure profile used

In Test #3, we added more pressure data. To be more specific, we added a pressure measurement point above each entry location to the inverse model. A unique and correct phase flowrate profile (Figure 5.36) is achieved. We also found that the pressure profile data do not have to be measured frequently, and only one pressure data measured above each entry location is sufficient to achieve good estimations of

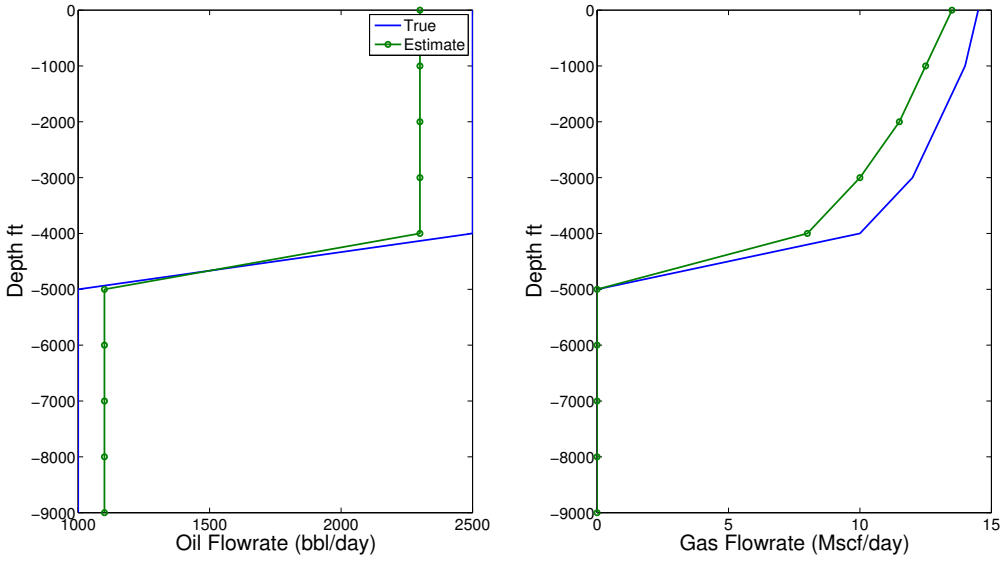

Figure 5.35: Result of Test 2.

phase flowrate profiles. Only two pressure values, one above each entry point, were used, and the estimation of phase flowrates was accurate.

The fact that pressure plays an important role in estimating flowrate profile emphasizes the necessity of applying compositional models in complicated production scenarios. Figure 5.37 shows the estimation of flowrate based on a black-oil model (remember that the synthetic data are simulated by a compositional model) and specifying the same amount of data as in Test #3. The estimation does not reflect the true values.

5.5.3 Three-Phase Flow

We added a certain amount of water to make three-phase flow in case 2-B.2. We assumed that the presence of water does not affect the phase diagram of the composition, and the Chen correlation (Eq 5.38) is still valid to calculate friction factor. Compared with two-phase flow, in the three-phase flow, there are two new unknowns:

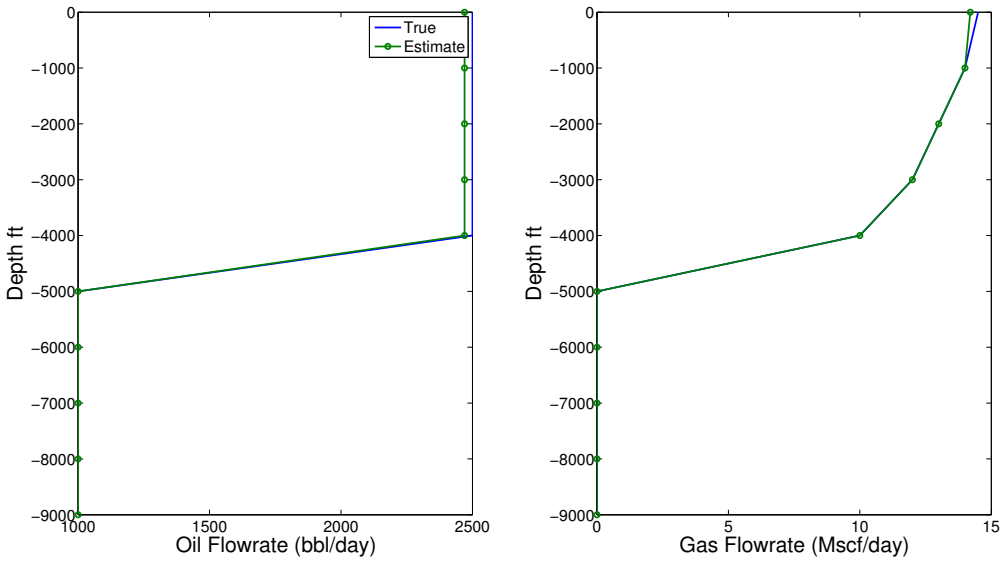

Figure 5.36: Result of Test 3.

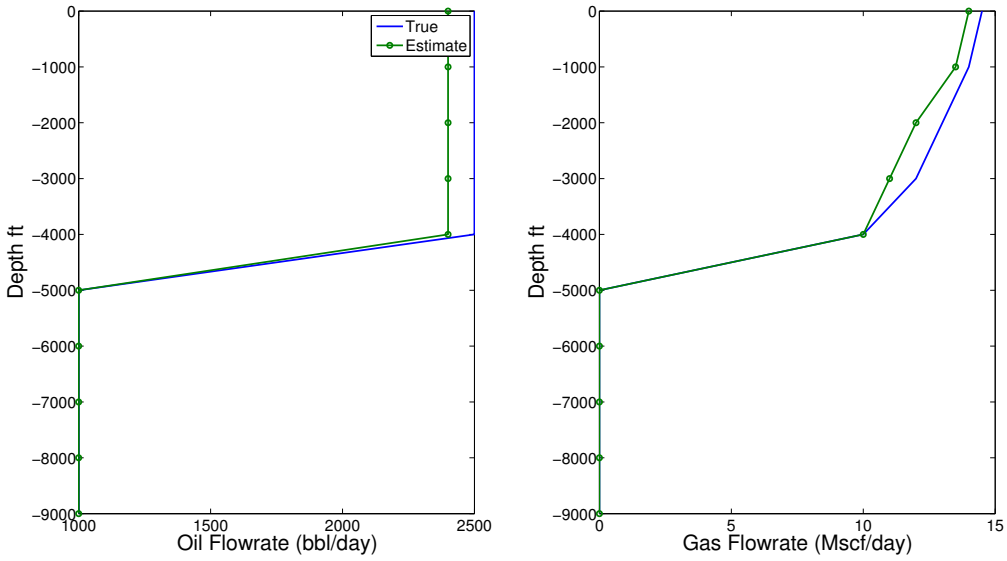

Figure 5.37: Result of using Black-Oil model.

water flowrate from each entry point. We found that even the temperature profile, pressure profile and wellhead flowrate are not sufficient to obtain a unique solution, as shown in Figure 5.38. For three-phase flow, as recommended by Ouyang and Belanger (2006), other information, e.g. in-situ hold-up information, is required to estimate the correct flowrate profile.

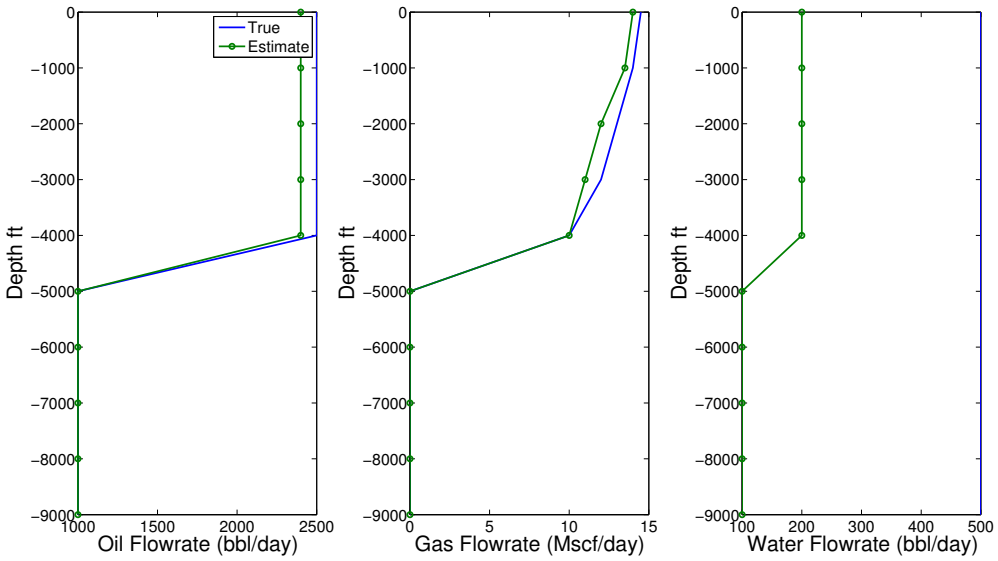

Figure 5.38: Result of estimation three phase flow.

5.6 Summary

In this chapter, two methods, least-square method and linear inverse model, were used to estimate flowrate from temperature data. In addition, two issues of difficulties involving in the inverse modeling, data noise and complicated flow scenarios, were solved. The findings and conclusions are summarized as follows:

1. In this problem, the least square method was not successful when the number of unknowns is large, and it can only handle the case when all the locations of

entry points are known (in which the number of unknowns equals the number of entry points). By contrast, the linear inverse model can give correct estimation of flowrate without knowing the locations of entry points, which avoids the risks and uncertainties associating with the process of locating entry points.

2. Wavelet analysis is very helpful to identify the abrupt changes on temperature profiles, which correspond to the entry points. The way that wavelet decomposes data into several resolutions with different frequencies enables us to find a certain level of resolution, at which the high-frequency variations (usually they are noise) are removed, whereas the low-frequency (the fluid entry points or 'edge') changes are kept.

3. In single-phase flow, several complex production scenarios were studied, and no single case shows failure. Unlike noise, the well configuration (including the deviation angles, distances between layers, the number of layers, etc.) does not affect the estimation much.

4. In two-phase flow, distributed pressure data are also required for a successful estimation of phase flowrates. We showed that a compositional model is necessary in analyzing multiphase flow data, because the precise prediction of pressure is important in flow profiling. For three-phase flow, we have the same conclusion as Ouyang and Belanger (2006) that data sources other than DTS and DPS are required for estimating flowrate profiles successfully.

In all, DTS has the advantage of providing exhaustive dynamic information along the wellbore direction, and it should be interpreted together with other available data to achieve estimates of flow profiles.

Chapter 6

Formation Evaluation by Temperature: Single Entry Analysis

In Chapter 5, wellbore temperature was analyzed to estimate flowrate, and the problem considered only the wellbore domain. However, the temperature signal contains information about the formation properties too. Similar to pressure transient analysis, temperature data are also useful for estimating formation properties. We found that the temperature signal differs from pressure signal in the way it travels through the medium: the temperature signal travels much more slowly than the pressure signal, which means the temperature measured in the wellbore is more sensitive to the near-wellbore region properties than pressure. Based on this observation, our wellbore/reservoir coupled thermal model was used to study the sensitivity of temperature transient data to formation properties, and an inverse problem was solved to estimate near-wellbore formation properties from transient temperature data.

We divide our discussion of evaluating formation properties into two parts: wells with single entry point (single layer reservoirs) and wells with multiple entry points

(multilayer reservoirs and horizontal wells), and these two parts are described in detail in Chapter 6 and 7.

6.1 Damaged Zone Problem

The drilling process usually harms the vicinity surrounding the wellbore, generally as a result of mud or cement filtrate invasion, and this area is called the damaged zone. As shown in Figure 6.1, in between the cement of the wellbore and the formation, there is a damaged zone, in which the permeability could be reduced significantly. This near-wellbore damage affects well productivity. A comprehensive evaluation of this damaged zone is helpful to improve well productivity.

In pressure transient analysis, this damaged zone effect is described by $skin$, which is a dimensionless factor accounting for the additional pressure drop in the damaged zone. If the permeability of damaged zone (denoted as k_d), radius of damaged zone (denoted as r_d) and permeability of the undamaged formation (denoted as k) are known, the skin factor can be calculated by using Eq 6.1.

$$s = (\frac{k}{k_d} - 1) ln \frac{r_s}{r_w} \tag{6.1}$$

The damaged zone has two parameters: permeability (k_d) and radius (r_d). The effects of these two parameters are combined in Eq. 6.1, and cannot be distinguished by the skin factor. It would be a better approach to evaluate the damaged zone if these two effects could be described separately. Both Sui et al. (2008) and Duru et al. (2011) show that the transient temperature signal is sensitive to the permeability and radius of the damaged zone. As shown later in Section 6.3, unlike the pressure history, which is not sensitive to radius and permeability of damaged zone, the temperature history shows different signatures for different values of damaged zone radius and permeability. Therefore, it is possible to use temperature history to estimate these

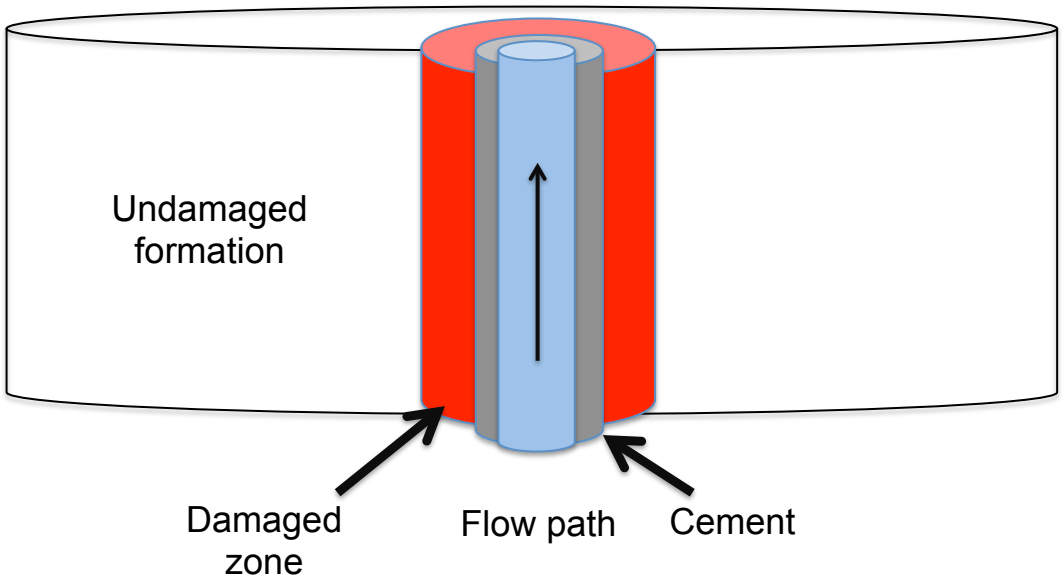

Figure 6.1: Damaged zone in the near wellbore region.

two parameters, which are not distinguishable in pressure data. Before the estimation results are presented, the 'ring' model used in this study is explained first.

6.2 Ring Model

To model the damaged zone problem, we used a model which consists of two 'rings'. As shown in Figure 6.2, both the cement and damaged zone are in the near-well ring, while the undamaged formation is the outer ring. These two rings have different permeability values. Therefore, the damaged zone can be modeled by the near-well ring, and the undamaged formation is modeled by the outer ring. Through this ring model, the parameters that are relevant to the damaged zone problem: damaged zone permeability (k_d), radius (r_d) and formation permeability (k) are all included.

The same gridding method described in Chapter 4 was applied to this ring model, the real space (Figure 6.2) was discretized by nonuniform cells in a cylindrical coordinate system, and different cells can be assigned different permeability values.

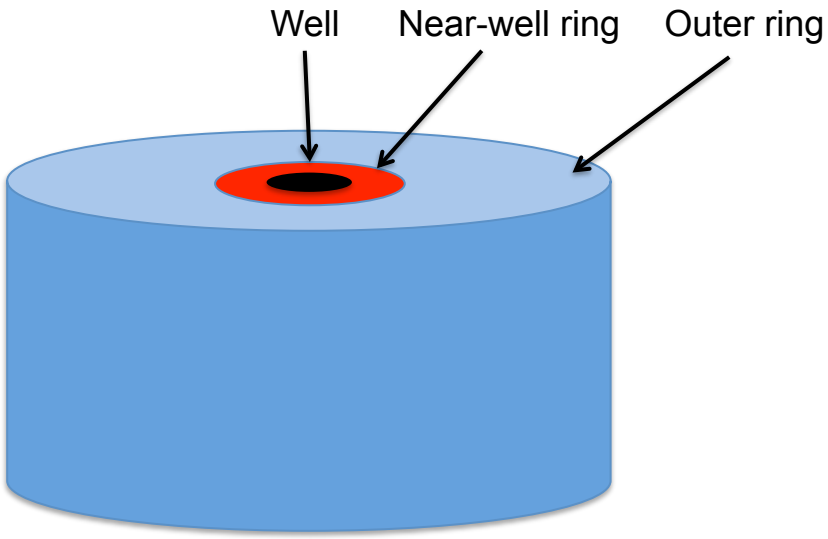

Figure 6.2: Damaged zone problem modeled by the ring model.

6.3 Sensitivity Test

We constructed six cases to study the sensitivity of pressure and temperature signals to damaged zone properties. The parameters of these six cases are listed in Table 6.1. The skins listed in the table were calculated by Eq. 6.1. These six cases have the same formation permeability, but different damaged zone properties. For the first three cases, they also have different skin factors, while the last three cases have the same skin factor.

Table 6.1: The parameters of the six cases

Case	$r_d(md)$	$k_d(md)$	$k(md)$	Skin
1	5	10	50	6.44
2	5	5	50	14.48
3	5	2	50	38.63
4	20.00	10	50	11.98
5	3.79	5	50	11.99
6	1.65	2	50	11.99

Pressure transient analysis has been used widely for estimating formation properties, in which the pressure derivative over time shows distinctive signatures for different flow periods. As shown in Figure 6.3, the pressure derivatives of the cases with different values of skin factor are easy to distinguish. However, the pressure derivative is only sensitive to skin factor, but not to the damaged zone radius and permeability. As shown in Figure 6.4, the pressure derivatives for case 4, 5 and 6 overlap each other, even though the damaged zone radius (r_d) and permeability (k_d) of these cases are different (while skin factors are the same). This observation confirms our previous statement that pressure transient analysis can only be used to estimate skin factor, but not the radius and permeability of the damaged zone.

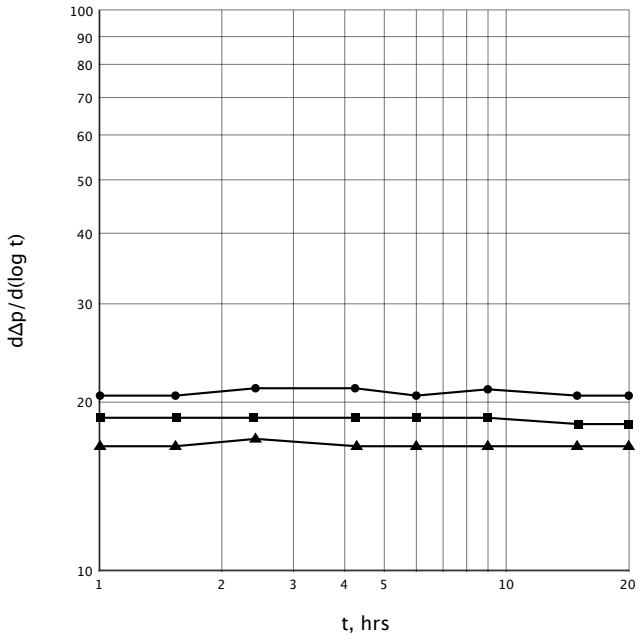

Figure 6.3: Pressure derivative of the three cases with different skins.

When we examine the temperature transient behavior for these six cases, as shown in Figure 6.5 and 6.6, both the temperature and temperature derivative curves show different shapes for each case. Especially on the temperature derivative curve, there are clearly two parts with different slopes, which correspond to different radii of

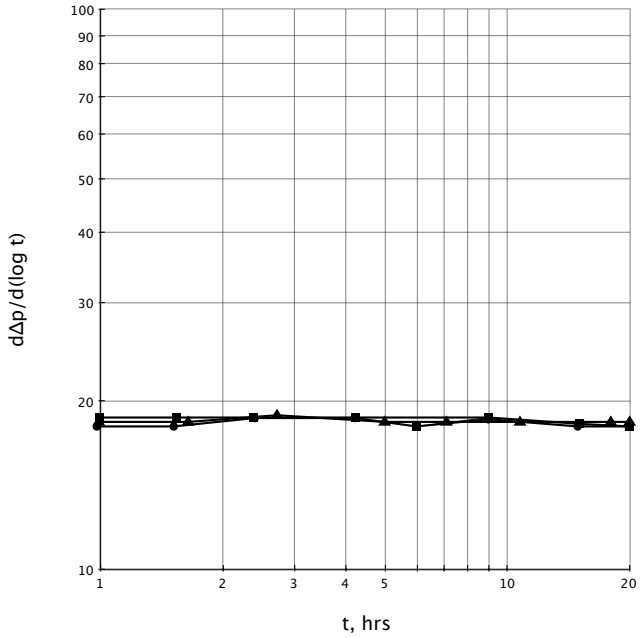

Figure 6.4: Pressure derivative of the three cases with the same skins.

investigation. The early part is characterized by the damaged zone: the slope is determined by the damaged zone permeability; while the slope of the late part is a function of undamaged zone permeability. Because these six cases share the same formation permeability, the slope of the late part is the same for all six cases. There is a transition period between the early and late parts. The time of the transition indicates the size of the damaged zone. Therefore, all the three parameters describing the damaged zone properties: k_d, k and r_d can be distinguished respectively by the slopes of early part and late part, and the time of the transition period on the temperature derivative curve.

6.4 Inverse Modeling and Results

In the inverse problem, the unknowns are permeability (k_d) and radius (r_d) of the damaged zone, and the permeability (k) of the formation. The available data are the

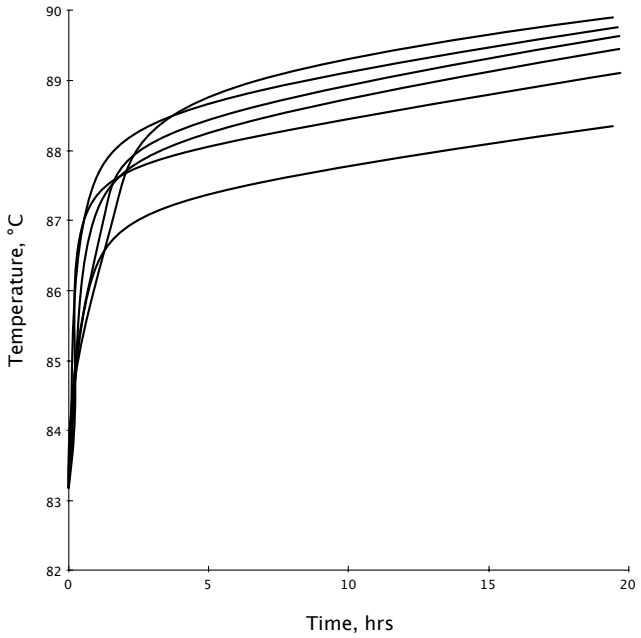

Figure 6.5: Temperature history of six cases.

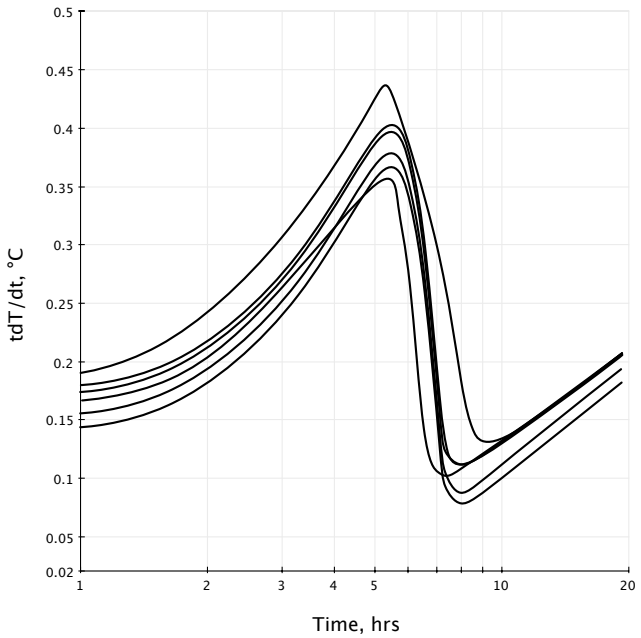

Figure 6.6: Temperature derivative of six cases.

fluid properties, temperature history (T_t) and flowrate history (q_t). A set of synthetic data (named as case 3-A.1) were generated by our wellbore/reservoir coupled thermal model based on the parameters shown in Table 6.2, and the flowrate and simulated temperature histories are shown in Figure 6.7.

We used the Least-Square method discussed in Chapter 5 to solve the inverse problem. As shown in Figure 6.8, the estimated three parameters k_d, r_d and k are close to the true values. Moreover, the calculated values of skin (Eq. 6.1) by using the estimated values and true values can match.

Table 6.2: Case 3-A.1 parameters

Formation permeability (md)	$50md$
Damaged zone radius (ft)	$5ft$
Damaged zone permeability (md)	$10md$
Skin	6.43
Fluid density (kg/m^3)	800
Heat capacity ($J/kg/k$)	1601.8
Tubing radius ($inch$)	1.5

- Data noise

  If the temperature history is augmented with noise, the presence of noise will deteriorate the estimation. In case 3-A.2, the temperature data used in case 3-A.1 were modified by adding random noise with different signal-to-noise ratios, 20 dB, 10 dB and 5 dB respectively (Figure 6.9). The estimations became worse as noise increased (Figure 6.10). None of the results are acceptable, and when noise is 5 dB, the results stay at the initial guess.

  The noise in flowrate history also affects the results. In case 3-A.3, flowrate data were modified by adding noise with signal-to-noise ratio of 10 dB (Figure 6.11), while temperature data are still noise-free in this case, and the estimation results are shown in Figure 6.12).

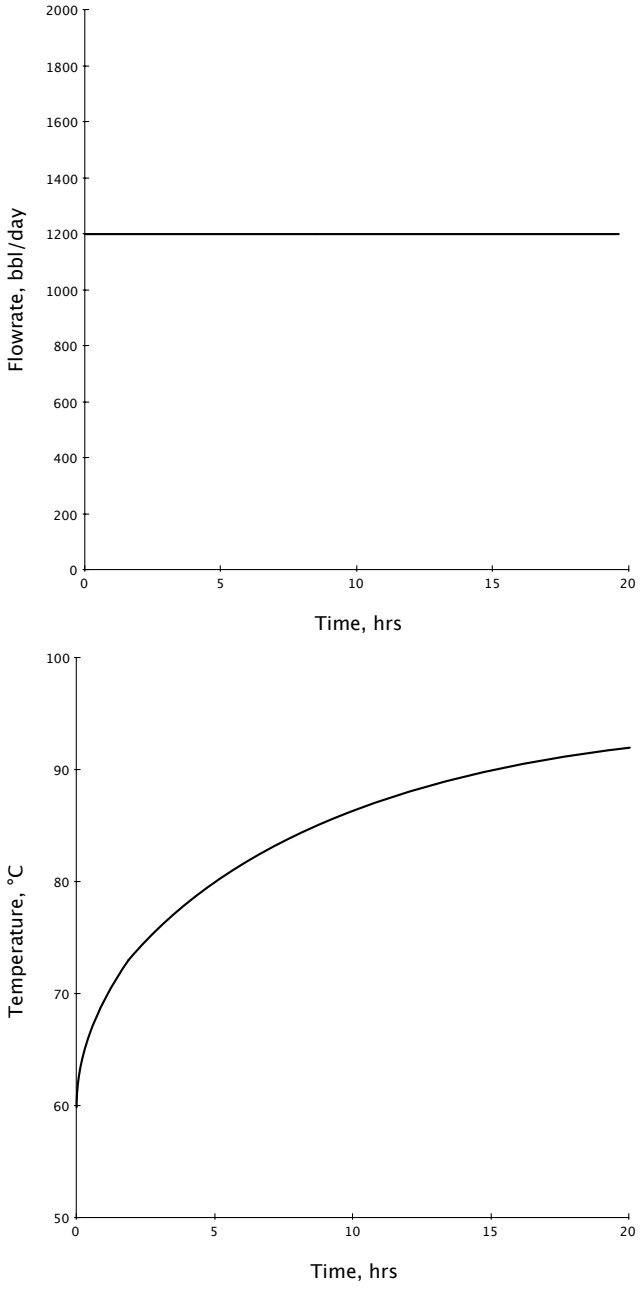

Figure 6.7: Flowrate and temperature histories.

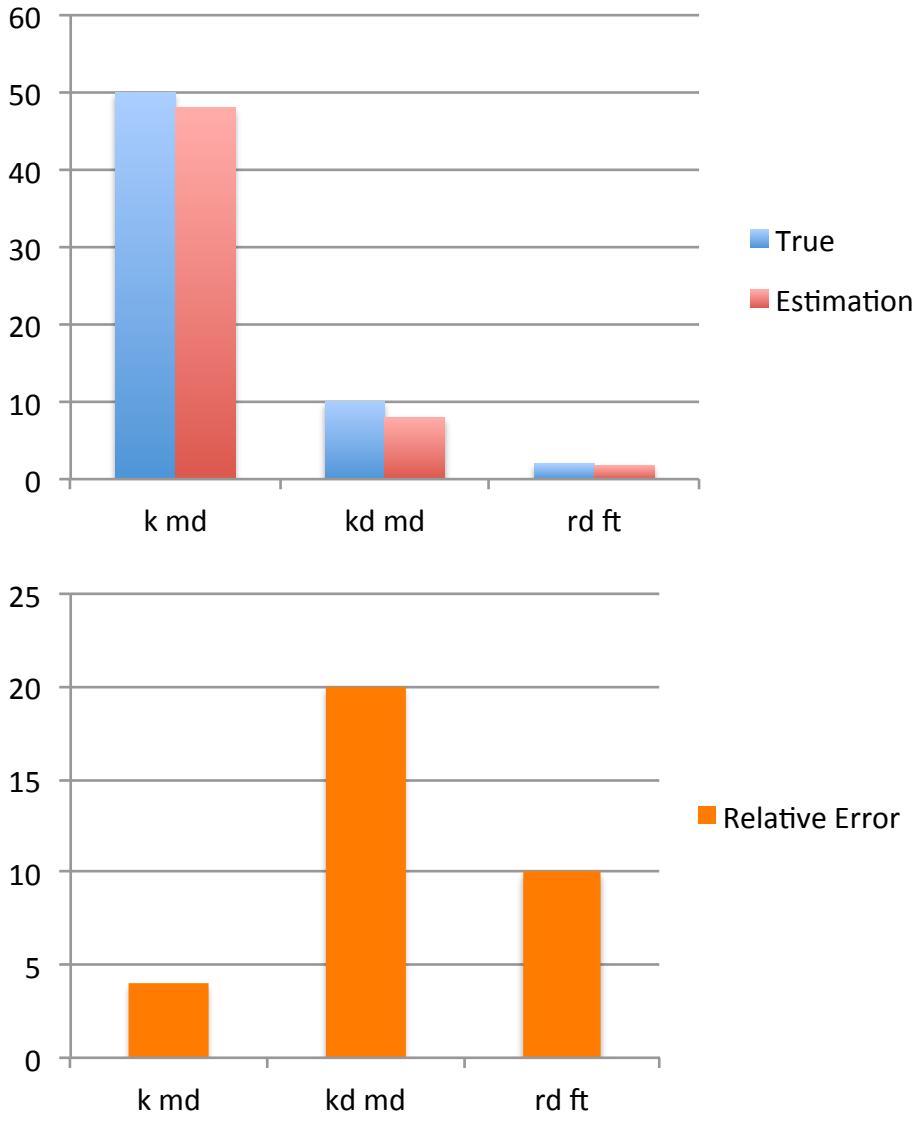

Figure 6.8: Estimation results of case 3-A.1.

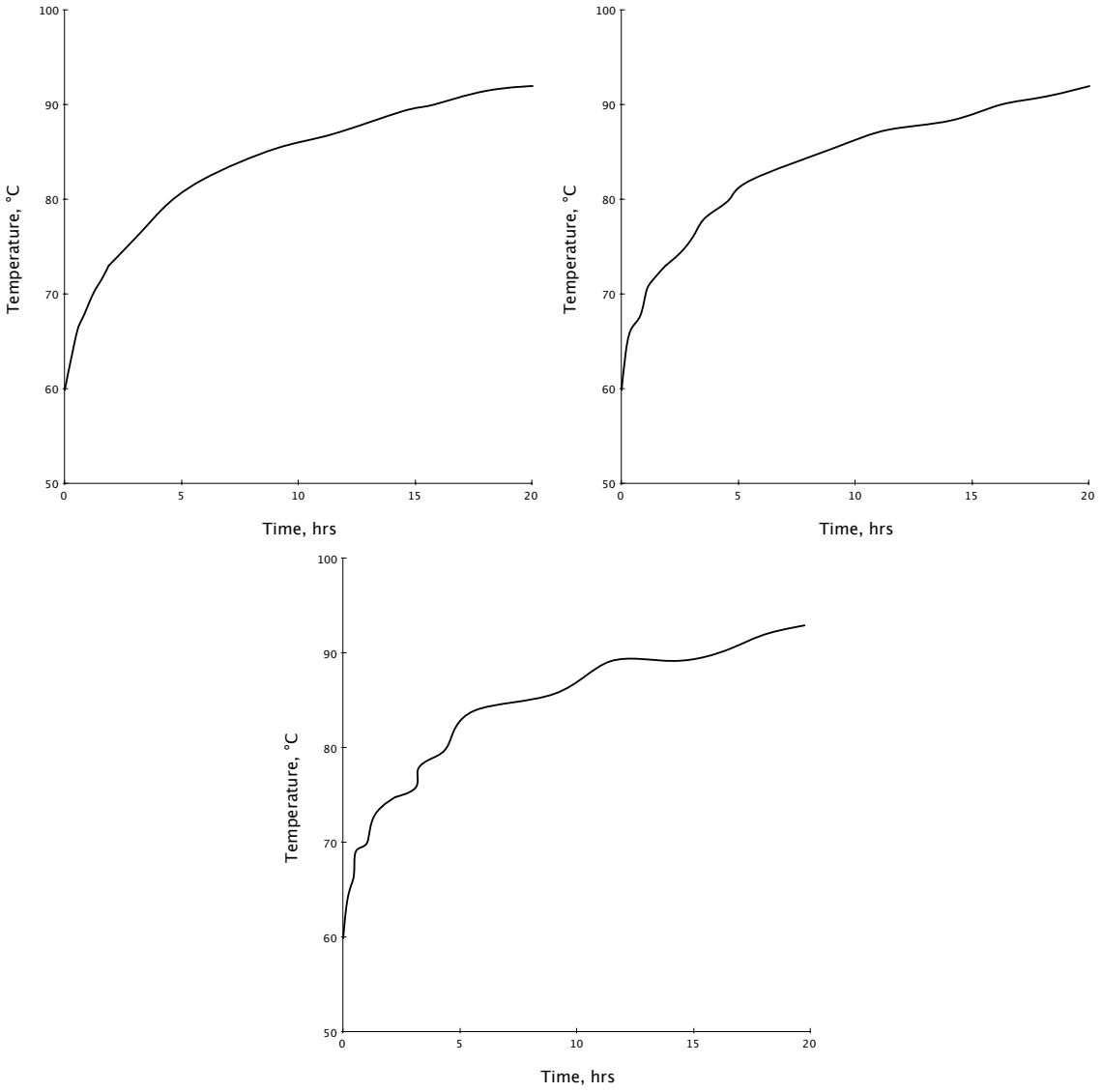

Figure 6.9: Temperature history with noise of Signal-Noise Ratio 20 dB, 10 dB and 5 dB respectively, case 3-A.2.

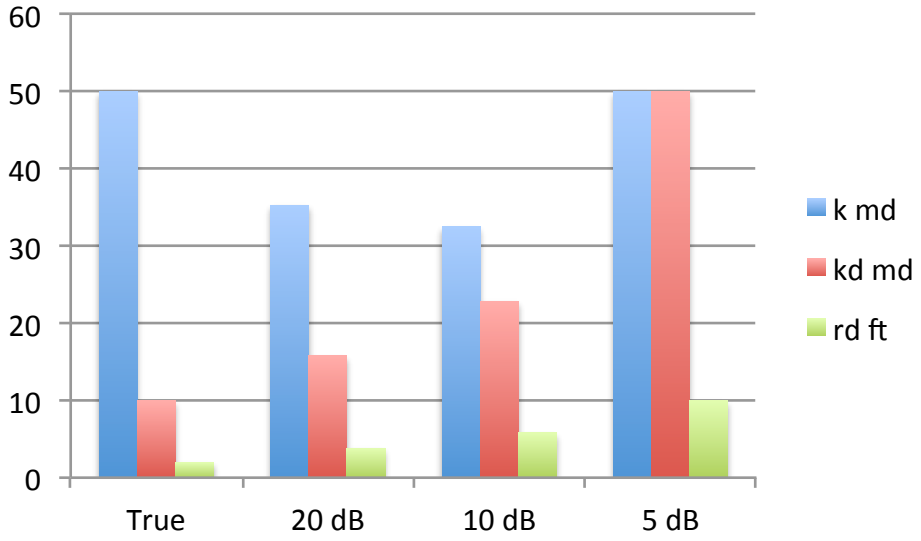

Figure 6.10: Estimation results of case 3-A.2.

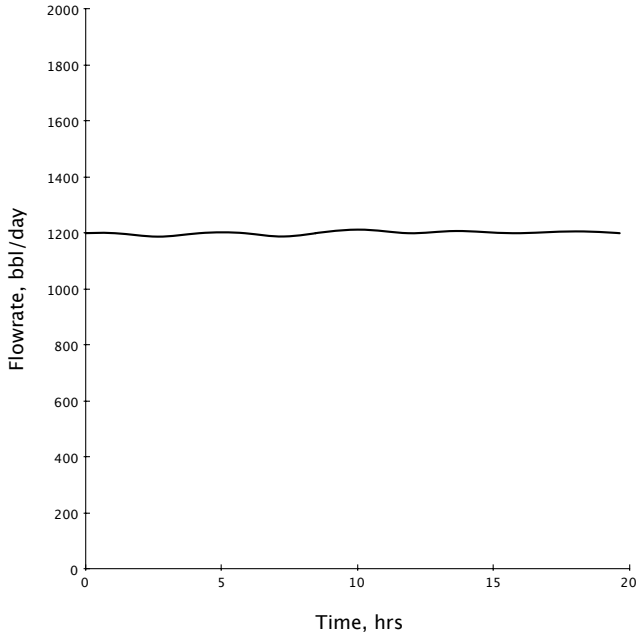

Figure 6.11: Noisy flowrate history, case 3-A.3.

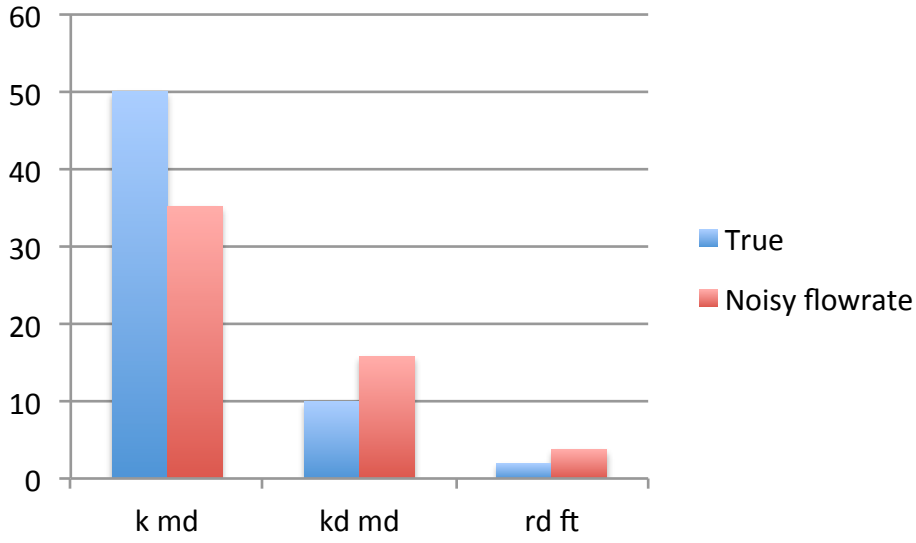

Figure 6.12: Estimation results of case 3-A.3.

- Data resolution

  In case 3-A.1, the synthetic data were generated with a temperature data point every 2.4 minutes (500 points for 20 hours), but if the temperature is measured at a lower frequency, e.g., every 12 minutes (100 points) and 24 minutes (50 points) (these two cases are numbered as case 3-A.4), the shapes of the temperature derivative will change (Figure 6.13). Therefore, if the temperature is measured at a low temporal frequency, the estimations will be misleading, as shown in Figure 6.14.

Aiming to find the limit of the parameters values that are estimable by temperature data, we made a large collection of cases to test the inverse model. This case space was generated by the following approach:

- Ten values of radius of damaged zone (r_d) were picked randomly from 1 ft to 10 ft, and ten values of permeability of damaged zone (k_d) were picked randomly from 0.1 md to 10 md to have ten combinations of r_d and k_d (as the value

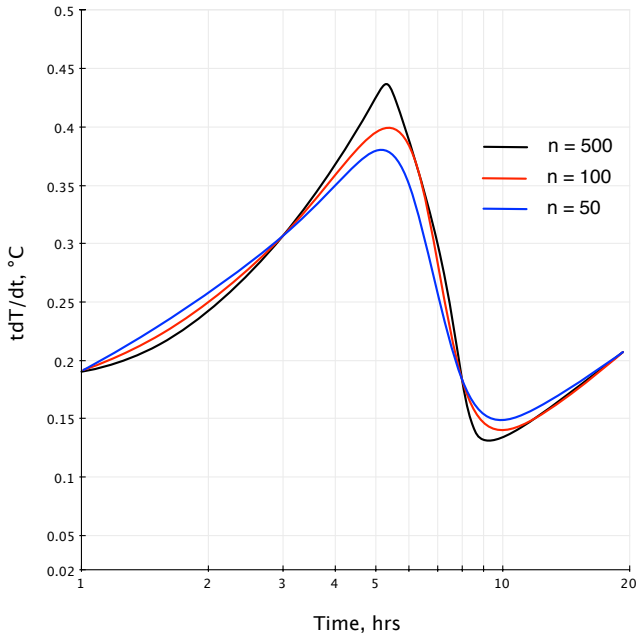

Figure 6.13: Temperature derivative of the data with different measurement frequency. Black line-data measured every 2.4 min; red line-data measured every 12 min; blue line-data measured every 24 min.(Case 3-A.4)

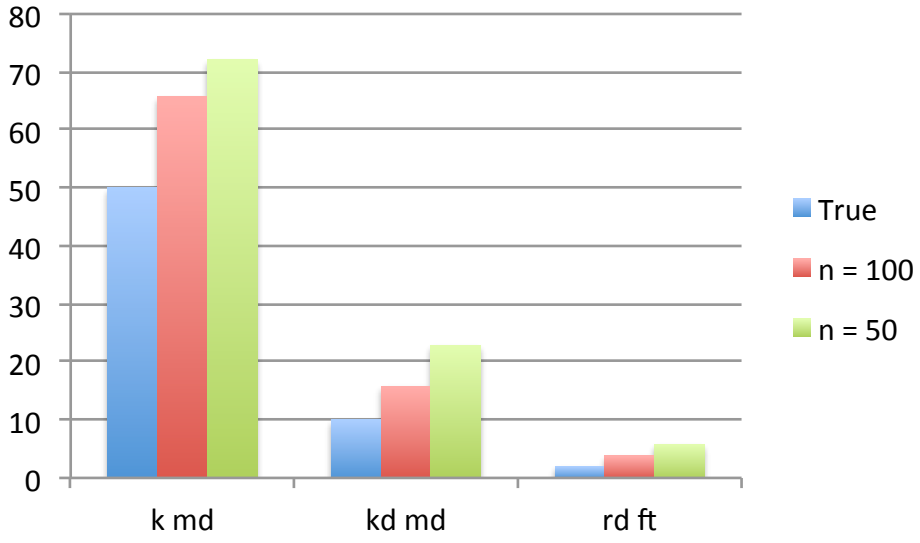

Figure 6.14: Estimation results of case 3-A.4.

assignment is random, only one example is shown in Figure 6.15). Subsequently, permeability of formation (k) was assigned from 1 md to 100 md. Thus, ten combinations of r_d and k_d and the ten values of k can form a 10x10 matrix, which is the case space. As shown in Figure 6.15, the 10 combinations of k_d and r_d form the volumes of the matrix, while the 10 values of k form the rows of the matrix.

We estimated r_d, k_d and k of individual cases in the 10x10 matrix in Figure 6.15, and calculated the relative error of k_d, r_d and k of each case. In these 100 cases, the relative errors of k_d and r_d are in the same range, from 5% to 15%, and they are larger than the relative errors of k, which varies from 2% to 8%. We generated the case-space matrix (Figure 6.15) three times, and did not find a single case in which the relative error exceeds a reasonable range.

All these cases were based on Case 3-A.1, in which the well has a simple production scenario. Sui et al. (2008) studied a similar production scenario, and also estimated permeability and radius of damaged zone successfully. In our research, to better understand the applicability of using temperature to estimate formation properties, we studied several cases with more complicated situations, and results are shown in the next section.

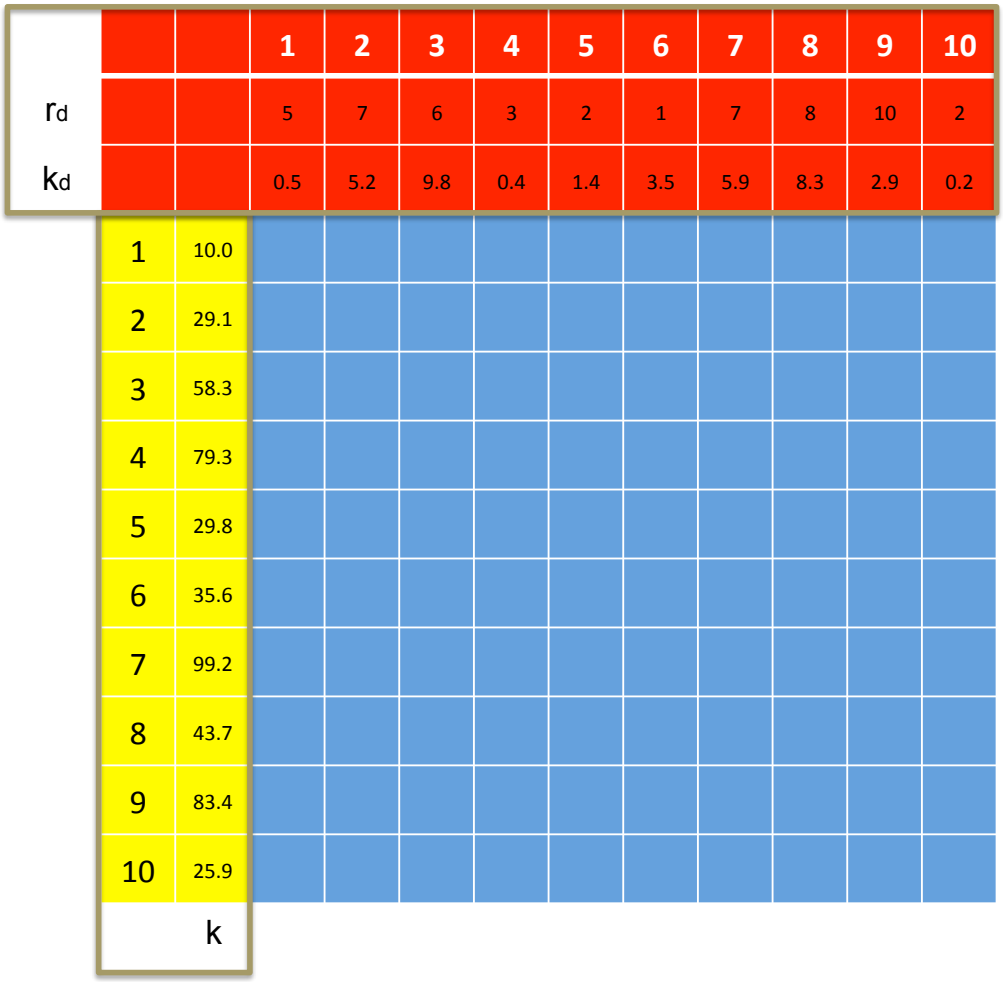

Figure 6.15: The case space.

6.5 More Cases

6.5.1 Skin Factor of Asymmetric Damaged Zone

In practice, the damaged zone may not be symmetric around the well. As shown in Figure 6.16, the cross section of the damaged zone is not a concentric circle, and the properties are not homogeneous within the damaged zone. Therefore, the skin factor in each direction is different. By using the traditional single-point measurement, which only takes measurements at the axis of the well, the skin factor in each direction cannot be estimated. However, for DTS technique, due to the small size of the fiber, several fibers can be installed at various locations around the wellbore. As a matter of fact, for the purpose of avoiding the damage by perforation guns, in practical applications it is common to run several fibers strapped around the casing in order to raise the chances that the fibers will survive.

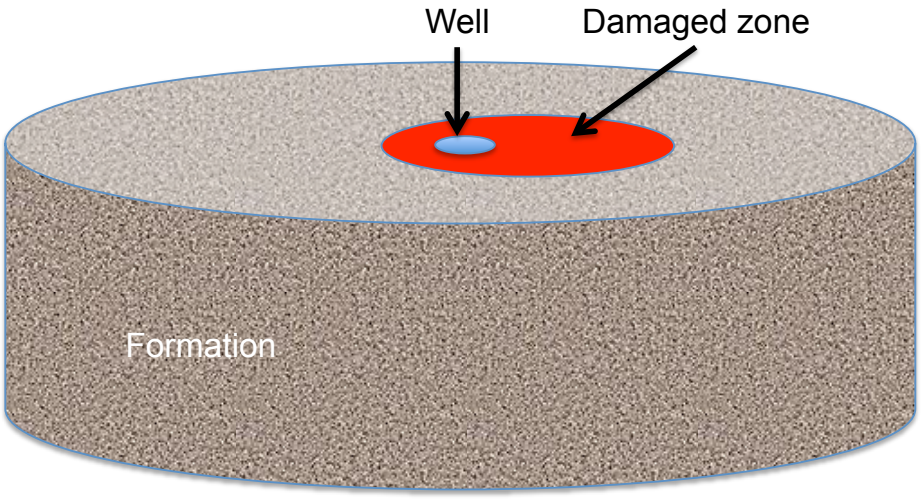

Figure 6.16: Sketch of an asymmetric damaged zone.

To study this asymmetric damaged zone problem, the ring model (originally shown in Figure 6.2) was modified: the rings were divided into several partitions, and these partitions could communicate with each other. Thus, each simulation cell has an

additional parameters k_c to describe the flow in the circumferential direction. In addition, each individual partition can be assigned with different properties to model the asymmetric damaged zone.

For the case (numbered Case 3-B.1), shown in Figure 6.17, there are three partitions, the properties of which are shown in Table 6.3. Three fibers were installed in these three partitions, and the temperature histories of these three segments were measured before the entry fluids were mixed together (Figure 6.18). By specifying these temperature histories as well as fluid properties in the inverse model, the results of estimating damaged zone permeability, radius and formation permeability are shown in Table 6.3. The estimation was not acceptable for all three partitions. In another case, case 3-B.2, the k_c is set to be zero, and thus there is no interpartition flow. The estimation became acceptable (Table 6.4). By comparing cases 3-B.1 and 3-B.2, it is clear that the interpartition flow affects the estimation results. The influence of k_c is shown in Figure 6.19, which is a scatter plot of the estimation of k_c. In these cases, three partitions share the same k_c/k ratio. Figure 6.19 shows a trend that the estimation becomes worse as k_c/k ratio increases.

Table 6.3: Estimation results of case 3-B.1

Partition 1	k_d	r_d	k	k_c
True	2	10	20	5
Estimate	1.5	22.5	16.3	4.2
Partition 2	k_d	r_d	k	k_c
True	5	5	100	10
Estimate	1.3	25.5	88.3	1.2
Partition 3	k_d	r_d	k	k_c
True	10	2	100	10
Estimate	1.3	10.0	92.2	1.4

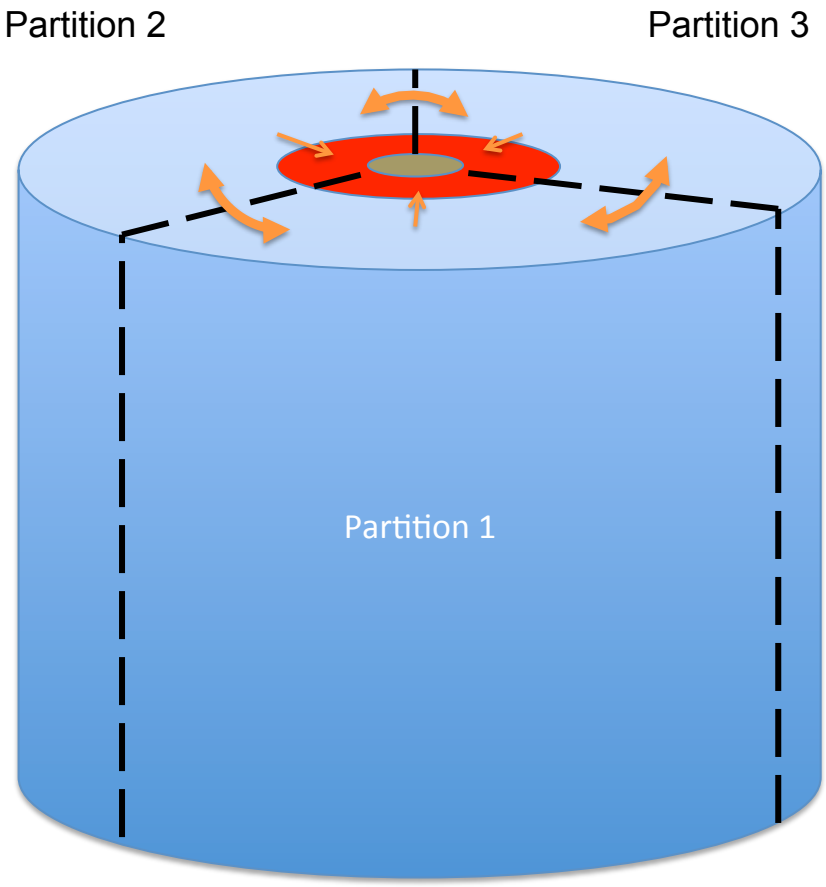

Figure 6.17: Sketch of the partitioned ring model.

Table 6.4: Estimation results of case 3-B.2

Partition 1	k_d	r_d	k
True	2	10	20
Estimate	1.75	12.5	18.3
Partition 2	k_d	r_d	k
True	5	5	100
Estimate	4.3	4.5	88.3
Partition 3	k_d	r_d	k
True	10	2	100
Estimate	11.3	1.1	93.2

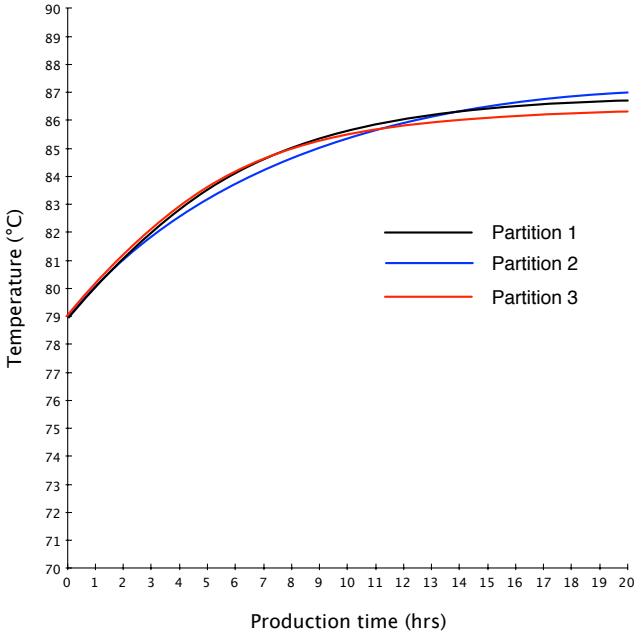

Figure 6.18: Temperature histories of three partitions of case 3-B.1.

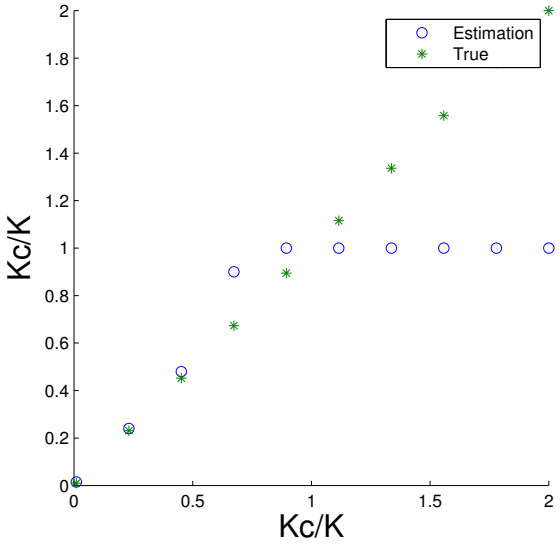

Figure 6.19: The scatter plot of estimation of k_c/k.

6.5.2 Gauge Placed Above the Entry Point

The temperature measurement point might be above the fluid entry point, as shown in Figure 6.20. Due to heat transfer between the fluid and the formation when the fluid flows along this distance, the shape of temperature derivative will change. In case 3-C.1 (input parameters are the same as case 3-A.1 listed in Table 6.2), temperature was measured 500 ft above the fluid entry point. The gap between the gauge and the entry point distorted the shape of the temperature derivative, as shown in Figure 6.21. Therefore, if the gap is ignored, the temperature history can be reproduced by a wrong set of damaged zone and formation properties, and the estimations will be misleading. However, if the gap is acknowledged and specified accurately, the temperature data can still give a good estimation of the damaged zone and formation properties (Figure 6.22).

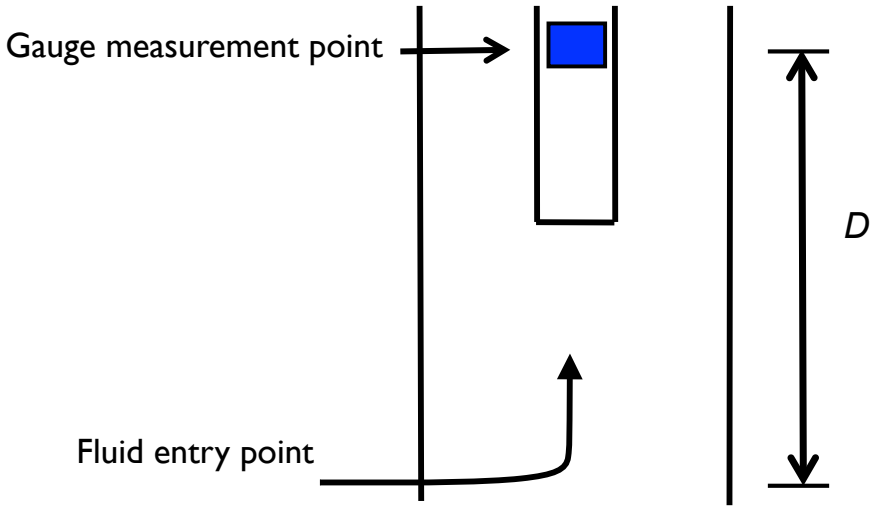

Figure 6.20: Gauge is placed above the fluid entry point.

The heat loss of the flow will be large if the flowrate is very low. In case 3-C.2, the distance is kept as 500 ft, and the flowrate is reduced to 100 bbl/day, and the temperature derivative is affected (Figure 6.23). In this case, even if the correct gap

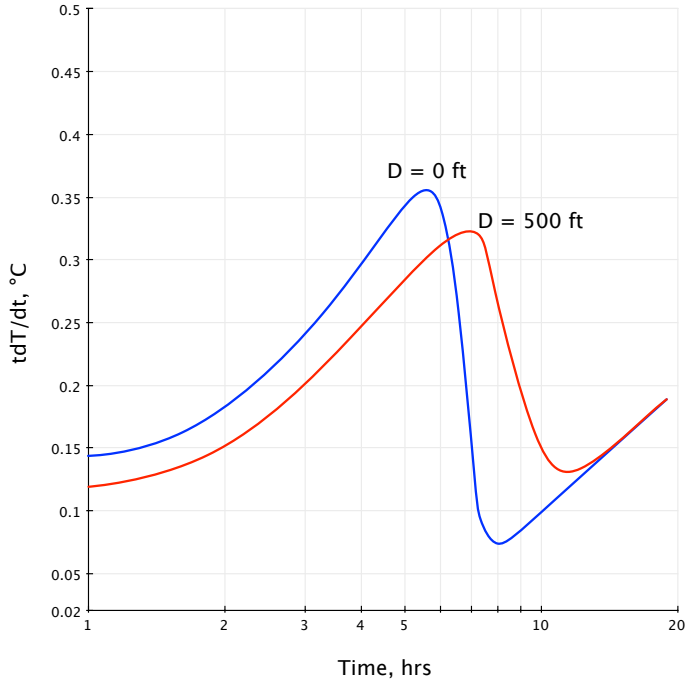

Figure 6.21: The temperature derivative when gauge is 500 ft above the entry point.

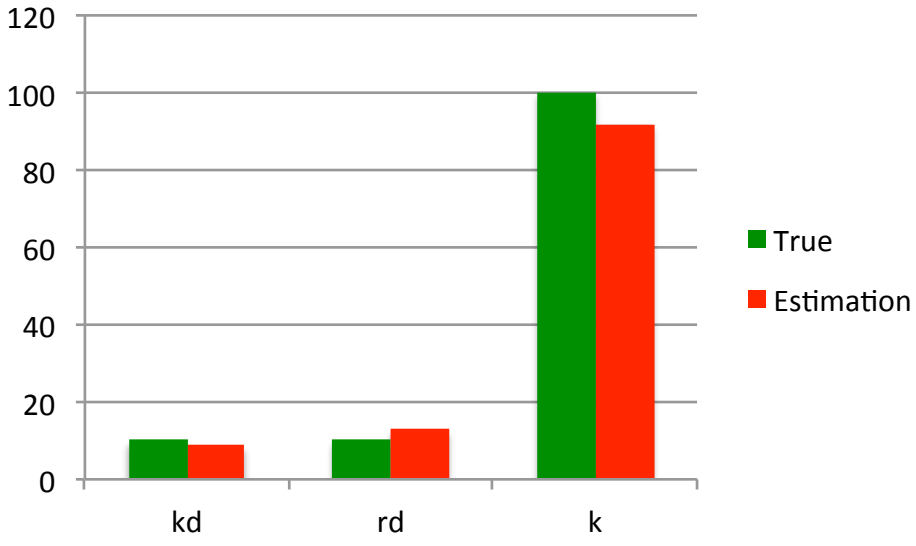

Figure 6.22: Estimations of case 3-C.1 when the gap is known.

distance is specified, the estimation is still not acceptable (Figure 6.24). Therefore, it is recommended to run the fiber past the entry points rather than ending it above them.

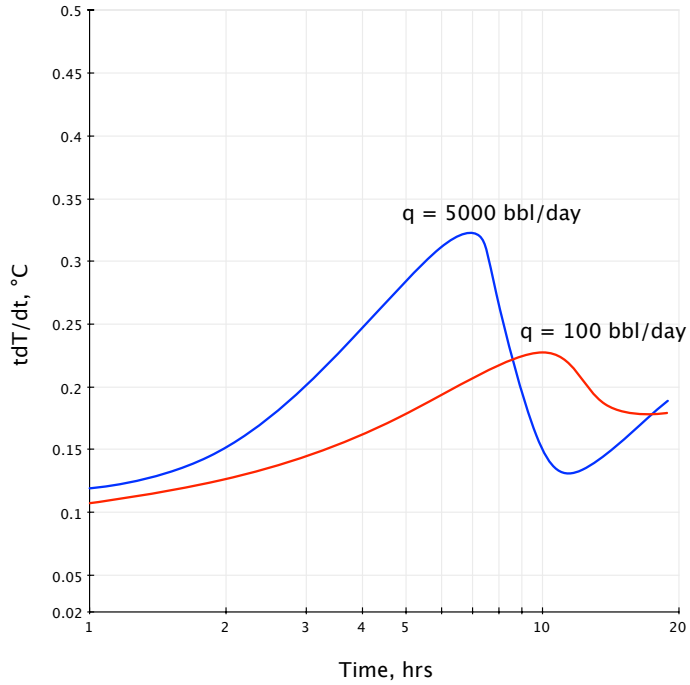

Figure 6.23: Temperature derivative when gauge is 500 ft above the entry point, and flowrate is 100 bbl/day.

6.5.3 Multiphase Flow

In case 3-D.1, there is a water-oil two-phase flow, and no damaged zone in the formation. In the forward modeling process, the effective permeability of water and oil (k_w and k_o) and total flowrate were specified, and temperature history of the fluid could be generated. We first notice that the entering temperature (T_e) is sensitive to water saturation in water-oil two-phase flow (Figure 6.25). Therefore, in the inverse model, if the relative permeability curve, total flowrate history and temperature history are

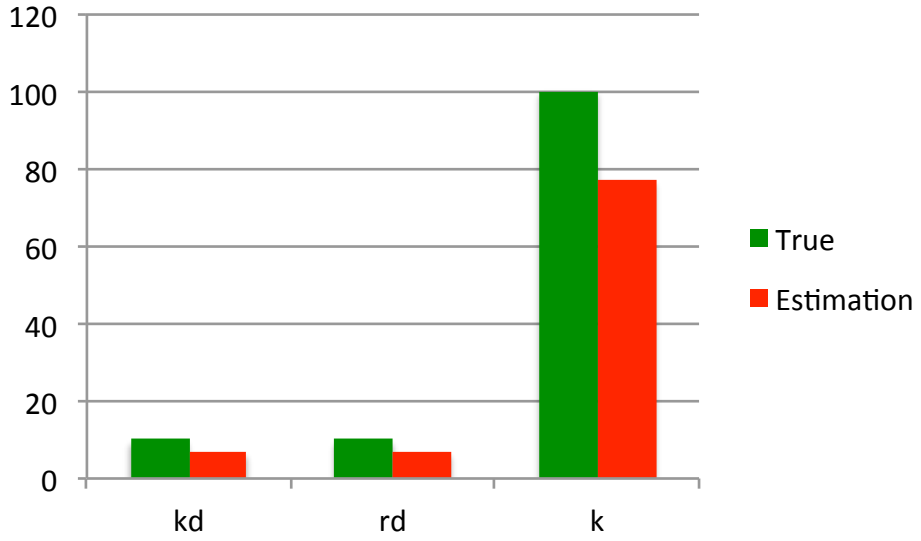

Figure 6.24: Estimation results of case 3-C.2

known, while the total permeability (k) is set as unknown, the estimation is close to the true value (Table 6.5).

Table 6.5: Estimation results of case 3-D.1

	True	Estimation
Permeability (md)	50.0	49.2

However, in contrast to case 3-D.1 which does not have a damaged zone, case 3-D.2 has a damaged zone, and thus we have two additional unknowns in the inverse model: r_d and k_d. The estimation result is shown in Figure 6.26. Although the estimation of formation permeability is acceptable, the estimations of k_d and r_d are far from satisfactory. The multiphase flow brings another uncertainty into the inverse problem. Water saturation and damaged zone may have the same effect: either a high water saturation or a large damaged zone can lead to a high entry temperature (T_e). Just by using temperature data, these unknowns are not distinguishable. Pressure was also added to reduce the uncertainty, but as pressure is not very sensitive to water saturation in single layer flow, the estimation cannot be improved with the

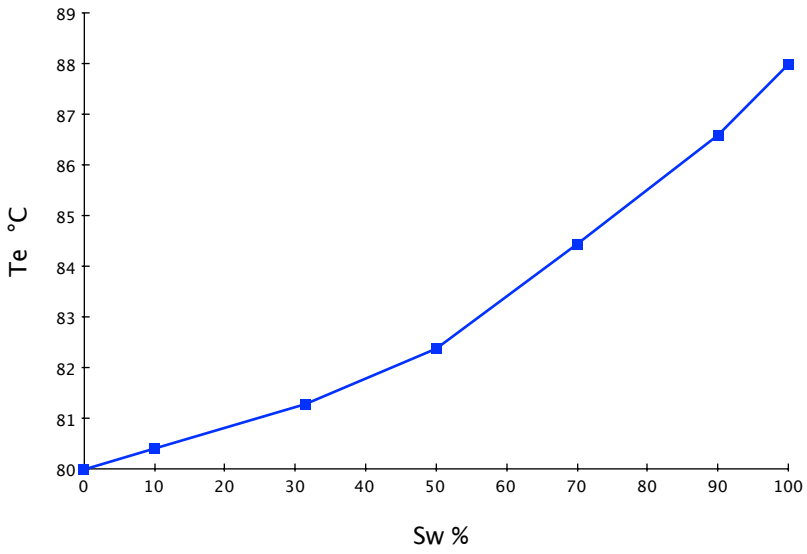

Figure 6.25: Entering temperature is a function of water saturation.

help of pressure. Other sources of data might be more helpful for solving this inverse problem, e.g. water saturation measurement.

6.5.4 Heterogeneity

Cases 3-E.1 and 3-E.2 were built to study the effect of heterogeneity. In both cases, there are five rings, as shown in Figure 6.27. These five rings have different permeabilities, listed in Table 6.6. Case 3-E.1 is to study the sensitivity of temperature to local heterogeneity. As shown in Figure 6.28, the temperature history of Case 3-E.1 almost overlaps a homogeneous case, and the estimation cannot identify the heterogeneity (Figure 6.29).

Table 6.6: Permeability for case 3-E.1 and 3-E.2

Ring	1	2	3	4	5
Case 3-E.1	20.0	20.0	20.0	5.0	20.0
Case 3-E.2	15.0	5.0	28.0	10.0	59.0

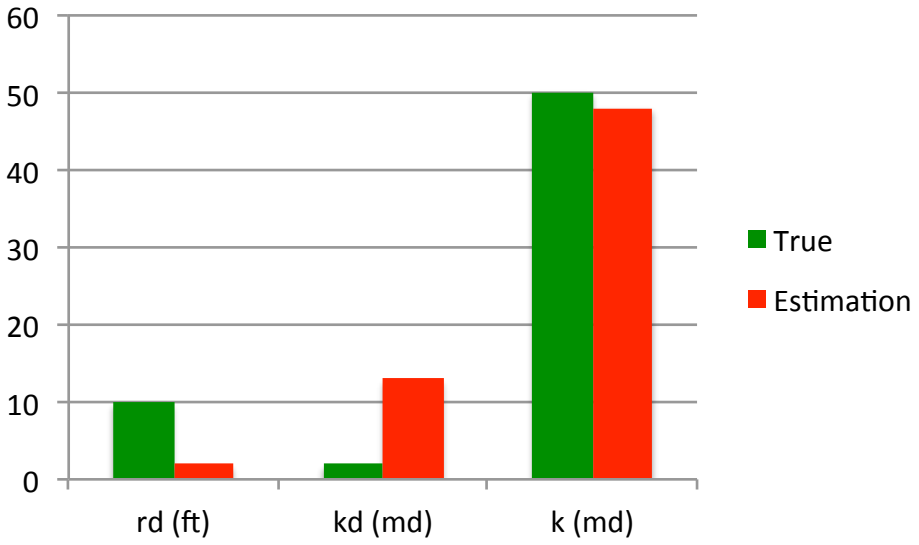

Figure 6.26: Estimation results of case 3-D.2

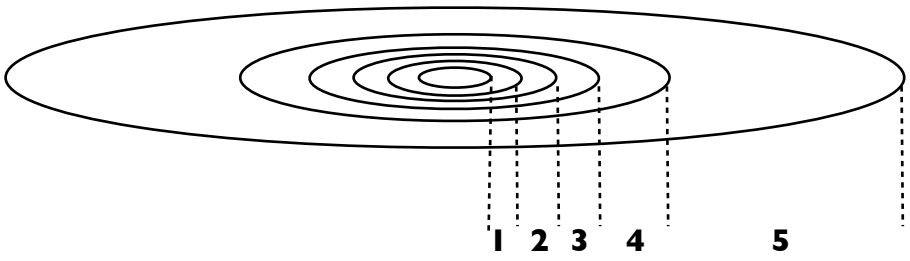

Figure 6.27: The five-ring model for case 3-E.1 and 3-E.2.

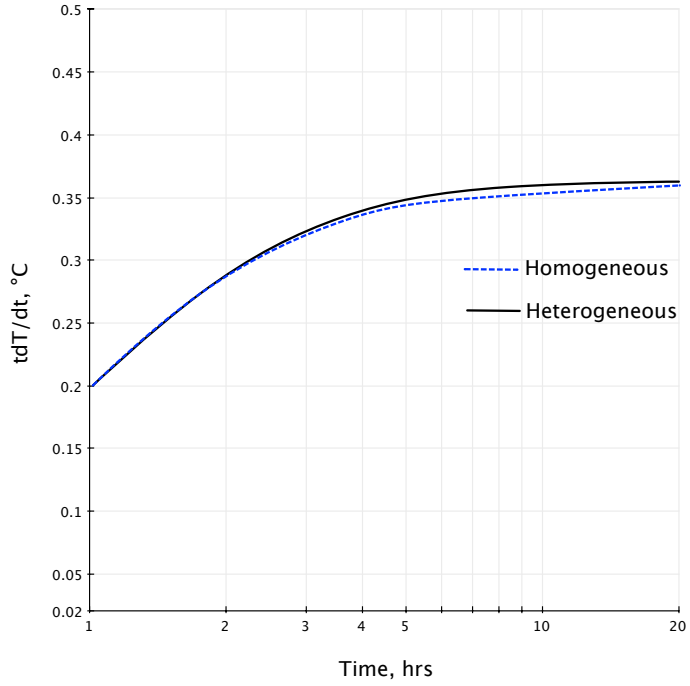

Figure 6.28: Temperature derivatives of the homogeneous case and the locally heterogeneous case (3-E.1).

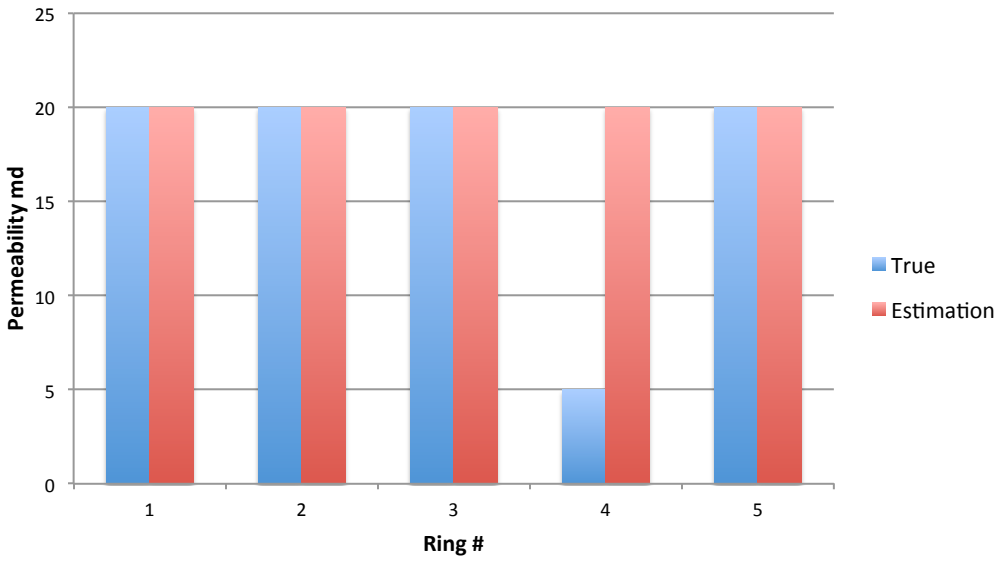

Figure 6.29: Estimation results of case 3-E.1.

In case 3-E.2, the five rings were very heterogeneous, and were assigned random permeability values between 1 md to 100 md, as listed in Table 6.6. The estimation could not reconstruct the heterogeneous permeability, but the area-weighted arithmetic mean of the estimation did match the true value (true = 42.1 md, estimation = 40.2 md).

6.5.5 Initial Temperature

The drilling process usually reduces the temperature in the near wellbore region, and thus the geothermal temperature measured in the wellbore immediately after the drilling process is misleading. This wrong geothermal temperature will affect the temperature derivative analysis.

In case 3-F.1, the geothermal temperature in the near-well region is distorted by the drilling process (Figure 6.30). When the wrong initial geothermal temperature (red curve in Figure 6.30) is used in the inverse model, the estimation is incorrect (Figure 6.31).

However, we note that the wellbore temperature has a tendency to restore to the true geothermal temperature when the fluid stops flowing. In case 3-F.2, we considered a shut-in period for 10 hours, and the temperature history is shown in Figure 6.32. After the initial temperature was set as an unknown in the inverse model, the estimation became acceptable (Figure 6.33).

6.6 Summary

In this chapter, the transient temperature data were used to estimate formation properties successfully in most cases. Different from the pressure transient signal, the temperature transient is transported in the formation more slowly, and thus more sensitive to the properties of near wellbore formation. Therefore, to evaluate the

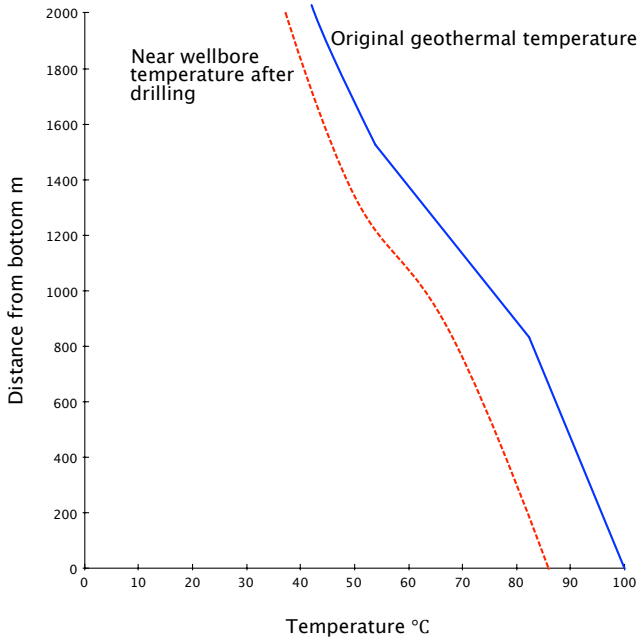

Figure 6.30: Near-well temperature is reduced by drilling process.

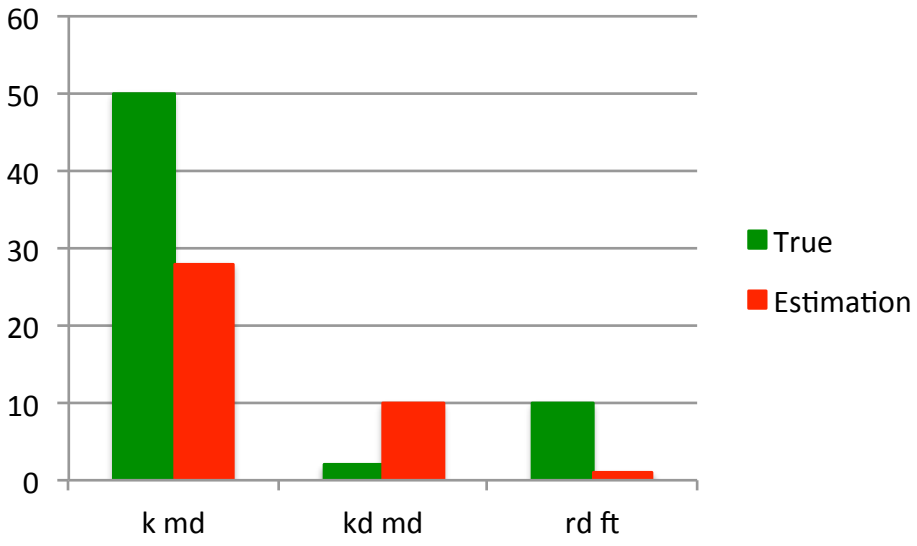

Figure 6.31: Estimation results of case 3-F.1.

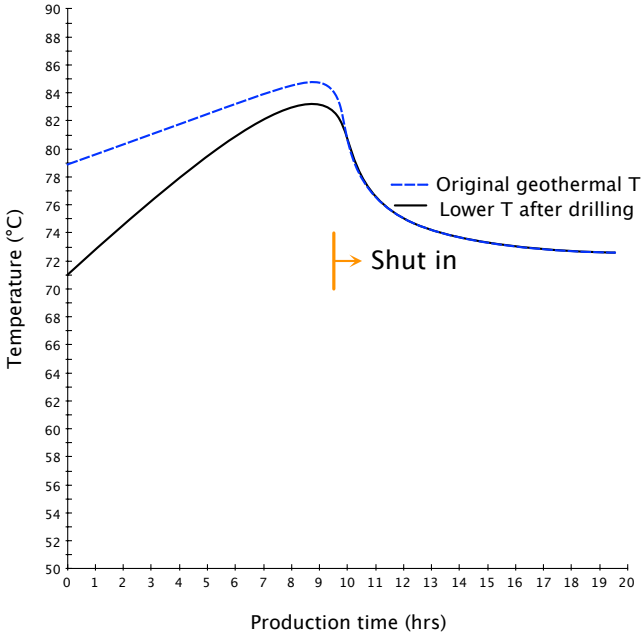

Figure 6.32: The reproduction of temperature history for case 3-F.2.

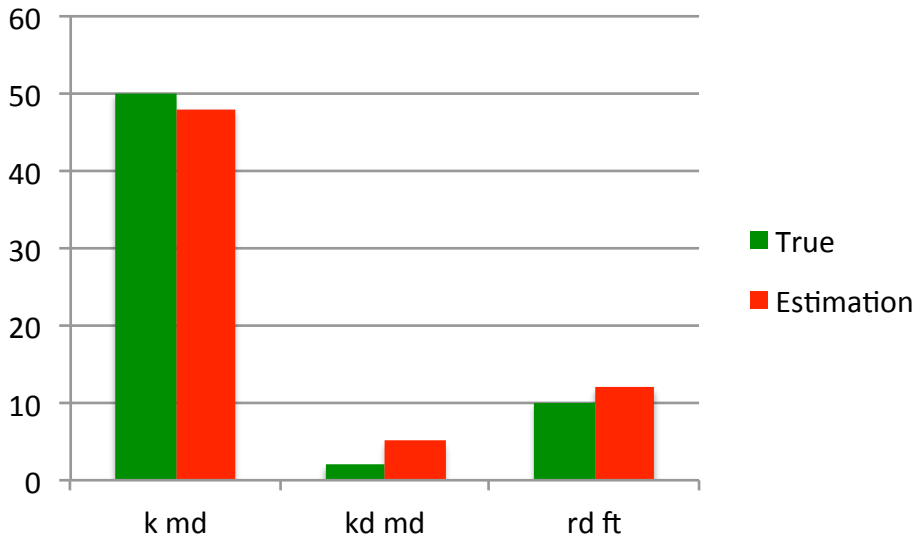

Figure 6.33: Estimation results of case 3-F.2.

near-well damaged zone, other than estimating a skin factor by pressure transient analysis, temperature data give estimations of both the size and permeability of the damaged zone. This information, which is not obtained by pressure transient analysis, is very helpful to better understand the damaged zone and propose plans to improve well productivity.

A numerical ring model was used in this study. Through this model, both radius and permeability of the damaged zone can be defined. In addition, directional skin can be defined by a modified version of this model. The synthetic studies were based on several different production scenarios, concluding that transient temperature data are sensitive to both the size and permeability of the damaged zone, and they can be used to estimate these two parameters, although several cautions should be taken:

1. The gap between the measurement and the entry point affects the estimation. Thus, the correct information of distance of this gap should be obtained, and the flowrate should not be very low if the gap is large. For DTS application, we recommend to run the fiber through the entry point, to prevent the influence of the gap.

2. The temperature data alone are not sufficient to estimate damaged zone properties if the flow becomes multiphase. However, the temperature data can still give a reasonable estimate of undamaged formation permeability.

3. The measured initial temperature might be misleading due to previous drilling or production jobs. A shut-in period and setting the initial temperature as unknown would help to solve this problem.

Chapter 7

Formation Evaluation by Temperature: Multilayer and Horizontal Wells

The discussion of estimating formation properties from temperature is extended to multilayered reservoirs in this chapter. Fiber optic DTS measures multiple downhole points simultaneously, and the distributed data obtained can be used to evaluate the formations properties in multiple layers. Unlike in a single-layer reservoir, fluids in a multilayered reservoir flowing from different layers are mixed in the well, so that the temperature measured in the tubing (T_m) differs from the entry temperature (T_e). We studied the difference between using T_m and T_e to do the estimation. Moreover, multilayered reservoirs are more complicated than single-layer reservoirs in having vertical flows in the reservoir, which adds another unknown (vertical permeability) into the inverse problem.

Horizontal wells were also studied. Similar to the wells in a multilayered reservoir, horizontal wells have multiple entry points, but horizontal wells have a significant difference from vertical wells, making the estimation more difficult. For example, in

horizontal wells, where the horizontal section is penetrating a single layer, all the fluids are flowing from the same depth with the same or similar geothermal temperature. Therefore, the difference between the entry temperature of the fluid from different locations is not prominent. Consequently, it is hard to distinguish individual flows after they mix in the well.

In this chapter, the relevant issues of estimating formation properties in multilayered reservoir and horizontal wells are discussed. Several cases of different production scenarios were studied using synthetic data. Finally, the estimation method was applied to analyze a real data set.

7.1 Multilayered Reservoir Type

According to the hydraulic connections, multilayered reservoirs can be defined into two basic types: commingled and cross-flow. If hydraulic communication only occurs in the wellbore, the reservoir is commingled, otherwise, it is a cross-flow reservoir, as shown in Figure 7.1. Sui et al. (2008) used transient entry temperature profile and total flowrate to achieve a correct estimate of permeability and radius of the damaged zone. But the authors did not study the use of mixing temperature data, and the discussion was limited to commingled reservoirs.

The objective of this study is the same as in the single-layer reservoir (Chapter 6): using temperature to estimate damaged zone properties and formation property. However, multilayered reservoirs are more challenging than single-layer reservoirs. In contrast to a single-layer case, where flowrate can be measured and set to be known in the inverse model, in a multilayered reservoir, only a total flowrate can be measured, while flowrate of each layer is unknown and needs to be estimated. Furthermore, if the reservoir is cross-flow, there is an additional unknown: vertical permeability (k_v).

To build an inverse model, the location of each entry point is known, and the

unknown of each layer for commingled and cross-flow reservoir are listed in Table 7.1.

The ring model introduced in Chapter 6 was used for multilayered reservoir cases, and the damaged zone properties can be defined separately in each individual layer. As described in Chapter 1, the temperature data can be measured from two sources: entry temperature (T_e) if the fiber is cemented behind casing and mixing temperature (T_m) if the fiber is attached to the tubing. We studied whether formation properties can be extracted correctly by using each source separately. Least square method was used to solve the inverse model. Commingled and cross-flow reservoirs are discussed in Section 7.2 and 7.3 respectively.

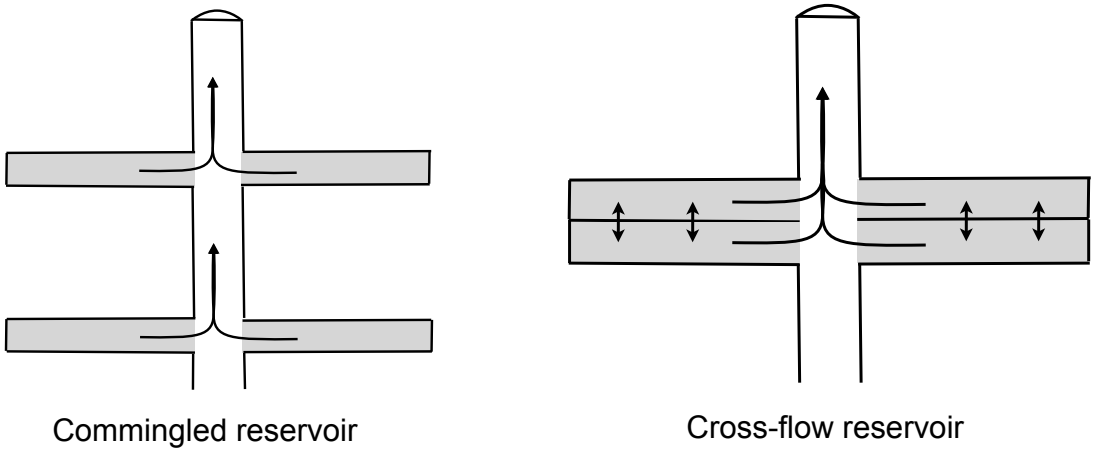

Figure 7.1: Sketch of commingled and cross-flow reservoirs.

Table 7.1: Unknowns for commingled and cross-flow reservoirs

Commingled	$r_d(md)$	$k_d(md)$	$k(md)$	flowrate $q(bbl/day)$	
Cross-flow	$r_d(md)$	$k_d(md)$	$k(md)$	flowrate $q(bbl/day)$	$k_v(md)$

7.2 Commingled Reservoir

Case 4-A.1 is a two-layer commingled reservoir, with layer properties listed in Table 7.2. The two layers are 1000 ft apart, and the simulated temperature profiles of T_m

and T_e are shown in Figure 7.2 and 7.3. As shown in Figure 7.4, by using either T_e or T_m, the estimations are close to true values. This finding coincides with the conclusion in Sui et al. (2008).

However, there is a disadvantage of using T_m to do the estimation: the result depends on the data quality of the whole temperature profile. In other words, noise from each layer will affect the estimation of other layers. As an example, in case 4-A.2, when the lower part of the T_m data were added with white noise with signal-to-noise ratio of 10 dB (Figure 7.5), the estimations of both layers were ruined (Figure 7.6). By contrast, in the same case, the T_e of the lower layer were augmented with noise of 10 dB signal-to-noise ratio, only the estimation of the lower layer properties was distorted, and the estimation of upper layer properties was not affected (Figure 7.7).

Table 7.2: Layer properties for case 4-A.1

	$k(md)$	$k_d(md)$	$r_d(ft)$
Layer 1	50	10	10
Layer 2	100	2	10

After studying case 4-A.1 and 4-A.2, which are based on simple production scenarios, more cases were built to study other relevant issues.

1. Large number of layers

   In case 4-A.3, the number of layers is ten, and the reservoir is commingled. Mixing temperature profile and entry temperature data were used separately to estimate formation properties, and as shown in Table 7.3 (estimation results) and Figure 7.8 (relative errors of estimations), the estimations are acceptable.

2. Distance between different layers

   Mixing temperature profile is influenced by the flow from each layer, so the flow from one layer affects the temperature derivatives of the other. The magnitude

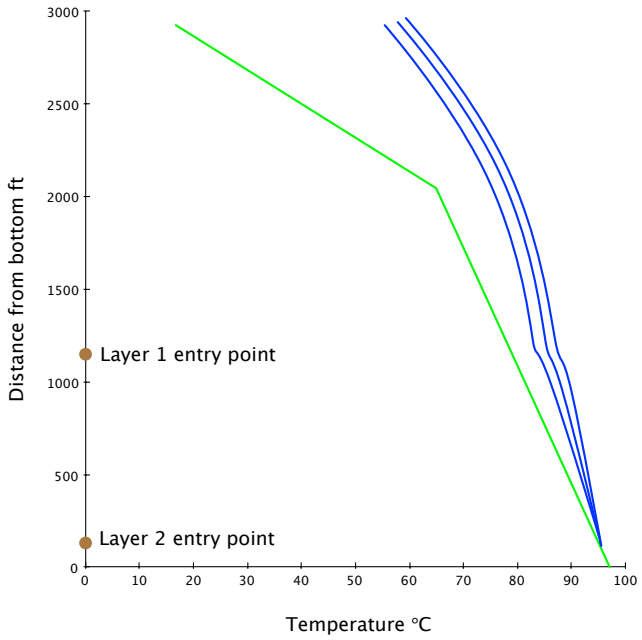

Figure 7.2: Mixing temperatures of two layers for case 4-A.1. (Blue lines are the mixing temperature at different time, while green line is the geothermal temperature.)

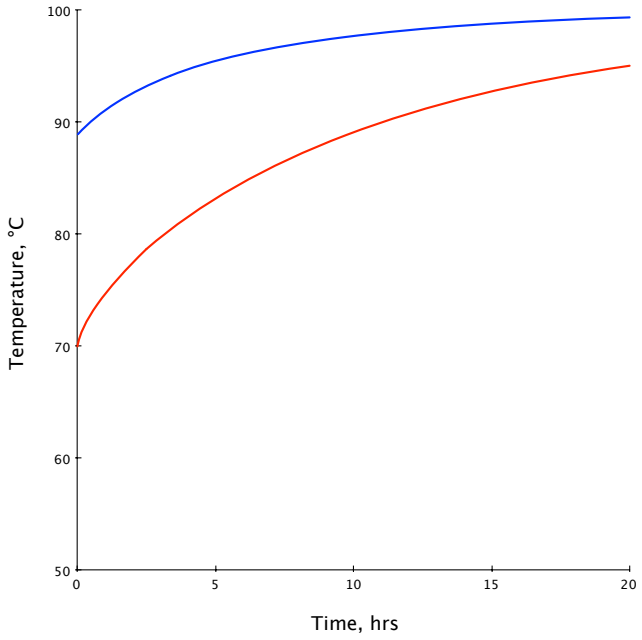

Figure 7.3: Entry temperatures of two layers for case 4-A.1.(Blue line - layer 2; Red line - layer 1)

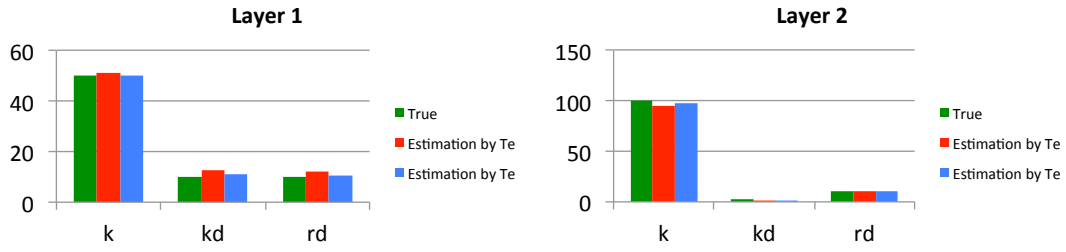

Figure 7.4: Estimation results by using T_m or T_e (Case 4-A.1).

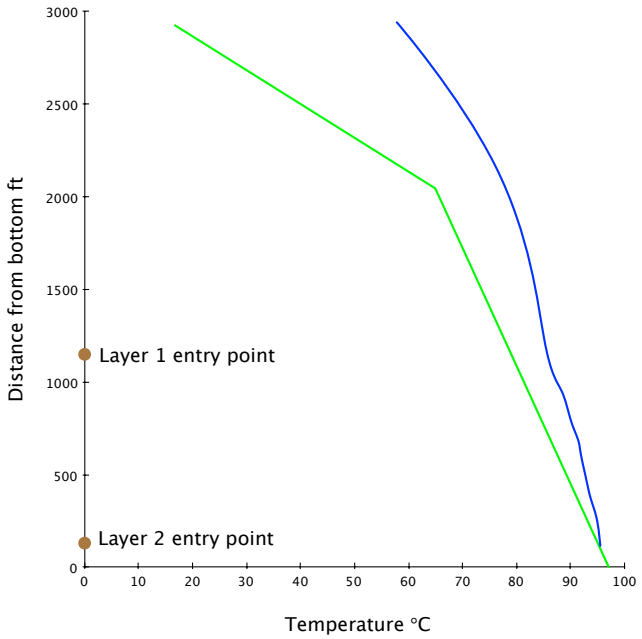

Figure 7.5: Noisy mixing temperature profile, case 4-A.2.

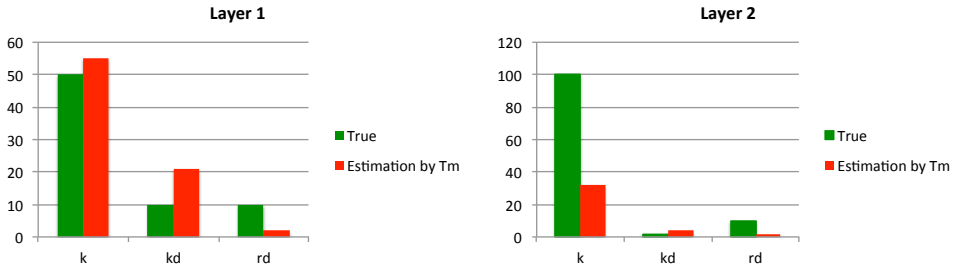

Figure 7.6: Estimation results of using T_m in case 4-A.2.

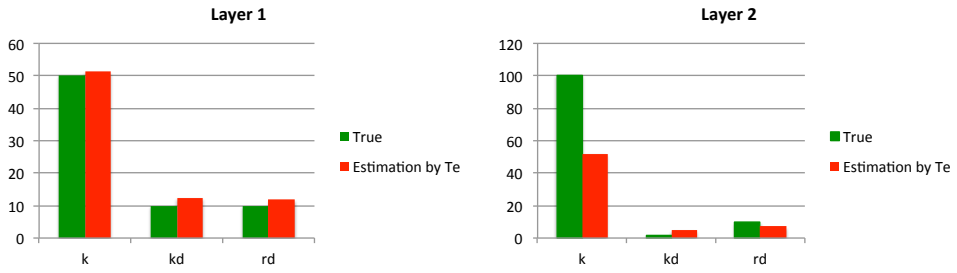

Figure 7.7: Estimation results of using T_e in case 4-A.2.

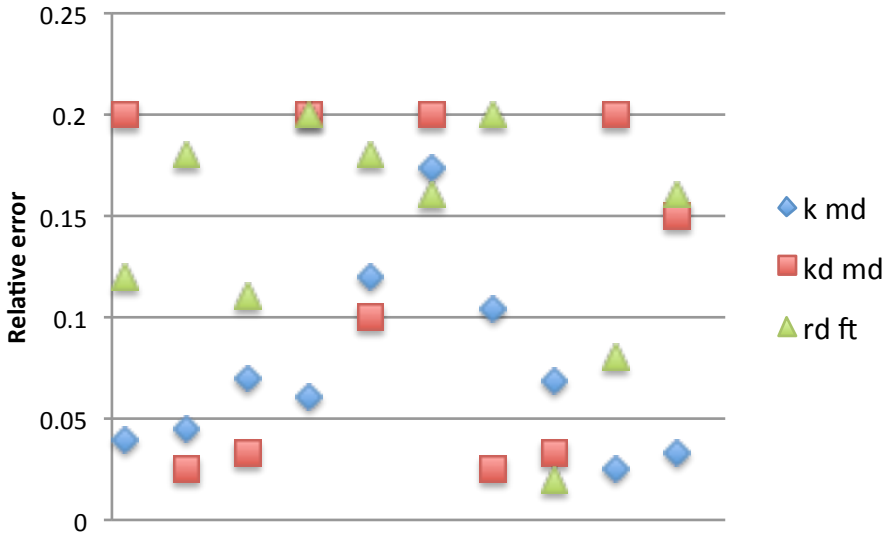

Figure 7.8: Relative errors of the estimation results for case 4-A.3.

Table 7.3: Estimation results for case 4-A.3

Layer 1	$k(md)$	$k_d(md)$	$r_d(ft)$
True	50	2	10
Estimaiton	48.2	1.6	8.8
Layer 2			
True	40	8	10
Estimaiton	38.2	8.2	8.2
Layer 3			
True	30	6	10
Estimaiton	32.1	6.2	8.9
Layer 4			
True	20	4	10
Estimaiton	21.2	3.2	8.0
Layer 5			
True	10	2	10
Estimaiton	8.8	1.8	8.2
Layer 6			
True	15	2	5
Estimaiton	12.4	1.6	4.2
Layer 7			
True	25	8	5
Estimaiton	22.4	8.2	4
Layer 8			
True	35	6	5
Estimaiton	32.6	6.2	4.9
Layer 9			
True	45	4	5
Estimaiton	43.9	3.2	4.6
Layer 10			
True	55	2	5
Estimaiton	53.2	2.3	4.2

of the influence depends on the distance between different layers. As a derivation of case 4-A.1, in case 4-A.4, the distance between two layer was reduced from 1000 ft to 50 ft. Due to the small distance between layers, the shape of the mixing temperature derivatives of layer 1 (upper layer) changes (Figure 7.9). The change of temperature derivative affects the estimation, and the estimation results of layer 1 by using mixing temperature profile is not acceptable (Figure 7.10).

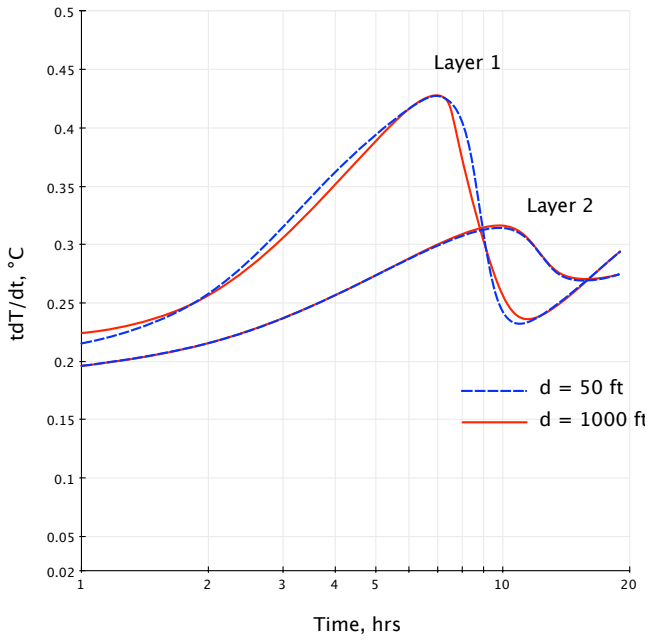

Figure 7.9: Derivatives of T_m for case 4-A.4.

However, the entry temperature (T_e) is not affected by other layers. The estimation of using T_e in case 4-A.4 is still acceptable (Figure 7.11).

3. Property contrast between different layers

   We learned from case 4-A.4 that when using mixing temperature, the influence of one layer on the other should be considered. Besides the distance between layers, the contrast between properties of different layers is also an influential

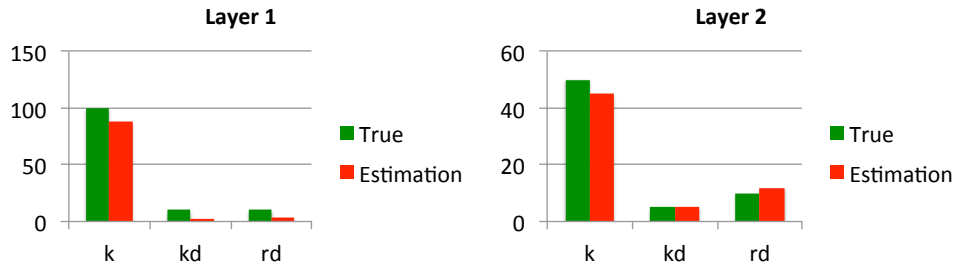

Figure 7.10: Estimation results of using T_m for case 4-A.4.

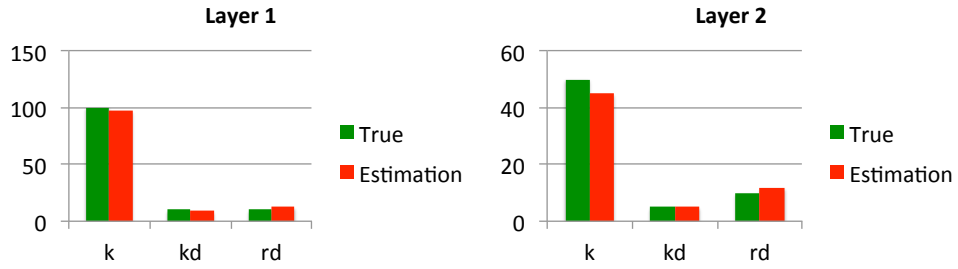

Figure 7.11: Estimation results of using T_e for case 4-A.4.

factor. Unlike the case 4-A.1, in which two layer properties are close to each other, in case 4-A.5, the lower layer has permeability 50 times that of the upper layer, as listed in Table 7.4. By comparing Figure 7.12 and 7.4, the estimation by using mixing temperature in case 4-A.5 is not as good as the results obtained in case 4-A.1.

Table 7.4: Layer properties for case 4-A.5

	$k(md)$	$k_d(md)$	$r_d(ft)$
Layer 1	3	3	10
Layer 2	150	10	10

We also used entry temperature T_e to do the estimation, and the result was improved, as shown in Figure 7.13. This emphasizes the fact that the T_e is less affected by the influence from other layers.

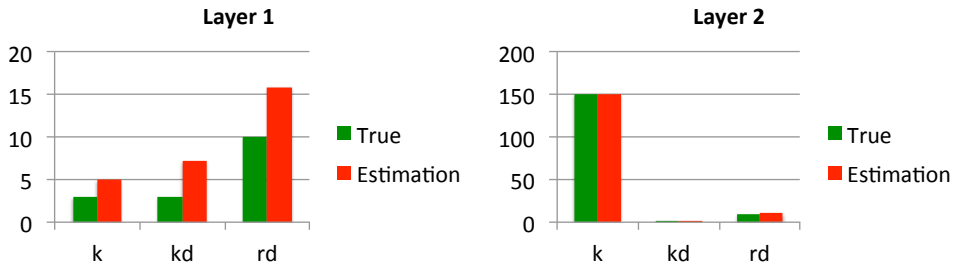

Figure 7.12: Estimation results of using T_m for case 4-A.5.

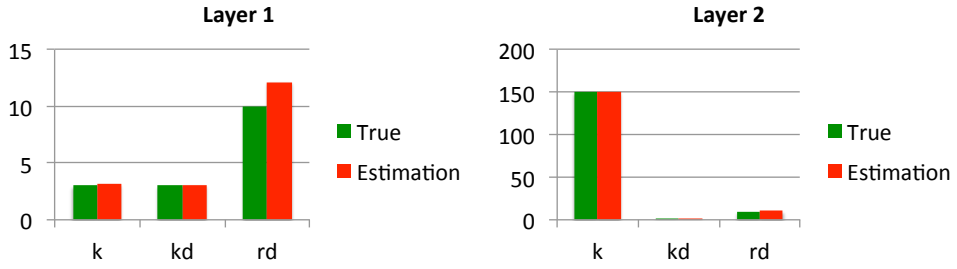

Figure 7.13: Estimation results of using T_e for case 4-A.5.

7.3 Cross-Flow Reservoir

In cross-flow reservoirs, there is vertical flow between different layers due to the property contrast between layers. As mentioned earlier, compared with commingled reservoirs, the inverse problem of cross-flow reservoirs has an additional unknown: vertical permeability.

In case 4-B.1, there are two layers **without** damaged zones. Each layer is homogeneous with horizontal permeability as well as vertical permeability, (Table 7.5). The entry temperature of each layers was used to estimate the formation properties, and the results are close to the true values (Figure 7.14).

Table 7.5: Layer properties for case 4-A.5

	$k(md)$	$k_v(md)$
Layer 1	100	10
Layer 2	50	10

Figure 7.14: Estimation result of case 4-B.1.

However, if the two layers have damaged zones, and the properties of the damaged zone are set as unknowns (case 4-B.2), the estimations by using entry temperature are shown in Figure 7.15. Although the formation permeabilities (k) of both layers are inverted correctly, the estimation results of k_v, k_d and r_d of both layers are not acceptable. If we examine the flow path in the reservoir (Figure 7.16), we find that most cross-layer flow occurs in the near-wellbore region, which means the effect of cross-flow is mixed with the effect of the damaged zone, which cannot be separated by inversion of the temperature data. Pressure data are not helpful for this problem. We have tried to add transient pressure data and distributed pressure data, but the estimation was not improved. To solve this problem, information about the formation properties is more helpful. For example, if the vertical permeability is known, the estimation result by entry temperature for case 4-B.2 become much better (Figure 7.17).

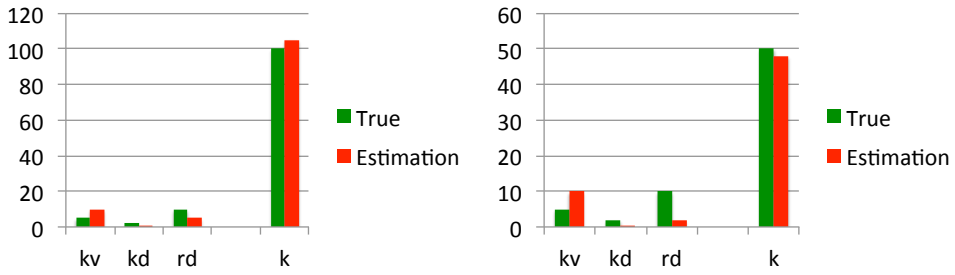

Figure 7.15: Estimation results of case 4-B.2.

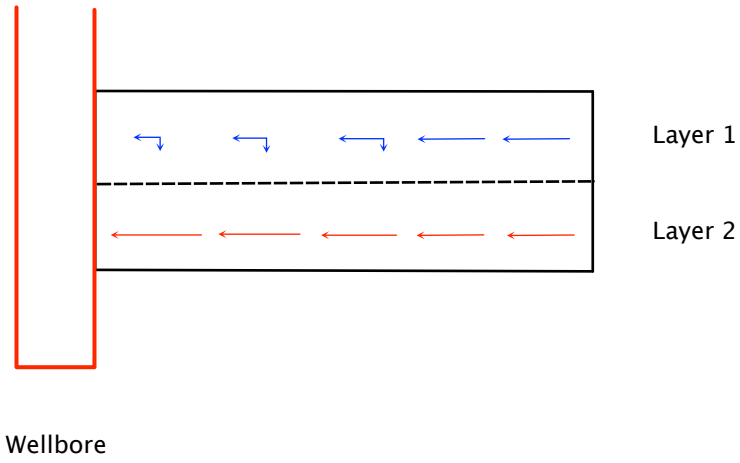

Figure 7.16: The flow path in case 4-B.2.

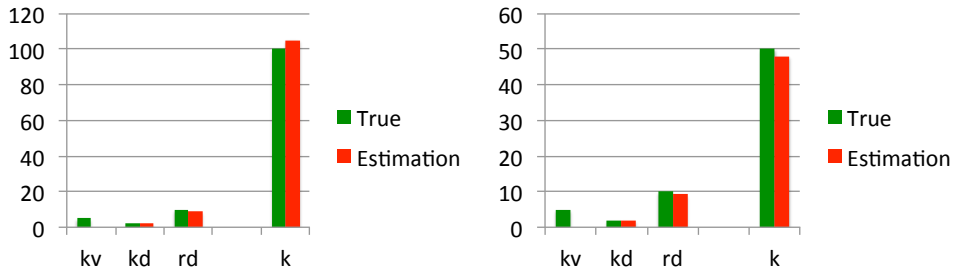

Figure 7.17: Estimation results of case 4-B.2, where k_v is known.

7.4 DTS Application in Horizontal Wells

The idea of horizontal wells is to drill a well deviated from vertical by more than 80 degrees (as shown in Figure 7.18). Through this approach, the contact area between wellbore and reservoir is maximized, and horizontal wells usually deliver much higher productivity than vertical wells.

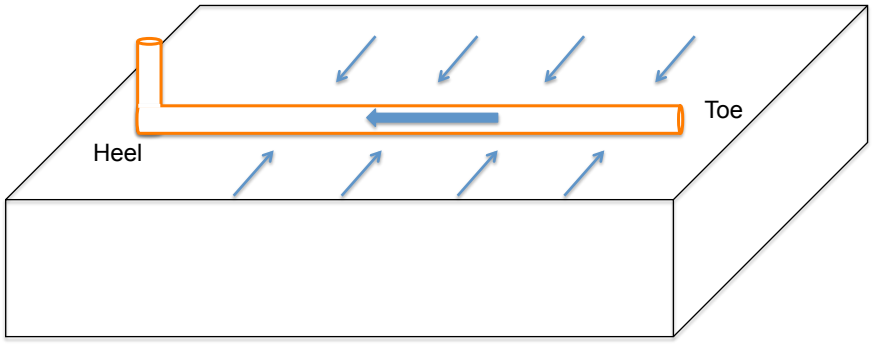

Figure 7.18: A sketch of a horizontal well.

However, the trajectory of horizontal wells makes it extremely difficult to run production measurement tools in the horizontal part. Considering that the length of a typical horizontal well can be thousands of feet, the flow along this length is inhomogeneous, and it is important to monitor the production status along the whole horizontal part for the purpose of optimizing production and identifying flow problems. The small size of optical fiber makes it feasible for measuring temperature profiles along the horizontal part. Several studies have been done to analyze temperature data in horizontal wells. For example, Yoshioka (2005) was successful in using entry temperature profile to estimate flowrate profile in a horizontal well. Based on the same model used by Yoshioka, Li (2010) achieved permeability distributions by using transient entry temperature profiles in a horizontal well. These publications stated that the flowrate profile and permeability distribution can be estimated by entry temperature profiles, but they did not try to use mixing temperature to do the

inversion. In our study, entry and mixing temperature profiles of horizontal wells were studied separately to invert information of flowrate profiles and formation properties. The first step of this study was to build a horizontal well flow model, which is described in the next section.

7.5 Horizontal Well Modeling

The control equations for horizontal wells are the same as the ones we used in vertical wells, and the mass balance and energy balance equations for wellbore and reservoir are the same as we discussed in Chapter 4. The difference from vertical well models comes from the pressure drop equation in wells. We used the homogenous model developed by Ouyang (2005):

$$\frac{dp}{ds} = \frac{32\rho Q^2 I_D}{\pi^2}[\frac{f_c}{D^5}] \tag{7.1}$$

where D is the wellbore internal diameter, f_c is the Fanning friction factor for fluid flow in a circular pipe, I_D is flow direction index, +1 for a production well and -1 for a injection well, s is the position of the measurement in the well.

The reservoir is discretized by single stack of cells. Figure 7.19 is a top-view of a horizontal well penetrating the whole reservoir. The reservoir consists of five layers. These layers might have different permeability values. In the reservoir, we assumed there is no cross flow between different layers and no vertical flows.

We used a synthetic case (case 5-A.1) to show the behavior of this numerical model. In this case, a horizontal well was producing from an oil-saturated reservoir, and the pressure was kept above saturation pressure. The horizontal section of the well is 3000 ft, and all its length is open to flow. The reservoir has five layers, sharing the same width (600 ft). The permeability distribution of reservoir is shown in Figure 7.20. The input parameters are summarized in Table 7.6. The total flowrate is controlled

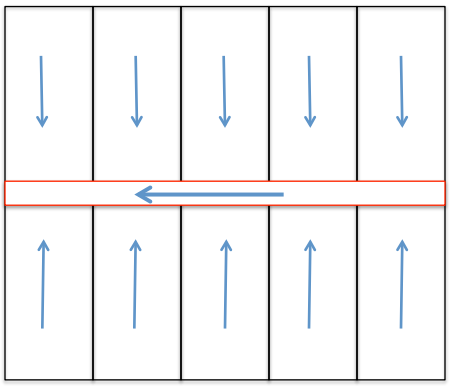

Figure 7.19: A top view of the flow direction in a horizontal well.

as 10,000 bbl/day. The simulation results of flowrate profile, pressure profiles, mixing temperature profiles and transient entry temperature for individual layers are shown in Figure 7.21, 7.22 and 7.23. The analysis of these data will be discussed in Section 7.6.

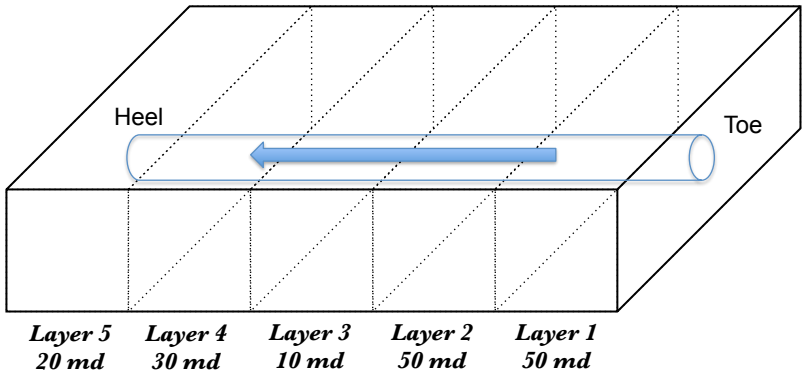

Figure 7.20: Permeability distribution of case 5-A.1.

7.6 Inverse Model and Results

In the inverse model, the data are the temperature profiles. Similar to vertical wells, in horizontal wells the temperature profiles measured downhole could also be mixing temperature (T_m) or entry temperature (T_e). The unknowns are the permeability of

Table 7.6: Input parameters for case 5-A.1

Fluid	
$\mu(cp)$	0.6
$C_p(Btu/lb\cdot^o F)$	0.6
$\rho(lb/ft^3)$	43
Reservoir	
Reservoir length(ft)	3000
Reservoir width(ft)	1000
Reservoir highth(ft)	500
Well	
Well diameter (inch)	2.8
Relative roughness	0.01

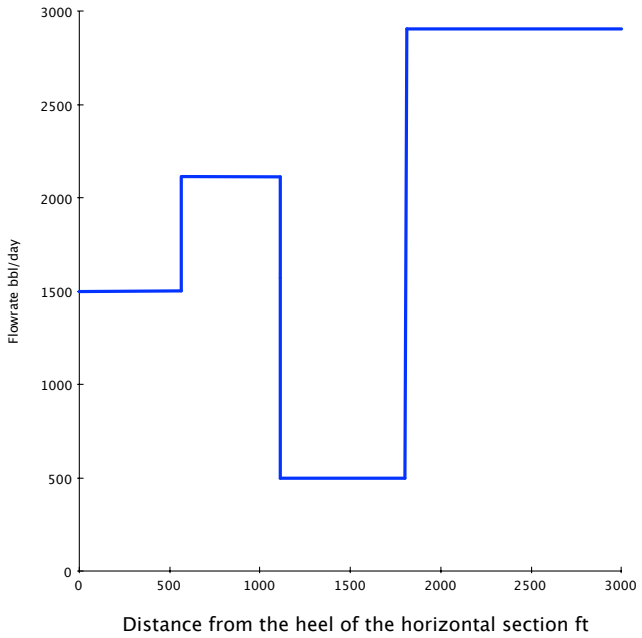

Figure 7.21: Simulation result of flowrate profile for case 5-A.1.

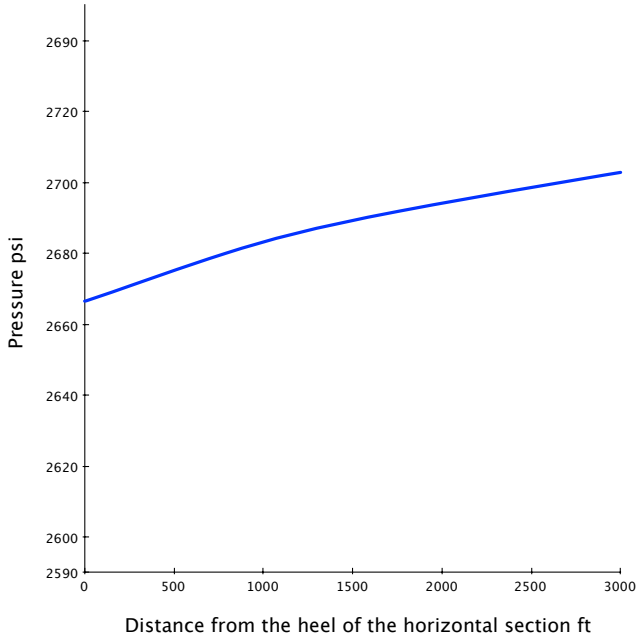

Figure 7.22: Simulation result of pressure profile for case 5-A.1.

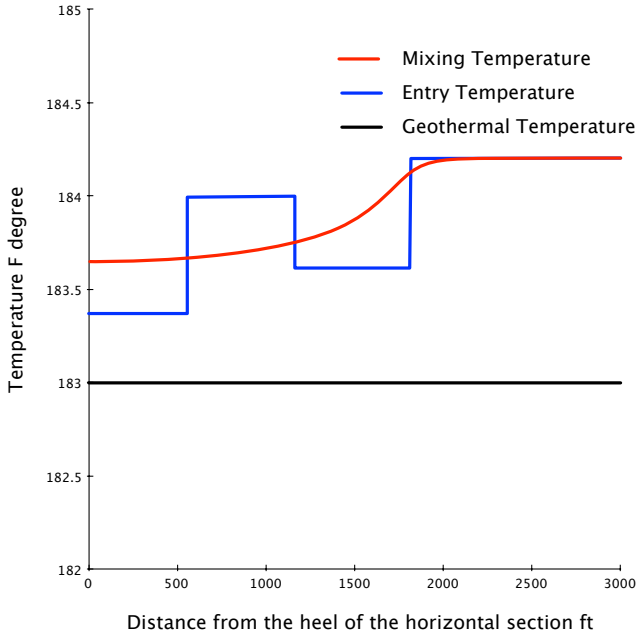

Figure 7.23: Simulation result temperature profiles for case 5-A.1.

each layer and the flowrate profile in the wellbore. The location of each entry point is known, and this inverse problem is again solved by the Least-Square method.

7.6.1 Estimation Only by Using T_m

The mixing temperature profiles simulated in case 5-A.1 (Figure 7.23) were used to estimate flowrate profile and formation properties. Compared to vertical wells, the fluids entering the horizontal wells are from the same depth, sharing the same geothermal temperature. Therefore, the difference between the entering fluid temperature and the mixing fluid temperature is mainly due to the viscous dissipation and adiabatic expansion, so the magnitude of the temperature difference depends largely on the flowrate and formation permeability.

In case 5-A.1, when the transient mixing temperature profiles were used to invert formation properties, the results were not accurate (Figure 7.24). We notice that in this case, the layers 3, 4 and 5 have smaller permeability values than layers 1 and 2 (Figure 7.20). A consequence of this permeability distribution is that the temperature in the well is decreasing monotonically towards the well heel. Because the temperature in the well is higher than its surrounding formation temperature in this case, the fluid is constantly losing heat when it is flowing from the toe to the heel of the well. Even though there is no cold fluid entering the well in the downstream, the temperate will still decrease because of the heat loss. A comparison of the mixing temperature profile of case 5-A.1 and a case where layers 3, 4 and 5 have no flow is shown in Figure 7.25. No significant difference was observed. Therefore, the mixing temperature is not a sensitive indicator for cases having a declining (towards the well heel) permeability distribution.

However, in case 5-A.2 the permeability is increasing monotonically towards the heel of horizontal well, as shown in Table 7.7. The estimated formation properties are close to the true values (Figure 7.26).

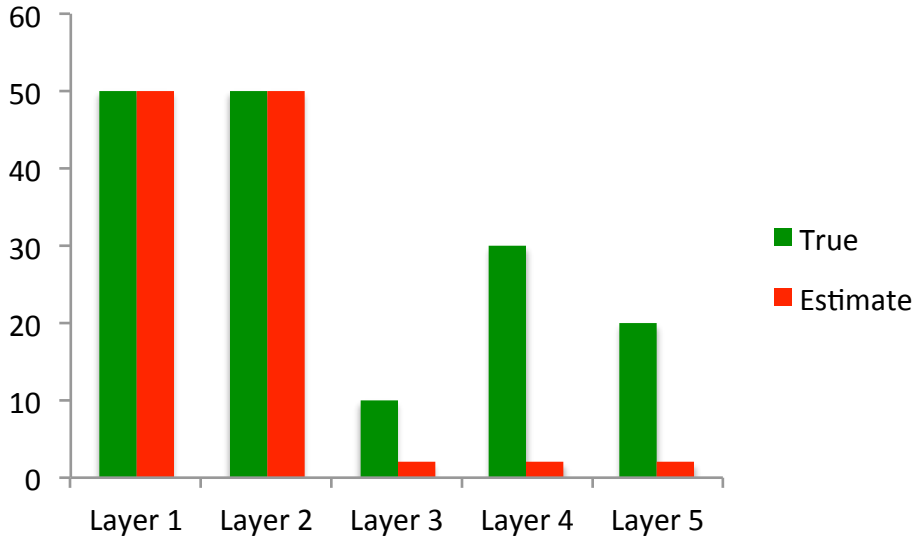

Figure 7.24: Estimation results of using T_m for case 5-A.1.

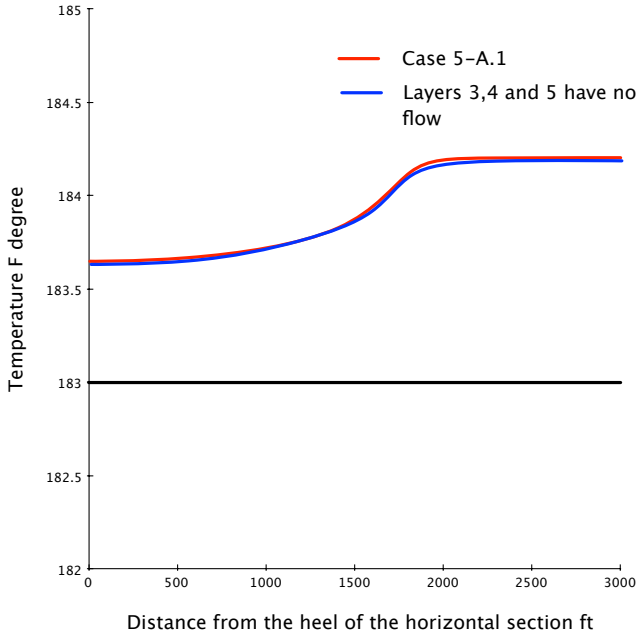

Figure 7.25: Temperature profiles when layers 3, 4 and 5 have no flow.

Table 7.7: Layer properties for case 5-A.2

Layer 1	30 md
Layer 2	40 md
Layer 3	60 md
Layer 4	80 md
Layer 5	100 md

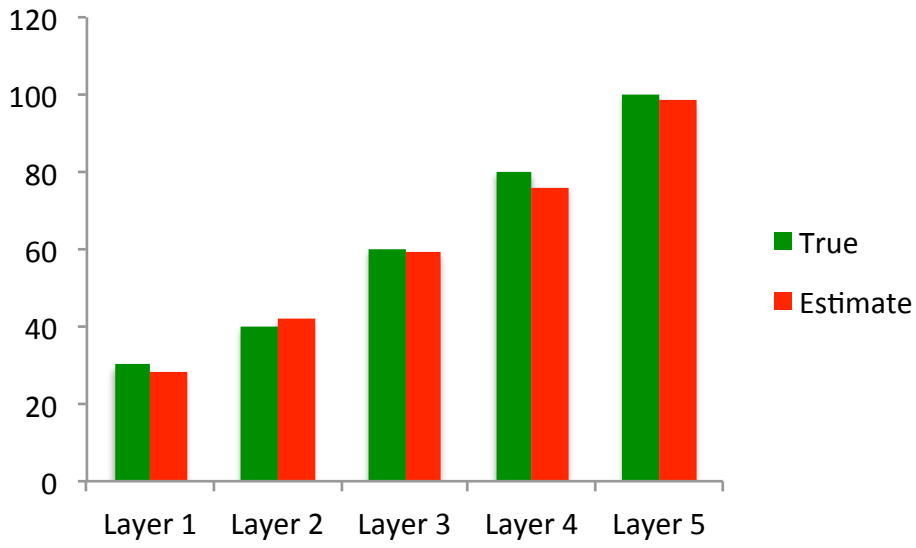

Figure 7.26: Estimation result of using T_m for case 5-A.2.

Through case 5-A.1 and 5-A.2, we learned that the permeability distribution is important for the success of inverting formation permeability using mixing-temperature profile. A successful estimation can be achieved in the case where permeability is increasing towards the toe of the well, whereas it is difficult to invert formation correctly in other cases. Therefore, a subsequent measurement procedure is proposed for general application of this study. For example, in case 5-A.1, the in flow control valve in layer 1 (named as valve 1) is opened first, the permeability of layer 1 can be estimated by measuring the temperature and the flowrate. Then the valves 2, 3, 4 and 5 are opened subsequently to obtain the mixing temperature profiles shown in Figure 7.27. By using these temperature profiles, the permeability of all the layers can be estimated correctly (Figure 7.28).

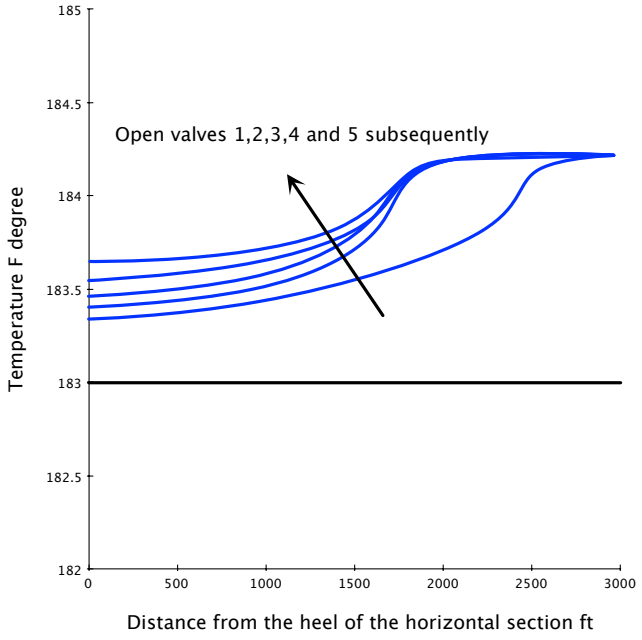

Figure 7.27: Sequential temperature profiles for case 5-A.1.

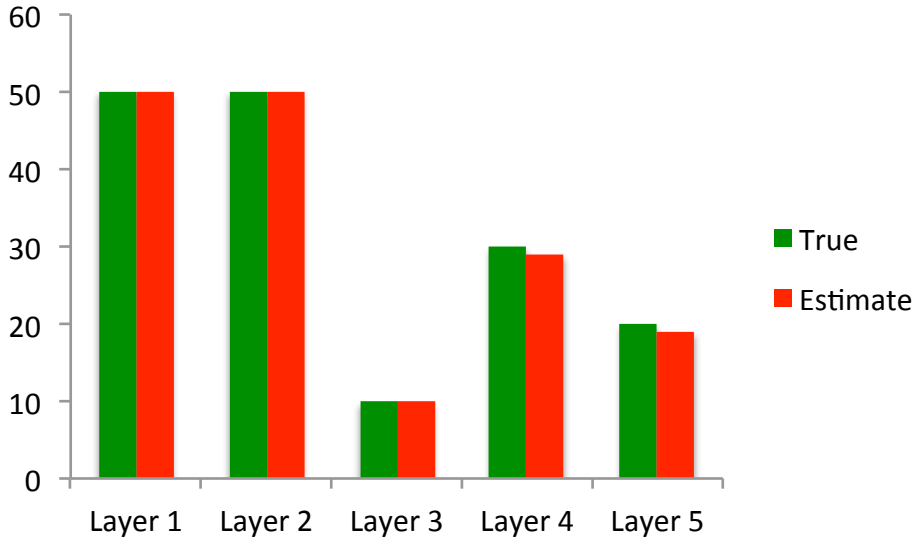

Figure 7.28: Estimation results of using sequential temperature profiles for case 5-A.1.

7.6.2 Estimation Only by Using T_e

Similar to the multilayered reservoir cases discussed in Section 7.2, entry temperature of each layer is not influenced by other layers in vertical wells. This is also true for horizontal wells. In case 5-A.1, when the transient entry temperature (Figure 7.23) in each layer is used, the estimations of permeability are acceptable (Figure 7.29).

The cases of 5-B.1 to 5-B.4 have different permeability distributions. Using entry temperature, layer permeabilities can be estimated correctly in all these cases, as shown in Figure 7.30 to 7.33. Again, this confirms the statement that using entry temperature to invert formation properties is not constrained to permeability distribution. This also coincides with the findings of Li (2011).

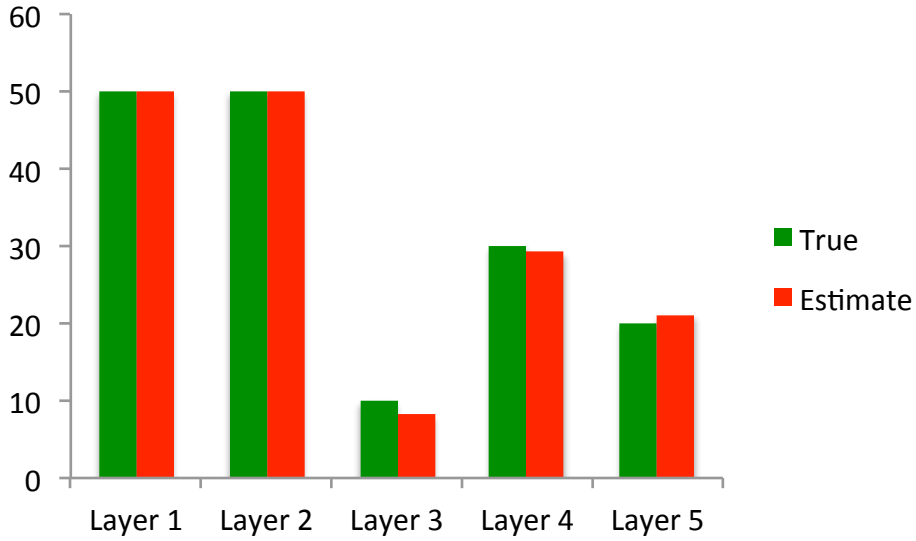

Figure 7.29: Estimation results of using T_e for case 5-A.1.

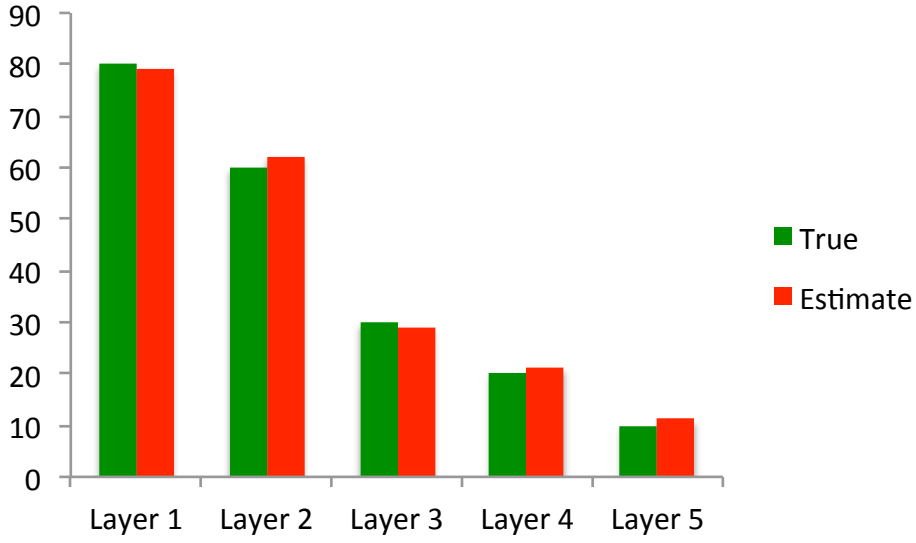

Figure 7.30: Estimation results of using T_e for case 5-B.1.

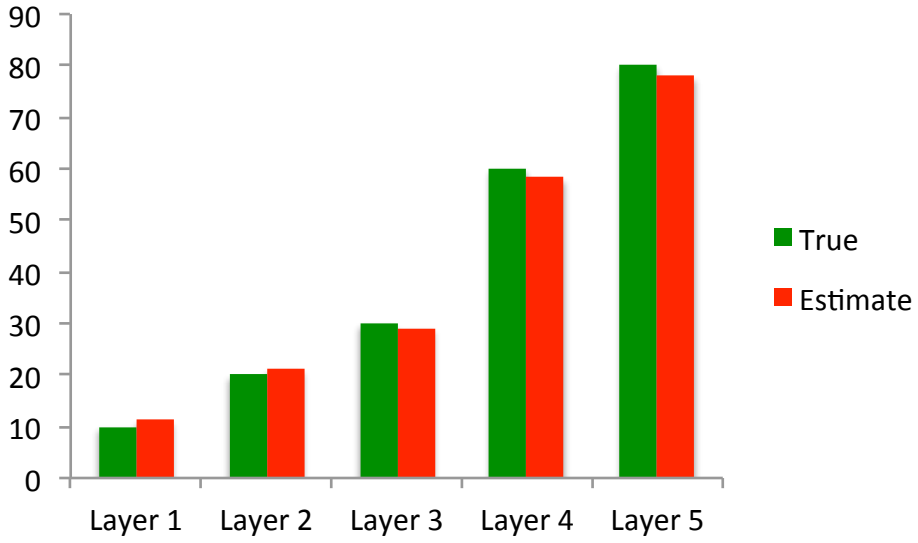

Figure 7.31: Estimation results of using T_m for case 5-B.2.

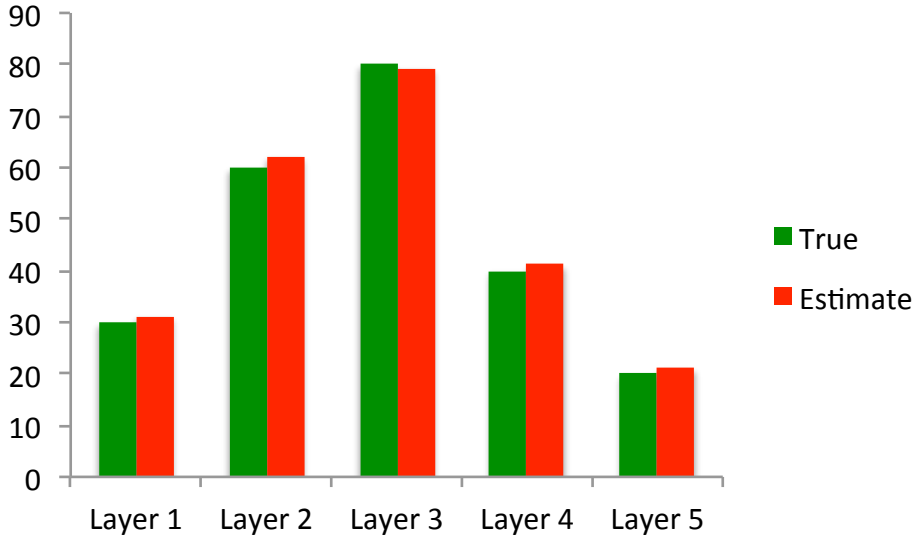

Figure 7.32: Estimation results of using T_m for case 5-B.3.

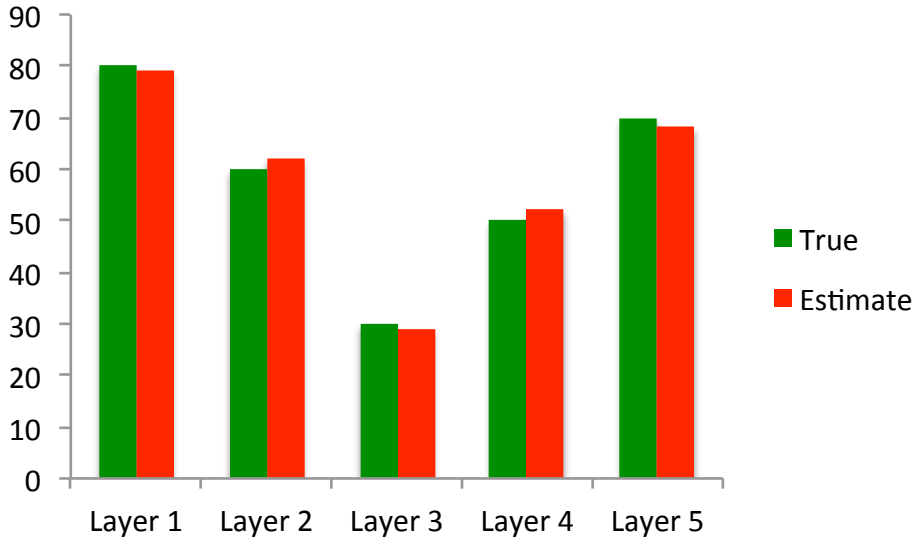

Figure 7.33: Estimation results of using T_m for case 5-B.4.

7.7 Real Cases

The real DTS data set we studied is from an oil producer. The well was producing from three layers. The DTS was installed on the sand-screening. This installation method was shown in Figure 1.3 of Chapter 1. As discussed, the measurement made by this installation method is twofold: it measures entry temperature when there is fluid flowing from the reservoir (in the production layer), or mixing temperature otherwise. This is illustrated by Figure 7.34.

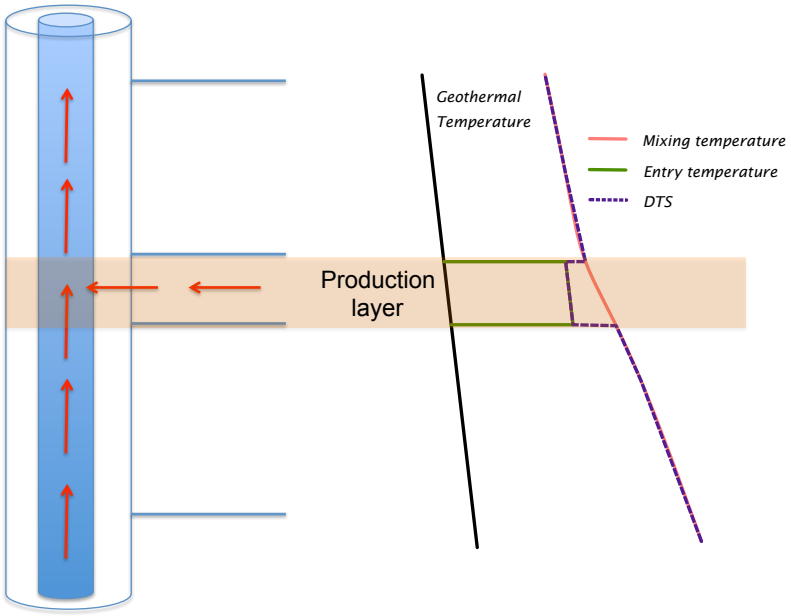

Figure 7.34: A sketch of DTS data in the real case.

The data available to us are 12 hour-DTS data, which were measured when the well was first put into production. The total flowrate at the wellhead during this 12-hour production was kept as constant at 7592 bbl/day. The data are shown in Figure 7.35. From the data, the three production layers are shown clearly: the temperature dipped where the flow enters the well. We also calculated the derivative of entry temperature in each layer, which is shown in Figure 7.36. The early parts of all these derivatives are too noisy to reveal any trend. In contrast, in the late part of the

derivative, the derivative bears a certain pattern of behavior, which will be indicative of the far-well formation properties.

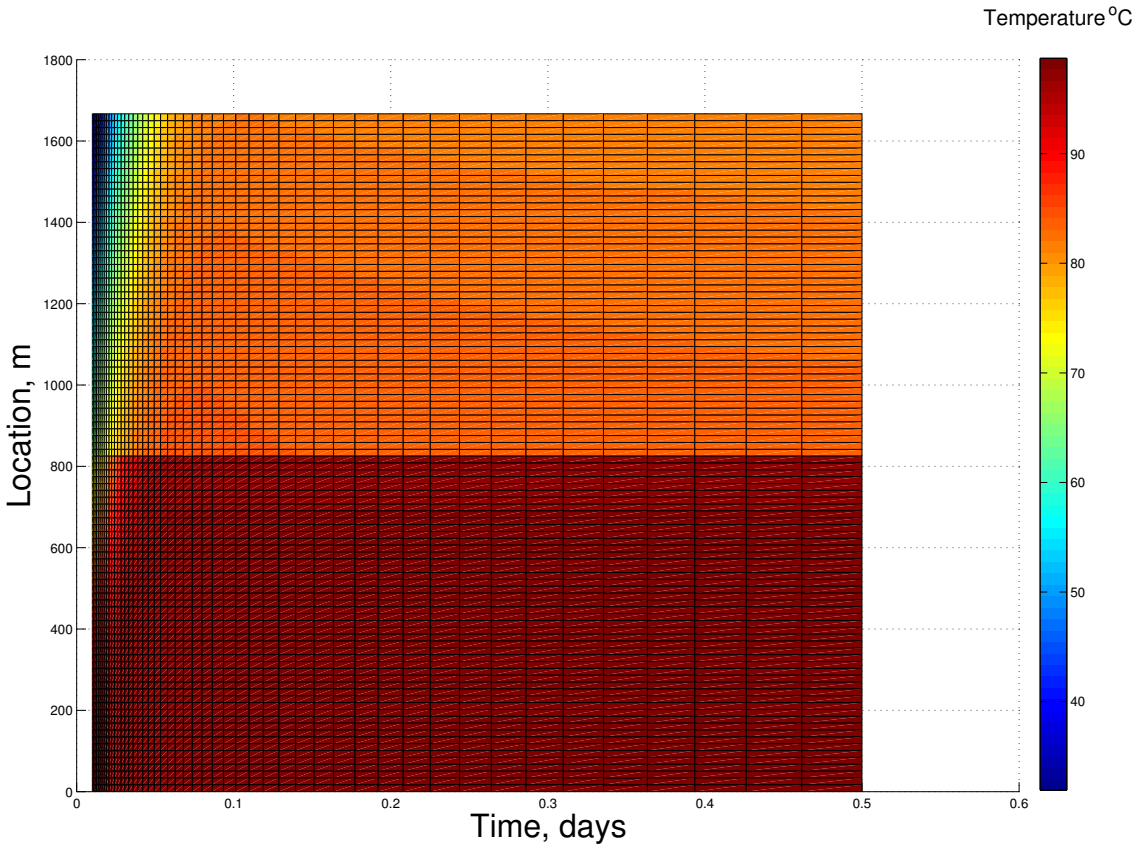

Figure 7.35: DTS data.

We used the ring model and least-square method to analyze the DTS history. The estimation results include radius and permeability of damaged zone and permeability of undamaged zone for all three layers, and flowrate profile history. All these results are listed in Table 7.8, and the model can reproduce the DTS data closely (Figure 7.37).

The flowrate profile cannot be measured directly from the well, and thus the estimated flowrate cannot be verified. However, a comparison between the total

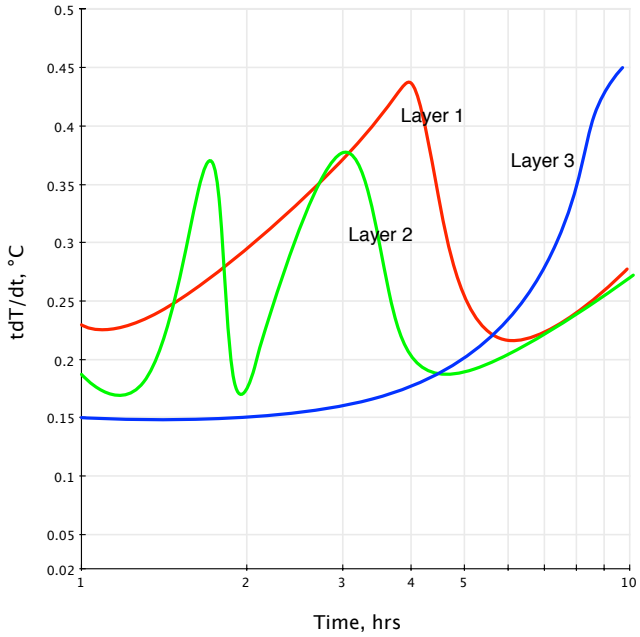

Figure 7.36: Temperature derivatives for three layers.

Table 7.8: Estimation results for the real data set.

Layer 1	
k	59.2 md
r_d	3.2 ft
k_d	7.1 md
Layer 2	
k	30.3 md
r_d	2.1 ft
k_d	6.2 md
Layer 3	
k	25.5 md
r_d	3.2 ft
k_d	5.3 md

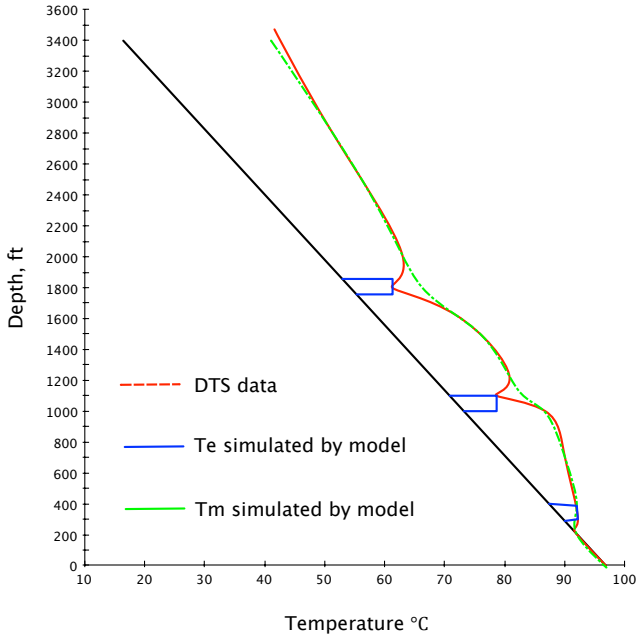

Figure 7.37: The reproduction of DTS data.

permeability obtained from analyzing the wellhead transient pressure data and the height-weighted mean of the estimated permeability can help to validate the estimation. As shown in Figure 7.38, the values are close to each other.

7.8 Summary

In this chapter, the discussion of evaluating formation properties was extended to multilayered reservoirs and horizontal wells, both having multiple entry points in the well. This research work took advantage of DTS, using the distributed temperature data obtained from DTS to evaluate formation properties along the whole well length simultaneously. An important issue is the installation method of the fiber. Different installation methods give different measured temperature profiles. If only mixing temperature is obtained, the influence between different layers should be taken into consideration when doing the estimation. For example, a pair of close-by layers, or

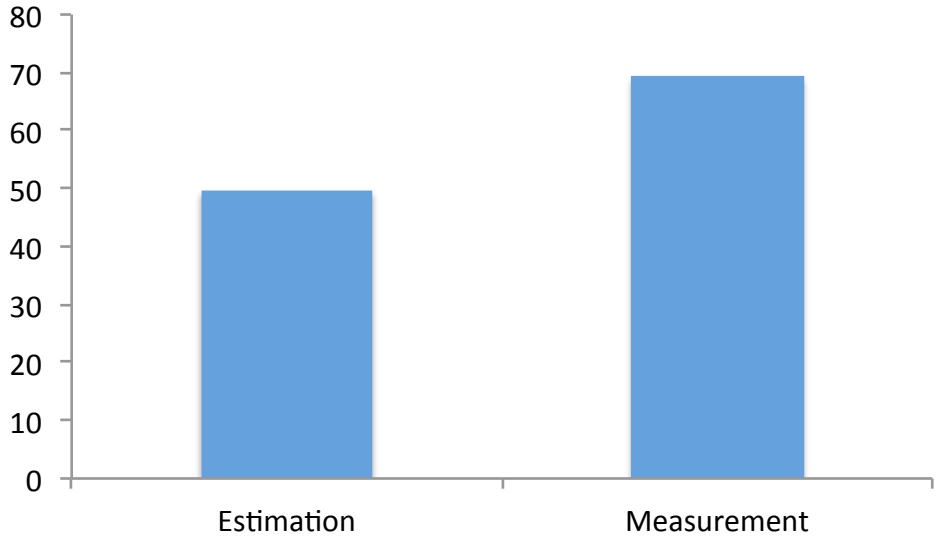

Figure 7.38: Comparison of the hight-weighted mean of permeability.

layers with huge properties contrast would ruin the estimation made by using mixing temperature. However, the entry temperature is not influenced by other layers if no leakage happens in the cement, so the estimation by using entry temperature is better than mixing temperature in numerous vertical cases we studied.

Chapter 8

Conclusions and Recommendations for Future Work

In this research, the downhole temperature behavior was studied in three subsequent respects.

1. A numerical wellbore/reservoir coupled thermal model was built to study which parameters are important in determine the downhole temperature distribution. Through the synthetic study using this model, we found that temperature in the wellbore is largely influenced by fluid Joule-Thomson coefficient, flowrate and formation permeability. Also, we concluded that a compositional model is necessary for analyzing DTS data from complicated flows, e.g. multiphase flow.

2. We showed that flowrate can be estimated from temperature data. In our study, both least-square method and linear inverse model were applied to solve the inverse problem. As discussed in this dissertation, the success of least-square method relies on the knowledge of the number and locations of each entry point. By contrast, linear inverse model can invert flowrate profile from temperature profile correctly without knowing the entry points number and locations.

This research result makes the concept of 'soft-sensor' for monitoring flowrate more realistic and achievable.

3. Temperature can also be very informative about formation properties, and it is even better than pressure transient analysis in evaluating near-well damaged zones.

The result of this study makes the downhole temperature data more useful to understanding well perforation and reservoir characters. However, there are still large spaces for better use of DTS data. Two directions are suggested for future research work.

1. Apply Vertical Temperature Data to Reservoir Characterization

   The reservoir characterization process is to build a geological reservoir model by incorporating as many field data as possible. Well logs, seismic and production data are the three main sources of data. A workflow of reservoir characterization can be illustrated in Figure 8.1. First, a lithofacies model is built by integrating well logging data and seismic data, and then a petrophysical model is generated based on the lithofacies model. Thus, this petrophyisical model is conditioned to the geological prior information and the seismic/well logging data. Subsequently, by doing history matching, the petrophysical model is conditioned to production data. Finally, an optimized geological model is obtained.

   The incorporation of DTS data to reservoir characterization workflow is promising because DTS has the following advantages:

   (a) It has high vertical resolution, and the flowrate profile can be estimated from the DTS. Therefore, comparing to the traditional single-point production data (no matter whether the production is measured on the surface or downhole), DTS can provide more information in the vertical direction.

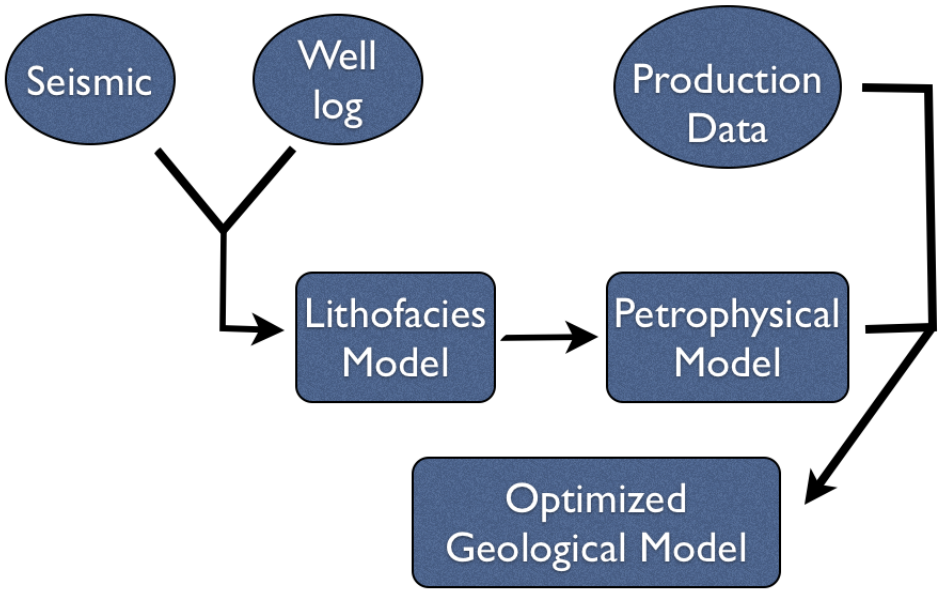

Figure 8.1: Flowchart of reservoir characterization.

This vertical production information can be used to constrain geostatistical realizations. Thus, DTS is valuable to study the **vertical heterogeneity** in the reservoir.

(b) DTS can provide information continuously during the production, and thus it might be incorporated with 4D seismic data to capture the temporal reservoir changes.

(c) The estimate of permeability from the temperature profile is more reliable than from seismic or well logging data, because temperature is dynamic data, while seismic or well log are static data. Permeability is a parameter used to characterize dynamic flowing, so in order to estimate permeability from seismic or well logging data, an empirical relationship between porosity and permeability has to be used. However, the temperature is related directly with permeability. Thus, it is promising to use the temperature to estimate permeability field.

2. Interpret DTS Data in an Interference Test

   As the heat diffuses very slowly in the reservoir, the DTS data in a single well can only provide information in the near-wellbore region, and this region is usually contaminated by the drilling operation and is not representative of the whole formation. By contrast, in an interference test, temperature may be recorded in an observation well at a distance away from the active well. The time of water (or gas) breakthrough and sequence of water breakthrough in each layer provides information of the layer permeability. DTS can monitor wellbore production continuously, and sensitive to water (or gas) breakthrough.

Nomenclature

C_0	distribution coefficient in the drift-flux model, dimensionless
f	fugacity
g	gravity component along the well, ft/sec^2
H_p	specific enthalpy of phase p, btu/lbm
k	permeability, md
K_c	equilibrium ratio
m_{cp}	mass source/sink term for component c in phase p, lbm/day
m_H	thermal source/sink term, $btu/day \cdot ft$
N_c	number of component
N_s	number of well segments
p_p	wellbore pressure, psi
Q_{loss}	heat loss to the surroundings, $btu/day.ft$
r_{in}	internal radius of the well, ft
S_p	saturation of phase p

t	time, $days$
T	reservoir temperature, ^oF
T_w	wellbore temperature, ^oF
U_p	specific internal energy of phase p, btu/lbm
U_{to}	overall heat transfer coefficient, $btu/day \cdot ft^2 \cdot^o F$
V_d	drift velocity of gas in liquid, ft/sec
V_m	mixture velocity, ft/sec
V_p	velocity of phase p, ft/sec
V_{sp}	superficial velocity of phase p, ft/sec
WI	well index, $cp \cdot b/day \cdot psi$
Z_c	overall mole fraction of component c
α_p	in-situ volume fraction of phase p
β	thermal expansion coefficient? $1/K$
x_{cp}	molar fraction of component c in phase p
λ_p	mobility of phase p, $ft^2/cp \cdot rb$
ρ_p	density of phase p, lbm/ft^3
z	mole fraction of gas in absence of water

Subscripts

a	acceleration

c	component
f	frictional
h	hydrostatic
p	phase
s	superficial
r, z	spatial directions

Appendix A

Structural Parameter Selection

Continuing from the discussion in Chapter 3 about the linear inverse model, the prior of s($\mathbf{x}$) is a Gaussian random field, and its covariance matrix is Q. The measurement equation is:

$$y = Hs + v \tag{A.1}$$

in which v is the error term with mean 0 and covariance R.

In the case that Q and R have linear generalized covariance function, they can be written as:

$$Q_{i,j} = -\theta_1 |x_i - x_j|, \theta_1 > 0 \tag{A.2}$$

$$R_{i,j} = \theta_2 \delta_{i,j}, \theta_2 > 0 \tag{A.3}$$

θ_1 and θ_2 are the parameter we need to choose. According to Kitanidis (2007), these structural parameters have the following characters:

1. a large θ_1 would replicate data more closely, while leading to more fluctuation in the estimation, thus θ_1 has the effect of suppressing fluctuations in the estimate at the expense of sacrificing some of the resolution;

2. a large θ_2 smooths the estimates and yields an estimate that reproduces the

data less faithfully.

One may need to select these two parameters, not only by previous experience, which is subjective, but also under the guidance of the data. This is the problem of **structural-parameters estimation**. The detail of the choosing structural parameters when applying linear inverse model to Case 2-A.1 (Chapter 5) are shown in the following.

At optimum, Q_2 should be equal to 1, from Figure A.1, when Q_2 equals 1, θ_2 is 6.1×10^{-4}; and we want to minimize cR by varying θ_1/θ_2, as shown in Figure A.2, $\theta_1/\theta_2 = 0.0167$ minimizes cR, thus, θ_1 is 10^{-5}.

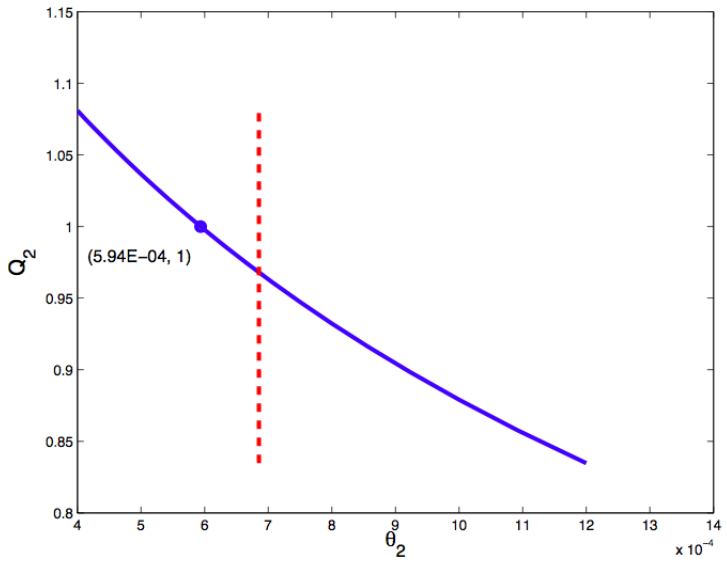

Figure A.1: Q_2 vs θ_2.

One way of convincing that our estimation of θ is reasonable is to show we achieve a good trade-off between data fitting and resolution. The degree of meeting these conflicting objectives can be measured through J_r and J_f, which are defined as:

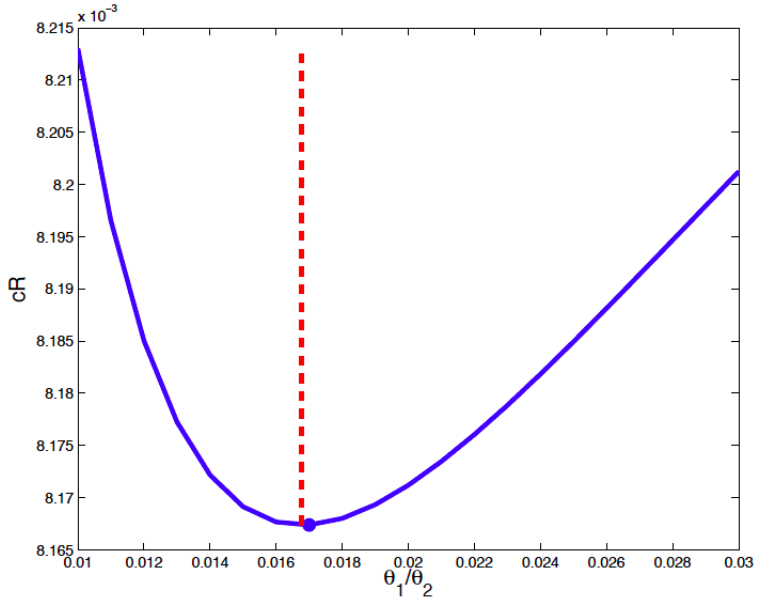

Figure A.2: cR.

$$J_r = \sum_{i=1}^{m-1} (\hat{s}_{i+1} - \hat{s}_i)^2 \tag{A.4}$$

$$J_f = \sum_{i=1}^{n} (y_i - \sum_{j=1}^{m} H_{i,j}\hat{s}_j)^2 \tag{A.5}$$

J_r represents the flatness of the estimate, it is small when the estimate is relatively uniform, and J_f represents how faithful the data is reproduced, when it is small, the data is reproduced more faithfully. When $\theta_1/\theta_2 = 0.0167$, J_r vs J_f is shown in Figure A.3. This shows that under our estimation ratio between θ_1 and θ_2, J_r and J_f achieves a good trade-off.

In the linear inverse modeling, two objectives have been set up: one is reproducing the data and the other is to meet the requirement of the prior information, which includes uniformity, flatness and smoothness of the estimate. The choices of the regulation schemes and the relative weighting of the two terms in the objective function

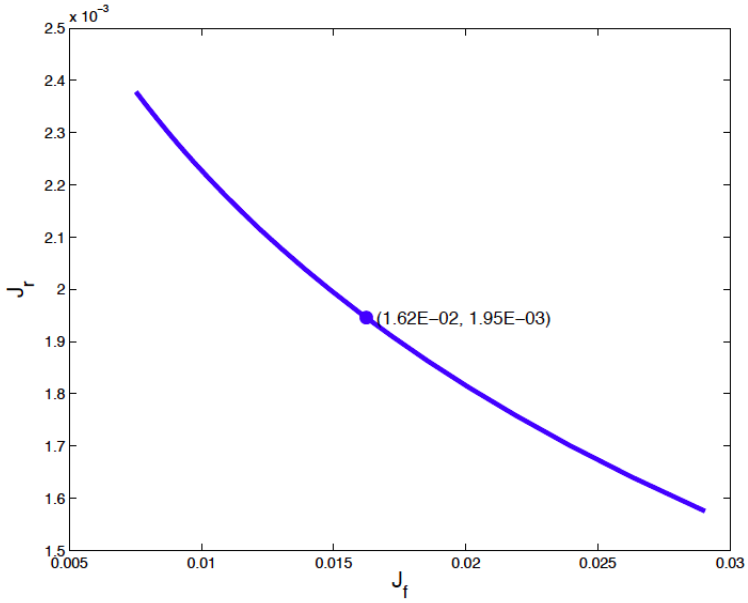

Figure A.3: Trade-off between J_r and J_f.

have profound effects on the result of the inverse problem.

In summary, we parameterized the prior information and measurement error by two structural parameters: θ_1 and θ_2. The choice of these parameters are guided by the data, and the algorithm solves the problem in the sense of minimizing the loss function which does not obtain the two objectives. As shown here, our estimation of θs gives a good-trade off between reproducing the data and being consistent with prior information.

Appendix B

Numerical Distretization for Reservoir Temperature Model

The detail of the discretized form of the reservoir temperature equation Eq. 4.15 is shown in this Appendix. The Eq. 4.15 represents the energy balance in the reservoir, considering several heat transfer mechanisms, is repeated here.

$$\overline{\rho C_p}\frac{\partial T}{\partial t} - \phi\beta T\frac{\partial p}{\partial t} = \overline{k_T}\nabla^2 T - \rho c_p u\nabla T + (\beta T - 1)u\nabla p \tag{B.1}$$

where u is velocity, β is the thermal expansion coefficient and the over bars stand for the mean properties for the mixture of fluids and rocks. As discussed in Chapter 4, the first-order derivative is approximated by a forward difference and the second-order derivative by central differences (Eq. 4.85 to 4.89). We used implicit method in temporal advance, and the discretized form of Eq. B.1 can be written as Eq. B.2.

$$\begin{aligned}\overline{\rho C_p}\frac{T_{i,j}^{n+1} - T_{i,j}^{n}}{\Delta t} &= \overline{k_T}\frac{T_{i+1,j}^{n+1} - 2T_{i,j}^{n+1} + T_{i-1,j}^{n+1}}{\Delta x^2} - \rho c_p u\frac{T_{i+1,j}^{n+1} - T_{i-1,j}^{n+1}}{2\Delta x} \\ &\quad +(\beta T - 1)u\frac{p_{i+1,j}^{n+1} - p_{i-1,j}^{n+1}}{2\Delta x} + \phi\beta T\frac{p_{i,j}^{n+1} - p_{i,j}^{n}}{\Delta t}\end{aligned} \tag{B.2}$$

Again, as discussed in Section 4.1.6, the coefficients in Eq. B.2 are obtained by solving secondary equations. The solving scheme we chose to use is implicit Euler, more details were discussed in Section 4.1.6.

References

[1] Atkinson, P.G. and Ramey, H.J. 1977. Problems of Heat Transfer in Porous Media. SPE 6792 presented at the 52nd Annual Fall Technical Conference and Exhibition in Denver, CO.

[2] Achinivu, O.I., Li, Z., Zhu, D. and Hill, A.D. 2008. An Interpretation Method of Downhole Temperature and Pressure Data for Flow Profiles in Gas Wells. SPE 116292 presented at SPE Russian Oil and Gas Technical Conference and Exhibition, Moscow, Russia.

[3] Alves, I., Alhanatl, F. and Shaham, O. 1992. A Unified Model for Predicting Flowing Temperature Distribution in Wellbore and Pipelines. *SPE Production Engineering* 363.

[4] Bahrami, H. and Siavoshi, J. 109544. Application of Temperature Transient Analysis in Well Test Interpretation. SPE 109544 presented at the SPE Asia Pacific Oil and Gas Conference and Exhibition, Jakarta, Indonesia.

[5] Brown, G. and Tiwari, P. 2010. Using DTS Flow Measurement Below Electrical Submersible Pumps to Optimize Production From Depleted Reservoirs by Changing Injection Support Around the Well. SPE 135130 presented at the SPE Annual Technical Conference and Exhibition held in Florence, Italy.

[6] Brown G., Carvalho, B., Wray, A., Smith, D, Toombs, M. and Pennell, S. 2004. Monitoring Alternating CO2 and Water Injection and Its Effect on Production in a Carbonate Reservoir Using Permanent Fiber-Optic Distributed Temperature Systems. SPE 90248 presented at the SPE Annual Technical Conference and Exhibition held in Houston, Texas.

[7] Brown, G. 2005. Monitoring Multilayered Reservoir Pressure and Gas/Oil Ratio Changes Over Time Using Permanently Installed Distributed Temperature Measurements. SPE101886 presented at the SPE Annual Technical Conference and Exhibition, San Antonio, TX, USA.

[8] Brown, G., Field, D. Davies, J., Vollins, P. and Garayeva, N. 2005. Production Monitoring Through Openhole Gravel-Pack Completions Using Permanently Installed Fiber-Optic Distributed Temperature Systems in the BP-Operated Azeri Field in Azerbaijan. SPE 95419 presented at the SPE Annual Technical Conference and Exhibition, Dallas, TX, USA.

[9] Chen, N. 1979. An Explicit Equation for Friction Factor in *Pipe. Ind. Eng. Chem. Fundamentals* **18**(3) : 296.

[10] Corey, A. T. 1954. The Interrelation Between Gas and Oil Relative Permeabilities. *Producer Monthly*, Nov (1954), 38-41.

[11] Curtis, M.R. and Witterholt, E.J. 1973. Use of the Temperature Log for Determining Flow Rates in Production Wells. *Journal of Petroleum Technology.*

[12] Drakeley, B.K., Johansen, E.S., Zisk, E.J. and Bostick, F.X. 2006. In-Well Optical Sensing State of the Art Application and Future Direction for Increasing Value in Production-Optimization Systems. SPE 99696 presented at the SPE Intelligent Energy Conference and Exhibition held in Amsterdam, The Netherlands.

[13] Dropkin, D. and Sommerscales, E., 1965. Heat Transfer by Natural Convection in Liquids Confined by Two Parallel Plates Inclined at Various Angles with Respect to the Horizontal, *J. Heat Transfer; Trans., ASME, Series C* (Feb., 1965) **87**, 77- 84.

[14] Duru, O. and Horne, R. 2009. Simultaneous Interpretation of Pressure, Temperature and Flowrate Data for Improved Model Identification and Reservoir Parameter Estimation. SPE 124827 presented at the SPE Annual Technical Conference and Exhibition held in New Orleans, USA.

[15] Duru, O. and Horne, R. 2010. Joint Inversion of Temperature and Pressure Measurements for Estimation of Permeability and Porosity Fields. SPE 134290 presented at the SPE Annual Technical Conference and Exhibition held in Florence, Italy.

[16] Duru, O. 2011. Reservoir Analysis and Parameter Estimation Constrained to Temperature, Pressure and Flowrate Histories. PhD dissertation.

[17] Elashaawi, H., Osman, M.S. and Sengul, M. 1999. Use of Temperature Data in Gas Well Tests. SPE 56613 presented at the SPE Annual Technical Conference and Exhibition, Houston, TX.

[18] Glasbergen, G, Gualtieri, D, van Domelen, M. and Sierra, J. 2007. Real-Time Fluid Distribution Determination in Matrix Treatment Using DTS. SPE 107775 presented at the European Formation Damage Conference held in Scheveningen, the Netherlands.

[19] Hadley, M.R., Brown, G.A. and Naldrett, G. 2005. Evaluation Permanently Installed Fiber-Optic Distributed Temperature Measurements Using Temperature-Step Resolution. SPE 97677 presented at the SPE International Improved Oil Recovery Conference in Asia Pacific held in Kuala Lumpur, Malaysia.

[20] Hagoort, J. 2004. Ramey's Wellbore Heat Transmission Revisited. *Journal of Petroleum Technology*, SPE 87305.

[21] Hasan, A., Kabir, C. and Sayarpour, M. 2007. A Basic Approach to Wellbore Two-Phase Flow Modeling. SPE109868 presented at the SPE Annual Technical Conference and Exhibition, Anaheim, California, USA.

[22] Horne, R. and Shinohara, K. 1979. Wellbore Heat Loss in Production and Injection Wells. *SPE Journal of Petroleum Technology* 116-118.

[23] Hembling, D., Berberian, F., Carter, N. and Naldrett, G. Enabling Efficient Permanent Production Monitoring of Advanced Well Completions in Saudi Arabia Using Fiber Optic Distributed Temperature Sensing. 2008. SPE 115255 presented at the SPE Annual Technical Conference and Exhibition, Denver, USA.

[24] Hoang, H., Mahadevan, J. and Lopez, H. 2011. Interpretation of Wellbore Temperatures Measured Using Distributed Temperature Sensors During Hydraulic Fracturing. SPE 140442 presented at the SPE Hydraulic Fracturing Technology Conference and Exhibition, Woodlands, TX.

[25] Huckabee, P. 2009. Optic Fiber Distributed Temperature for Fracture Stimulation Diagnostics and Well Performance Evaluation. SPE 118831 presented at the SPE Hydraulic Fracturing Technology Conference held in Woodlands, TX.

[26] Hutchinson, D.A., Kuramshina, N., Sheydayev, A. and Day, S. 2007. The New Interference Test: Reservoir Connectivity Information from Downhole Temperature Data. SPE 11672 presented at the International Petroleum Technology Conference held in Dubai, U.A.E..

[27] Izgec, B., Hasan, A.R., Lin, D. and Kabir, C.S. 2008. Flow Rate Estimation From Wellhead Pressure and Temperature Data. SPE 115790 presented at SPE Annual Technical Conference and Exhibition, Denver, USA.

[28] Johnson, D., Sierra, J. and Gualtieri, D. 2006. Successful Flow Profiling of Gas Wells Using Distributed Temperature Sensing Data. SPE 103097 presented at the SPE Annual Technical Conference and Exhibition, San Antonio, TX.

[29] Kitanidis, P. K. 1986. Parameter Uncertainty in Spatial Functions: Bayesian Analysis. *Water Resources Research*, 22, 499-507.

[30] Kitanidis, P. K. 1991. Orthonormal Residuals in Geostatistics: Model Criticism and Parameter Estimation. *Math. Geol*, **23** (5), 741-758.

[31] Kitanidis, P. K. 1995. Quasilinear Geostatistics Theory for Inversing. *Water Resources Research*, **31**, 2411-2419.

[32] Kitanidis, P. K. 2007. On stochastic inverse modeling. *Water monograph paper.*

[33] Le Gallo, Y.L. and Latil, M.J. 1993. Modeling Thermal and Pressure Drops for Multiphase Flow in Thermal Horizontal Wells. SPE 26077 presented at the Western Regional Meeting, Anchorage, AK.

[34] Leskens, M., de Kruif, B., Belfruid, S., Smeulers, J. and Gryzlov, A. 2008. Downhole Multiphase Metering in Wells by Means of Soft-Sensing. SPE 112046 presented at the SPE Intelligent Energy Conference and Exhibition, Amsterdam, Netherlands.

[35] Li, Z. and Zhu, D. 2010. Optimization of Production with ICV Using Temperature Data Feedback in Horizontal Wells. SPE 135156 presented at the SPE Annual Technical Conference and Exhibition, Florence, Italy.

[36] Li, Z. and Zhu, D. 2010. Predicting Flow Profile of Horizontal Well by Downhole Pressure and Distributed Temperature Data for Waterdrive Reservoir. *SPE Production and Operations*. August, 2010. 296-304

[37] Livescu, S., Durlofsky, L. and Aziz, K. 2008. Application of a New Fully Coupled Thermal Multiphase Wellbore Flow Model. SPE113215-MS presented at the SPE Improved Oil Recovery Symposium, Tulsa, Oklahoma

[38] Livescu, S., Aziz, K. and Durlofsky, L.J. 2009. Development and Application of a Fully-Coupled Thermal Compositional Wellbore Flow Model. SPE121306 presented at the SPE Western Region Meeting, San Jose, California, USA.

[39] Lorentzen, R.J., Savareid, O. and Navdal, G. 2010. Rfate Allocation: Combining Transient Well Flow Modeling and Data Assimilation. SPE 135073 presented at the SPE Annual Technical Conference and Exhibition, Florence, Italy.

[40] Mallat,S and Hwange, W. L., 1992. Singularity detection and processing with wavelets. *IEEE Transaction on Information Theory*, **38**:617-643.

[41] Nath, D., Sugianto, R. and Finley, D. 2005. Fiber-Optic Distributed Temperature Sensing Technology Used for Reservoir Monitoring in An Indonesia Steamflood. SPE97912 presented at the SPE International Thermal Operation and Heavy Oil Symposium, Calgary, Alberta, Canada.

[42] Nath, D.K., Finley, D.B., Kaura, J.D., Krismartopo B. and Yudhiarto, W. 2006. SPE 103069 presented at the SPE Annual Technical Conference and Exhibition held in San Antonio, USA.

[43] Nasri, Z. and Binous, H. 2009. Application of the Peng-Robinson Equation of State Using Matlab. *J. Chem. Engr* **43** (2)

[44] Neuringer, J.L. 1968. Green's Function For An Instantaneous Line Particle Source Diffusing In A Gravitional Field and Under The Influence of A Linear Shear Wind. SIAM *J. APPL. MATH.*, **16** (4), July 1968.

[45] Ouyang, L. and Aziz, K. 2000. A Homogeneous Model for Gas-Liquid Flow in Horizontal Wells. *J. Pet. Sci. and Eng.* **27** (2000) 119-128.

[46] Ouyang, L. 2005. Production and Injection Profiling - Challenges and New Opportunities. SPWLA 46 th Annual Logging Symposium, New Orleans, USA.

[47] Ouyang, L. and Belanger, D. 2006. Flow Profiling by Distributed Temperature Sensor (DTS) System Expectation and Reality. *SPE Production and Operation Journal*, SPE 90541.

[48] Peng, D. and Robinson, D. 1976. A New Two-Constant Equation of State. *Industrial and Engineering Chemistry: Fundamentals* **15**(59).

[49] Pinzo, I.D., Davies, J.E., Mammadkhan, F. and Brown G.A. 2007 Monitoring Production From Gravel-Packed Sand-Screen Completion on BP's Azeri Field Wells Using Permanently Installed Distributed Temperature Sensors. SEP 110064 presented at the SPE Annual Technical Conference and Exhibition held in Anaheim, CA.

[50] Platenkamp, R.J. 1985. Temperature Distribution around Water Injector. Paper 13746 presented at the SPE Middle East Oil Technical Conference and Exhibition held in Bahrain.

[51] Pourafshary, P., Varavei, A., Sepehrnoori, K. and Podio A. 2008. A Compositional Wellbore/Reservoir Simulator to Model Multiphase Flow and Temperature Distribution. SPE12115 presented at the International Petroleum Technology Conference, Kuala Lumpur, Malaysia.

[52] Ramey, H. 1962. Wellbore Heat Transmission. *SPE Journal of Petroleum Technology* **14**(4): 427-435. Roy, B. N. 1992. Fundamentals of Classical and Statistical Thermodynamics. 1st Edition, John Wiley.

[53] Sagar, R., Dort, D.R. and Schmidt, Z. 1991. Predicting Temperature Profiles in a Flowing Well. *SPE Production Engineering*, Noveber, 1991, 441-448.

[54] Semenova, A., Livescu, S., Durlofsky, L.J. and Aziz, K. 2010. Modeling of Multi-segmented Thermal Wells in Reservoir Simulation. SPE 130371 presented at the SPE EUROPEC/EAGE Annual Conference and Exhibition held in Barcelona, Spain.

[55] Shi. H., Holmes, J.A., Durlofsky, L.J., Aziz, K., Diaz, L.R., Alkaya, B.and Oddie, G. 2005. Drift-Flux Modeling of Two-Phase Flow in Wellbores. *SPE Journal*, March, 2005. 24-33.

[56] Shirdel, M. and Sepehrnoori, K. 2009. Development of a Coupled Compositional Wellbore/Reservoir Simulator for Modeling Pressure and Temperature Distribution in Horizontal Wells. SPE 124806 presented at SPE Annual Technical Conference and Exhibition held in New Orleans, USA.

[57] Sierra J., Kaura, J., Gualtieri, D. Glasbergen, G., Sarkar, D. and Johnson, D. 2008. DTS Monitoring Data of Hydralic Fracturing: Experience and Lessons Learned. SPE 116182 presented at the SPE Annual Technical Conference and Exhibition, 21-24 September 2008, Denver, USA.

[58] Silva, M.F., Lzetti, R.G., Pinto, P. and Couto, I.R. 2007. Management of Steam Flooding in Nine Spot with Fiber Optic in Observation Wells. SPE 107800 presented at the SPE Latin American and Caribbean Petroleum Engineering Conference, Buenos Aires, Argentina.

[59] Spivey, J.P. 2006. Estimating Layer Properties for Wells in Multilayer Low-Permeability Gas Reservoirs by Automatic History-Matching Production and Production Log Data. SPE 100509 presented at the SPE Gas Technology Symposium, Calgary, Canada.

[60] Steffensen, R.J. and Smith, R.C. 1973. The Importance of Joule-Thomson Heating (or Cooling) in Temperature Log Interpretation. SPE 4636 presented at the 48th Annual Fall Meeting of SPE of AIME, Las Vegas, NV.

[61] Stone, T., Edmunds, N.R. and Kristoff, B.J. 1989. A Comprehensive Wellbore/Reservoir Simulator. SPE 18419 presented at the SPE Symposium on Reservoir Simulation in Houston, TX.

[62] Stone, T., Bennett, J., Law, D. and Holmes, J. 2002. Thermal Simulation with Multisegment Wells.*SPE Reservoir Evaluation Engineering*, SPE 78131-PA **5**(3): 206-218.

[63] Stone, T., Edmunds, N., and Kristoff, B. 1989. A Comprehensive Wellbore/Reservoir Simulator. SPE18419 presented at the SPE Simulation Symposium, Houston, Texas.

[64] Sui, W, Zhu, D, Hill, A.D. and Ehlig-Economides, C.A. 2008 Determining Multilayer Formation Properties From Transient Temperature and Pressure Measurements. SPE 116270 presented at the SPE Annual Technical Conference and Exhibition, 21-24 September 2008, Denver, USA.

[65] Sui, W., Zhu, D., Hill, A.D., and Ehlig-Economides, C.A. 2008 Model for Transient Temperature and Pressure Behavior in Commingled Vertical Wells. SPE 115200-MS presented at the SPE Russian Oil and Gas Technical Conference and Exhibition, 28-30 October 2008, Moscow, Russia

[66] Tarantola, A. 2005. Inverse Problem Theory and Methods for Model Parameter Estimation. SIAM. ISBN 0-89871-572-5 (pbk.)

[67] Torrencen, C. and Webster, P.J. 1998. The Annual Cycle of Persistence in the El Nino-Southern Oscillation. *Quart. J. Roy. Meteor. Soc.*

[68] Varavei, A. and Sepehrnoori, K. 2009. An EOS-Based Compositional Thermal Reservoir Simulator. SPE 119154 presented at the SPE Reservoir Simulation Symposium, Woodlands, TX.

[69] Wang, X. Lee, L., Thigpen, B., Vachon, G., Poland, S. and Norton, D. 2008. Modeling Flow Profile Using Distributed Temperature Sensor System. SPE 111790 presented at the SPE Intelligent Energy Conference and Exhibition, Amsterdam, Netherlands.

[70] Wang, Z. and Horne, R. 2011. Analyzing Wellbore Temperature Distributions Using Nonisothermal Multiphase Flow Simulation. SPE 144577 presented at the SPE Western North American Regional Meeting, Anchorage, AK.

[71] Weaver, M., Kragas, T., Burmans, J., Copeland, D., Phillips, B. and Seagraves, R. 2005. Installation and APplication of Permanent Downhole Optical Pressure /Temperature Gauges and Distributed Temperature Sensing in Producing Deepwater Wells at Marco Polo. SPE 95798 presented at the SPE Annula Conference and Exhibition held in Dallas, TX.

[72] Willhite, G. 1967. Over-all Heat Transfer Coefficients in Steam and Hot Water Injection Wells. *Journal of Petroleum Technology* **19**(5): 607-615.

[73] Wood, P., Simpson, A, Holland, B., Brown, G., Rogers, G., Anderson, S., Balster, E. and Figueroa, M. 2010. Monitoring Flow and Completion Integrity of

a North Sea Subsea HPHT appraisal Well During an Extended Well Test Using Permanently Installed Fiber-Optic Temperature Sensors. 2010. SPE 137120 presented at the SPE Deepwater Drilling and Completions Conference held in Galveston, TX.

[74] Yee, E. 1990. An Approximate Analytical Solution for the Reaction-Convection-Diffusion Equation. *Physical Letter A*, **151**(6,7), 17 November, 1990

[75] Yoshioka, K., Zhu, D and Hill, A.D.2005. A Comprehensive Model of Temperature Behavior in a Horizontal Well. SPE 95656 presented at the SPE Annual Technical Conference and Exhibition, Dallas, TX.